Master's thesis

NTNU
Norwegian University of Science and Technology
Faculty of Engineering
Department of Energy and Process Engineering

Benedikt Julius Eichner

Simulation of temperature distribution within a PEM electrolysis stack using ex-situ thermal conductivity measurements

Master's thesis in EXCHANGESTUD_IV
Supervisor: Jacob Joseph Lamb
December 2023

NTNU
Norwegian University of
Science and Technology

Benedikt Julius Eichner

Simulation of temperature distribution within a PEM electrolysis stack using ex-situ thermal conductivity measurements

Master's thesis in EXCHANGESTUD_IV
Supervisor: Jacob Joseph Lamb
December 2023

Norwegian University of Science and Technology
Faculty of Engineering
Department of Energy and Process Engineering

NTNU
Norwegian University of
Science and Technology

Abstract

Polymer Electrolyte Membrane (PEM) water electrolysers are considered to be particularly well suited to produce green hydrogen in industrial scale from fluctuating renewable sources. In order to increase production rates, the current densities are being gradually enhanced, which leads to increased heat production inside the Electrolysis Cells (ECs). It is therefore more and more important to consider thermal gradients within the single ECs inside the stacks. A 2D thermal numerical steady state model of an industrial-sized PEM electrolysis stack is therefore presented here. Thermal gradients within the ECs inside the stack are predicted both in stacking direction and along the channels of the Flow Fields (FFs). For this, through-plane thermal conductivities were measured ex-situ for titanium felt Porous Transport Layer (PTL), Tion5-W PFSA membrane and EC Catalyst Layers (CLs). At 16 bar compaction pressure, the wet PTL showed a thermal conductivity of $(2.67 \pm 0.21)\,\mathrm{W\,m^{-1}\,K^{-1}}$, the wet membrane of $(0.31 \pm 0.01)\,\mathrm{W\,m^{-1}\,K^{-1}}$ and the wet CL of $(0.19 \pm 0.03)\,\mathrm{W\,m^{-1}\,K^{-1}}$. Using these values in the stack model, thermal gradients of $(16.5 \pm 0.6)\,\mathrm{K}$ in parallel flow and $(17.6 \pm 0.5)\,\mathrm{K}$ in counter-flow were predicted within the cells of $1\,\mathrm{m^2}$ cell area at a current density of $2\,\mathrm{A\,cm^{-2}}$ and a mass flow rate of $0.15\,\mathrm{kg\,s^{-1}}$ water of $60\,^{\circ}\mathrm{C}$ at the inlets of both anodic and cathodic FF. The counter-flow arrangement showed an advantage of 0.2 % in voltage efficiency. With non-thermally-insulated end-plates, the maximal temperature was predicted to decrease in the outer cells of the stack by up to 3.7 K where the anodic half-cell adjoins the end-plate, and by up to 2.1 K where the cathodic half-cell adjoins the end-plates. Increasing the current density to $3\,\mathrm{A\,cm^{-2}}$ led to an increase in thermal gradients by about 10 K, both in parallel and counter-flow conditions. Using a sintered PTL, however, decreased the thermal gradients at $2\,\mathrm{A\,cm^{-2}}$ by around 3.7 K. The simulation showed an increase in maximal thermal gradients within the stack by 20 to 40 % compared to other models that use lumped properties within the cells. This underlines the importance of considering in-cell thermal gradients also on a stack level.

Contents

List of Figures

List of Tables

Acronyms

Nomenclature

Latin Symbols

a	Thermodynamic activity
A	Area
c_p	Specific isobaric heat capacity
$C_\mathrm{v,m}$	Molar isochoric heat capacity
D	Diffusivity
E_cd	Activation energy of the exchange current density
E_ct	Activation energy of the charge transfer coefficient
E_mem	Activation energy of the membrane conductivity
F	Faraday constant
G	Gibbs free energy
h_t	Heat transfer coefficient
H	Enthalpy
H_S	Henry's coefficient
i	Current density
i_0	Exchange current density
j	Arbitrary number
K^mem	Linear factor for membrane conductivity
l	length
$\dot{m}$	Mass flow
M	Molar mass
N	Amount of elements in a quantity
p	Pressure
$\dot{q}$	Heat flux
$\dot{Q}$	Heat flow
R	Universal gas constant
R	Thermal resistance
R_el	Electric resistance
R_c	Thermal contact resistance
$R_\mathrm{el,c}$	Electric contact resistance
S	Entropy
t	Time

t_e	Equivalent time
T	Temperature
u	Uncertainty of measurement
u_c	Combined uncertainty of measurement
u_ext	Combined uncertainty of measurement
V	Voltage
x	Position
X	Arbitrary measurement result
Y	Arbitrary measurement result
Δx_tc	Distance between thermocouples in thermal conductivity apparatus

Greek Symbols

α	Thermal diffusivity
α_ct	Charge transfer coefficient
δ	Thickness
ϵ	Maximal allowable change per iteration in numerical solver
$\epsilon_\mathrm{V}^\mathrm{HHV}$	Voltage efficiency according to higher heating value
κ	Thermal conductivity
λ	Water molecules per sulphonic group in Nafion®
μ_act	Activation overpotential
μ_mt	Mass-transfer overpotential
μ_ohm	Ohmic overpotential
ρ_A	Area density
σ	Ionic conductivity
Ω	Constant factor representing the weight gain due to wetting in Nafion® membranes

Indizes

$\overline{()}$	Mean value of a quantity
0	(Subscript) At reference state
∞	(Superscript) With regard to the free stream of a fluid
α	(Superscript) Placeholder for any component
Θ	(Superscript) At standard conditions
a	(Superscript) With regard to the anode side
amb	(Superscript) At ambient conditions
bl	(Superscript) With regard to the boundary layer of a flow
c	(Superscript) With regard to the cathode side
cell	(Superscript) With regard to a single cell
conv	(Subscript) With regard to convective heat transfer
drag	(Superscript) With regard to water drag through the membrane
i	(Subscript) Indicating single element in a quantity
in	(Subscript) Flowing into the system
m	(Subscript) Molar quantity
mem	(Superscript) With regard to the membrane
mesh-cell	(Subscript) With regard to a single cell in the simulation-mesh
out	(Subscript) Flowing out of the system
s	(Superscript) With regard to a solid
set	(Subscript) At set-point
rev	(Subscript) Reversible
R	(Superscript) With regard to the reaction
sample	(Subscript) With regard to the sample
sat	(Subscript) Saturated
supersat	(Subscript) Supersaturated
thn	(Subscript) Thermo-neutral
x	(Subscript) In x-direction
y	(Subscript) In y-direction
z	(Subscript) In z-direction

1. Introduction

Moving away from a fossil-fuel-based economy leads to the need for alternative options to store large amounts of energy and the replacement of fossil-based chemicals by base materials of renewable origins. Green hydrogen produced from renewable energy and water is considered an important energy carrier for these applications. [1, 2] The Polymer Electrolyte Membrane (PEM) technology is considered to be particularly well suited for industrial scale production of hydrogen from fluctuating renewable sources because of its fast response to changing load profiles, high current densities, low operating temperatures and the high purity of produced gasses [3]. First industrial productions of large-scale industrial electrolysis stacks started the in recent years [4]. However, in order to further increase effectivity in terms of hydrogen produced per membrane area and thus decrease production costs, the current densities are expected to further increase over the years [3]. This leads to an increase in production of irreversible heat inside the stack. Inside the stacked Electrolysis Cells (ECs) this heat is produced within the Membrane Electrode Assemblys (MEAs) in the centre of the cells and must be transported through the adjoining Porous Transport Layers (PTLs) to the Flow Fields (FFs) where the flowing water, oxygen, and hydrogen absorb the excess heat of the electrolysis reaction. A higher production rate of heat thus leads to increased thermal gradients within the ECs, which have a high impact on local degradation rates, and might lead to locally overshooting the maximal operating temperatures of the PEM [5, 6]. With increasing current densities, it is thus of more and more importance to consider thermal gradients within the cells of PEMEC stacks for efficient operations management and cell design.

However, most models in literature assume a constant temperature over the stack when analysing the thermal behaviour [7]. For a single EC, few models exist that consider thermal gradients in stacking direction. Bock *et al.* [7] modelled the temperature distribution in stacking direction within a single EC for the first time in 2020. Predicting temperature gradients within the EC requires knowledge about the thermal conductivities of the materials used in the cells. Bock *et al.* therefore measured the thermal conductivity of the PTLs and used literature values for the Nafion® membrane, but only approximated the thermal conductivities of the Catalyst Layers (CLs) inside the MEA by thermal conductivities of Fuel Cell (FC) CL. They investigated the effect of different PTL compositions and water contents in the cathodic fluid on the temperature distribution in stacking direction as well as between the channels of the FF. Moradi Nafchi *et al.* [8] then simulated the temperature distribution over a single MEA in stacking direction and investigated the impact of operating pressure and mean temperatures as well as current density and membrane

thickness, but did not mention the origin of the used thermal conductivity values. Yasutake *et al.* [9] simulated the temperature distribution within a small single cell along the channels of the FF and in stacking direction using calculated values for PTL and CL thermal conductivity. They analysed the impact of high current densities, different membrane thicknesses and flow-rates on the temperature distribution. However, to best of the author's knowledge, no study exists that models the temperature distribution using exact, measured thermal conductivities for all layers inside the EC. On a stack level, mostly small-scale laboratory stacks are modelled with little impact of the temperature-gradients along the channels of the FFs [5]. Most models also use lumped values over the stack, neglecting gradients between the cells [10, 11, 12]. Krenz *et al.* [5] recently modelled for the first time temperature gradients between cells of an industrial-sized PEMEC stack in stacking direction as well as along the channels of the FFs. However, they used lumped values for all solid layers within the cells and thus neglected significant temperature gradients within the single cells in the stack.

The aim of this study is therefore to simulate the temperature distribution within an industrial-sized PEMEC stack, considering thermal gradients within the single cells of the stack using measured thermal conductivity values for all layers of the ECs.
For this purpose, trough-plane thermal conductivities of platinum coated titanium felt PTL, Tion5-W PFSA membrane and mean values of iridium ruthenium oxide Anodic Catalyst Layer (ACL) and platinum black Cathodic Catalyst Layer (CCL) are measured ex-situ under different compaction pressures and humidification levels using the heat flux method. A numerical steady-state thermal model is developed for an industrial-sized PEMEC stack considering thermal gradients along the channels of the FF and within as well as between the single ECs in stacking direction. Parallel and counter-flow arrangements are compared in terms of thermal gradients and efficiencies. The effect of different PTLs, current densities as well as dissimilar inlet-temperatures of anodic and cathodic fluid is investigated. Lastly, the impact of water drag through the membrane on temperature gradients and efficiencies on the cells in the stack is analysed.
Thus, this study presents, to best of the author's knowledge for the first time in literature, thermal conductivity measurements for PEMEC CLs and insights into thermal gradients within the cells of a PEMEC stack.

In the following, firstly an overview about the relevant heat transfer mechanisms, principles of PEM electrolysis and the calculation of measurement uncertainties is given in chapter 2. Afterwards, the experimental setup and procedure for the thermal conductivity measurements is presented in section 3.1. In section 3.2 the numerical stack model as well as the validation and simulation procedures are described. Subsequently, the measured thermal conductivities and simulated temperatures are presented in chapter 4 and discussed in chapter 5. Finally, in chapter 6 the findings are summarized and an outlook on future fields of research is given.

2. Background

2.1. Heat Transfer

Heat transfer describes an energy transfer due to a difference in temperature as driving force. The heat transfer can occur in form of conduction or radiation in solid materials, and in fluids additionally in form of convection. [13, p. 1]
For small temperature gradients, as they occur in PEM cells, radiation heat transfer is negligible compared to conduction and convection. It is therefore not further examined in this work. A one dimensional heat flux $\dot{q}$ due to conduction heat transfer within a bulk material can be described by Fourier's law with the temperature T and the position x (equation 2.1)[13, p. 1]:

$$\dot{q}'' = -\kappa \frac{\delta T}{\delta x} \tag{2.1}$$

κ represents the thermal conductivity, which is a material property describing the ability of a material to conduct heat. The higher the thermal conductivity, the higher the heat flux in the material at a given thermal gradient. The barrier that a material layer poses against a heat flow can be expressed as an area specific thermal resistance R. The thermal resistance can be calculated using equation 2.2 with the material's cross-sectional area A and its thickness Δx. It can again be used to calculate the heat flux using equation 2.3 [13, p. 9].

$$R = \frac{\Delta x}{\kappa A} \tag{2.2}$$

$$\dot{q} = \frac{\Delta T}{R} \tag{2.3}$$

When two solid materials are brought together, the contact of the surfaces is never perfect, so that the energy cannot pass unimpeded. The area specific contact resistance R_c describes this barrier. The value is dependent on many factors as the involved materials, the contact pressure, the surface structure and the interstitial material. [13, p. 14]

Convective heat transport mechanisms can be distinguished into natural convection, where the fluid moves only through density gradients occurring through heating or cooling of the fluid, and forced convection, where the fluid motion is driven by external forces [13, p. 725]. For both types of convection, the rate of heat transfer between the fluid and the adjacent solid surfaces is governed by the Boundary Layers (BLs) of the fluid. BLs are thin layers of fluid adjacent to and affected by the solid surface [13, p. 483]. The convective heat transfer can therefore be

described similar to the conductive heat transfer, using the thickness of the BLs δ^{bl} and the temperature difference between the surface of the solid T^{s} and the temperature of the fluid at the edge between free stream and BL T^{∞} (equation 2.4) [13, p. 490].

$$\dot{q}''_{\mathrm{conv}} = -\kappa \frac{T^{\mathrm{s}} - T^{\infty}}{\delta^{\mathrm{bl}}} \tag{2.4}$$

As the thickness of the BL and the fluid's thermal conductivity depend on different properties of flow and fluid, the convective heat transfer is often simplified described using the heat transfer coefficient h_{t} (equation 2.5). h_{t} summarizes BL thickness, properties of the flow and thermal conductivities. It is tabulated in literature for common fluids and flow situations.

$$\dot{q} = h_{\mathrm{t}} \Delta T \tag{2.5}$$

2.2. PEM water electrolysis

The water electrolysis process separates water electrochemically into its elementary components oxygen and hydrogen using an external electrical voltage.

$$\mathrm{H_2O} \longrightarrow \mathrm{H_2} + \frac{1}{2}\,\mathrm{O_2} \tag{2.6}$$

The electrolysis thus converts electrical energy into chemical energy. The chemical energy in form of hydrogen can either be stored as energy carrier and later reconverted into electrical power using e.g. a FC or be used in other energy sectors e.g. as feedstock for hydrogen-containing chemical precursors [1, 2]. This makes the water electrolysis an important component in industrial decarbonisation to store large amounts of fluctuating renewable power and replace fossil-based chemicals. The PEM-technology is particularly well suited for coupling with renewable power sources as it provides a fast response to fluctuating load profiles as well as high current densities, a high purity of the produced gasses and low operating temperatures [2, 14]. To efficiently operate PEMECs, prevent overheating and ensure appropriate humidification of the membrane, it is of high importance to understand the internal temperature distribution in the cell. Hence, the following sections focus on the working principle as well as the thermal properties of the PEMEC technology.

2.2.1. Principle

A single PEMEC consists of several sandwiched layers, as shown in figure 2.1. The water is supplied through a FF impressed into the anodic Bipolar Plate (BP). From there it flows through the PTL to distribute the water uniformly over the cell area before it reaches the ACL. At the triple-phase boundary regions of the ACL, where educts, catalyst, proton- and electron conductors are available, the Oxygen Evolution Reaction (OER) (equation 2.7) takes place and the water is split into oxygen, hydrogen ions and electrons.

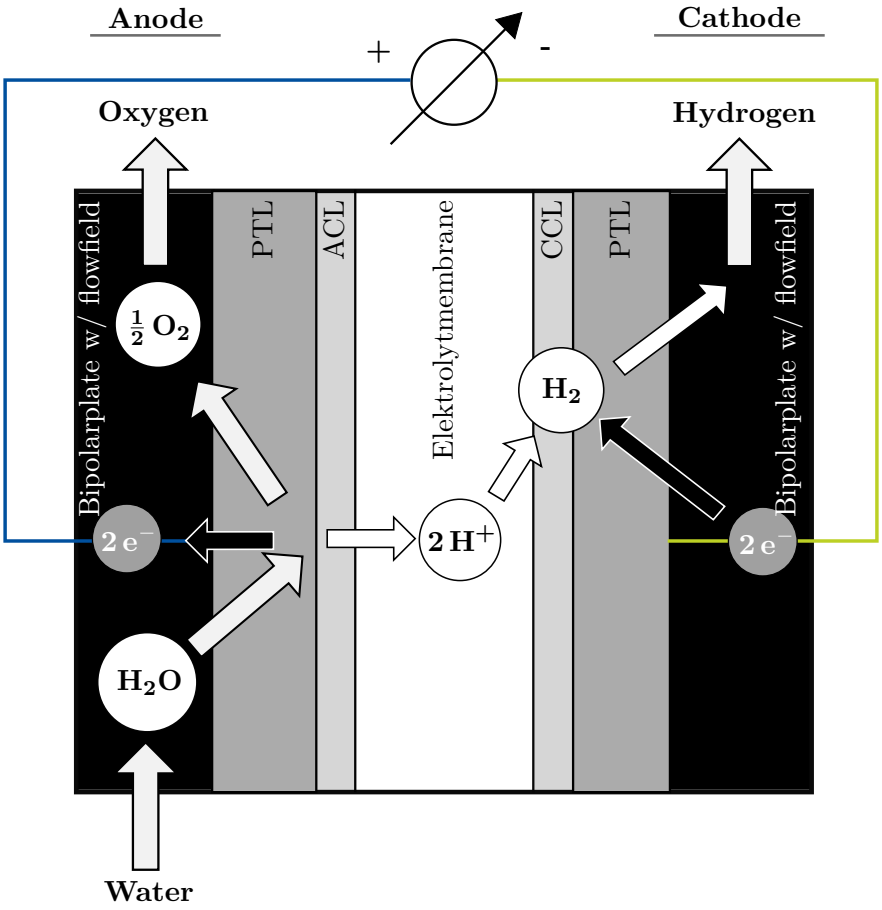

Figure 2.1.: Schematic of PEMEC

$$H_2O \longrightarrow \frac{1}{2} O_2 + 2\,H^+ + 2\,e^- \tag{2.7}$$

Due to the induced electrical voltage, a gradient in electrochemical potential forms between the anode and cathode, acting as a driving force for the hydrogen protons towards the cathode. Thus, the hydrogen protons move through the almost exclusively proton-conducting electrolyte membrane towards the cathode. As the electrolyte is not conductive to oxygen, the oxygen stays on the anode side and leaves the cell through PTL and FF in the BP. Also, the electrons go through the PTL and BP and flow through the external circuit to the cathode, where they react with the hydrogen protons in the CCL to molecular hydrogen (Hydrogen Evolution Reaction (HER), equation 2.8).

$$2\,H^+ + 2\,e^- \longrightarrow H_2 \tag{2.8}$$

Some water is also dragged by the hydrogen ions through the PEM to the cathode side [15]. This water leaves the cell together with the molecular hydrogen through the PTL and the FF in the BP on the cathode side.

The sandwiched ACL, membrane and CCL is referred to as MEA. The membrane needs to always be sufficiently humidified to optimize performance and minimize degradation. The humidification level is controlled by the water content of the feed-gasses [14].

Due to the low cell voltage of about 2 V [16, pp. 348 sqq.] multiple cells are layered to a stack and connected in series to operate the stack efficiently with conventional power electronics. The performance of the single cells in the stack is highly dependent on several factors as the composition of the gases, the humidification of the membrane or the temperature distribution inside the cell. This work focuses on the temperature distribution, which is difficult to measure inside the cell during operation without affecting the cell performance [17]. However, it is crucial to be able to predict the temperature distribution within the cell to prevent dryout and overheating of the membrane when e.g. increasing the current density and thus effectiveness of the cell [8]. Therefore, models are required to predict the temperature distribution over the cells, which demands knowledge over heat sources, -sinks and -flows within the cells. The thermodynamic properties of the electrolysis reaction are therefore presented in the following section.

2.2.2. Thermodynamic properties

The electrical energy required to drive the electrolysis reaction is partly converted into chemical energy in form of molecular hydrogen and partly dissipated into heat through different loss-mechanisms. The minimal amount of electrical energy required to split water into hydrogen and oxygen at standard conditions (index Θ) is described by the difference in molar Gibbs free energy $G_\mathrm{m}^{\mathrm{R},\Theta}$ between the products and educt (equation 2.9). [18]

$$G_\mathrm{m}^{\mathrm{R},\Theta} = G_\mathrm{m}^{\mathrm{H_2},\Theta} + \frac{1}{2} G_\mathrm{m}^{\mathrm{O_2},\Theta} - G_\mathrm{m}^{\mathrm{H_2O},\Theta} \tag{2.9}$$

This energy-requirement is commonly described in form of a potential difference, the reversible cell voltage ($V_\mathrm{rev}^\mathrm{cell}$). It can be calculated using equation 2.10 where F is the Faraday constant. [18]

$$V_\mathrm{rev}^{\mathrm{cell},\Theta} = \frac{\Delta G_\mathrm{m}^{\mathrm{R},\Theta}}{2\mathrm{F}} \tag{2.10}$$

The total reversible energy required for the electrolysis reaction is described by the difference in molar enthalpy between educt and products (H_m^R, equation 2.11). [18]

$$H_\mathrm{m}^\mathrm{R} = H_\mathrm{m}^{\mathrm{H_2}} + \frac{1}{2} H_\mathrm{m}^{\mathrm{O_2}} - H_\mathrm{m}^{\mathrm{H_2O}} \tag{2.11}$$

The remainder in total reversible energy not covered by the minimal electrical energy can be provided in form of heat. Using the definition of molar Gibbs free energy $G_\mathrm{m} = H_\mathrm{m} - TS_\mathrm{m}$ with the molar entropy S_m and the temperature T, the required amount of molar heat Q_m can be expressed by the change in entropy during the reaction S_m^R (equation 2.12).

$$Q_\mathrm{m,rev} = H_\mathrm{m}^\mathrm{R} - G_\mathrm{m}^\mathrm{R} = TS_\mathrm{m}^\mathrm{R} \tag{2.12}$$

The change in entropy can be calculated using equation 2.13.

$$S_{\mathrm{m}}^{\mathrm{R}} = S_{\mathrm{m}}^{\mathrm{H_2}} + \frac{1}{2} S_{\mathrm{m}}^{\mathrm{O_2}} - S_{\mathrm{m}}^{\mathrm{H_2O}} \tag{2.13}$$

The voltage required to provide the total reversible energy in form of electrical energy is called thermo-neutral voltage V_{thn} and can be calculated using equation 2.14 [18].

$$V_{\mathrm{rev}}^{\mathrm{cell}\Theta} = \frac{\Delta H_{\mathrm{m}}^{\mathrm{R}\Theta}}{2\mathrm{F}} \tag{2.14}$$

As mentioned above, different loss mechanisms occur during the electrolysis reaction so that the actual cell voltage is always higher than $V_{\mathrm{rev}}^{\mathrm{cell}}$. This increase in voltage is called overpotential (μ) and divided into activation (μ_{act}), ohmic (μ_{ohm}) and mass transfer (μ_{mt}) overpotentials (equation 2.15). The individual overpotentials are further discussed in section 3.2.1. [5]

$$V^{\mathrm{cell}} = V_{\mathrm{rev}}^{\mathrm{cell}} + \mu_{\mathrm{act}} + \mu_{\mathrm{ohm}} + \mu_{\mathrm{mt}} \tag{2.15}$$

The overpotentials increase with current density and lead to an increase in total cell voltage. During electrolysis operation, the current density is usually high enough that more heat is dissipated by the overpotentials in the membrane and CLs than used in the electrolysis reaction. This surplus heat must be transported out of the cell to prevent overheating. The main heat sink inside the cell is the fluid flowing through the FFs in the BPs. The heat transport from the place of generation in the MEA to the sink in the FFs occurs mainly by conduction. A temperature gradient forms over the cell, with the highest temperature being inside the MEA. [7]

The size of this gradient can either be determined using in-situ temperature measurements or by simulating the heat flow inside the cell. Measuring the temperature in-situ is demanding, as even the thinnest available temperature-sensors have a significant thickness compared to the thin layers in the EC. A temperature sensor inside the EC is therefore always prone to affect the current density distribution and thus the distribution of heat inside the cell. [17, 19, 20]
Most simulations, however, assume a constant temperature over the entire cell and thus risk underestimating the maximal temperature in the cell [12, 21]. Few models exist, which simulate the temperature distribution within a single EC [7, 8, 9]. Bock *et al.* [7] measures the thermal conductivity of EC PTL but estimates the thermal conductivities of the CLs from conductivities measured in FC CLs. Moradi Nafchi *et al.* [8] does not provide sources for the used thermal conductivity values. Yasutake *et al.* [9] uses literature values for the membrane's thermal conductivities but estimates the conductivity of the remaining layers using known bulk conductivities and pore-radii. No models are known that predict the temperature distribution within cells in PEMEC stacks.

2.3. Uncertainties of measurement

As every measurement is exposed to confounding effects, each result of a measurement must be given with an uncertainty. To quantify the uncertainties, a measurement uncertainty analysis is conducted following the ISO/IEC GUIDE 98-3 (GUM) [22]. The standard uncertainty u is calculated from the results X_i of N independent measurements using statistical techniques (Type A in GUM) (equation 2.16). The mean value $\overline{X}$, which represents the result of the measurement, is derived with equation 2.17.

$$u\left(\overline{X}\right) = \sqrt{\frac{1}{N^2 - N}\sum_{i=1}^{N}\left(X_i - \overline{X}\right)^2} \tag{2.16}$$

$$\overline{X} = \frac{1}{N}\sum_{i=1}^{N} X_i \tag{2.17}$$

If the result Y is derived from different results of measurements X_i using the function $Y = f(X_1, X_2, ..., X_N)$, the combined uncertainty u_c can be calculated using the uncertainty of every measurement result $u\left(\overline{X_i}\right)$ (equation 2.18).

$$u_\mathrm{c}\left(Y\right) = \sqrt{\sum_{i=1}^{N}\left[\left(\frac{\delta f}{\delta \overline{X}_i}\right) * u\left(\overline{X}_i\right)\right]^2} \tag{2.18}$$

The uncertainties are then presented in this paper using the extended uncertainty u_ext with a factor 2 (equation 2.19), which gives a confidence interval of 95 % for the measurement result given in the form $Y \pm u_\mathrm{ext}\left(Y\right)$.

$$u_\mathrm{ext}\left(Y\right) = 2u_\mathrm{c}\left(Y\right) \tag{2.19}$$

3. Methods

3.1. Measuring thermal conductivities

Thermal conductivities of materials used in the different layers of PEMFCs have been measured extensively in literature. The thermal conductivity of Nafion® membranes has been measured in [23, 24, 25, 26]. The thermal conductivity of CLs with different compositions has been investigated in [24, 27, 28, 29] and PTLs materials with and without Micro Porous Layers have been measured in [24, 30, 31, 32, 33, 34].
However, materials used in PEMECs have been investigated far less. The thermal conductivity of the Nafion® membrane can be taken from the studies mentioned above, as the membrane can be used both in FC and EC materials. However, CLs and PTLs have usually different compositions in FC and EC and must therefore be separately investigated [35, 36, 37]. Bock *et al.* [7] investigated the thermal conductivity of different sintered titanium PTLs under varying compaction pressure and humidification levels. Schuler *et al.* [38] measured the thermal conductivity of titanium felt PTLs with different porosities in-situ using indirect measurements of the membrane temperature. Though, no study is known that investigates the thermal conductivity of EC CL. The thermal conductivities for CL are in the models in literature therefore commonly approximated by values measured in FC CL or from bulk thermal conductivities [7, 9].

In order to gain a better knowledge about the thermal conductivities of the materials used in PEMECs, the materials should be measured in this study. Different techniques can be applied for this. One approach is to measure the conductivities in-situ under the actual electrolysis conditions by inserting thermocouples directly into the cell. This approach allows measuring thermal gradients inside the cell and calculating the produced heat with using the cell potential and current density. This approach, however, requires exact knowledge of the distances between the thermocouples. These values are difficult to determine as they depend on the compaction of the single layers, which again is influenced by the change in local pressure through the insertion of the thermocouples. Also the overpotentials and thus current density distribution within in the cell can be affected by the insertion of thermocouples. Together, this leads to a limited certainty of the determined thermal conductivities. [6]
Therefore, other approaches are being utilized to measure the thermal conductivity ex-situ. In general, the laser flash technique, which heats the sample on one side with a laser and measures the increase in temperature on the other side, is often used for ex-situ thermal conductivity measurements. However, the materials in ECs are mostly very porous, so that parts of the laser

beam just dissipate through the material. Furthermore, mostly the thermal conductivities of wetted materials are of interest in PEM cells, which can be partly dried out by the laser beam. Therefore, the laser flash technique is cannot be applied here. [30]
Another approach is the heat flux method, which is an ex-situ method that measures the temperature drop over a material sample between two pistons under a known heat flux. This method was applied in this study to allow measurements with high accuracy and at different compaction pressures. Thermal conductivities of dry and wet EC membrane, CL and PTL were measured to have reliable values for all layers to simulate the temperature distribution in the second part of this study. The apparatus used in this work to measure the thermal conductivities had already been validated in former studies [23, 39, 40] and is presented in the following sections.

3.1.1. Experimental setup

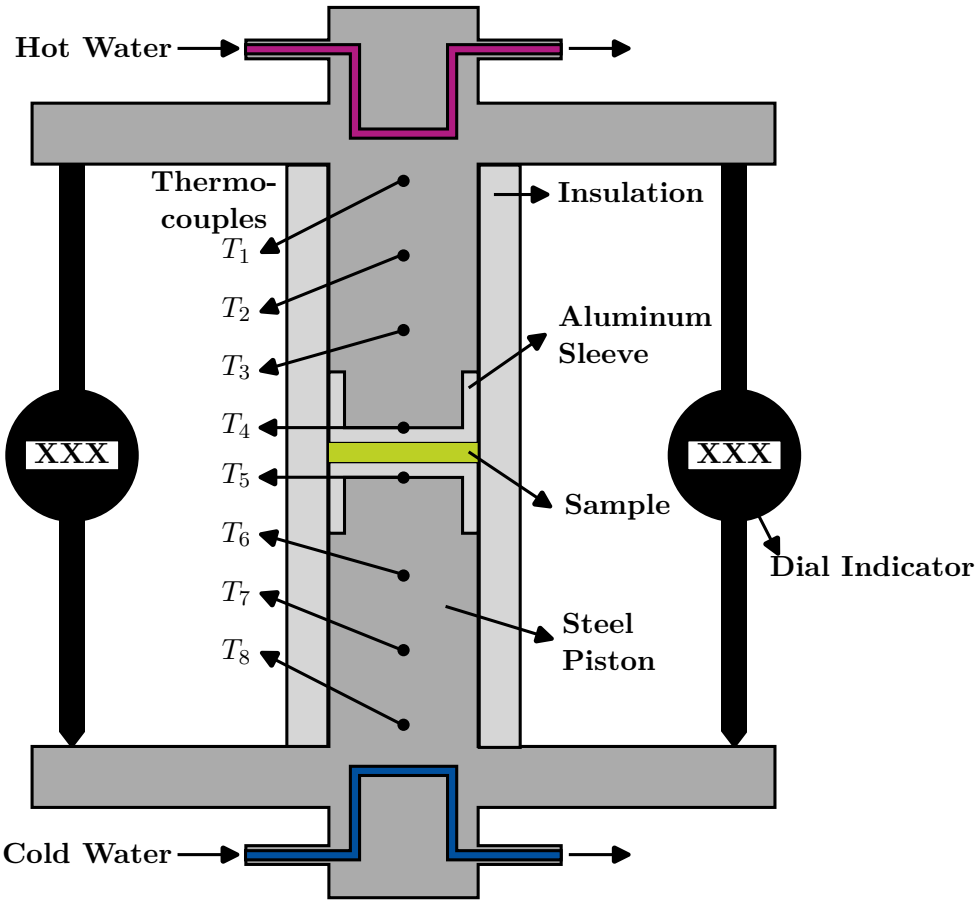

Figure 3.1.: Schematic thermal conductivity measurement setup

The thermal conductivities in this work were measured ex-situ using the heat flux method. A schematic of the apparatus used is given in figure 3.1. The apparatus consists of two steel pistons of (21.0 ± 0.1) mm diameter with thin aluminium sleeves at the contacting surfaces. The upper piston was heated to about 35 °C at the top and the lower piston cooled to about 10 °C at the bottom using temperature controlled water circuits to keep the aluminium sleeves close to ambient temperature to minimize heat exchange with the ambient. Additionally, the

pistons were thermally insulated against the ambient to further minimize heat exchange. Both pistons contained three type k thermocouples in the steel section ($T_1 - T_3$ and $T_6 - T_8$) with a distance Δx_{tc} of $(17.70 \pm 0.25)\,\mathrm{mm}$ and an accuracy of $\pm 0.05\,\mathrm{K}$. These thermocouples allowed the measurement of thermal gradients ΔT over the pistons and thus the determination of the heat flux $\dot{q}$ in each piston using the known thermal conductivity of steel κ_{steel} and Fourier's law of heat conduction (equation 2.1). The heat flux through the aluminium sleeves ($\dot{q}_{\mathrm{sample}}$) was assumed to be the mean of the heat fluxes through the pistons (equation 3.1).

$$\dot{q}_{\mathrm{sample}} = \frac{\kappa_{\mathrm{steel}}}{2} \left(\frac{\Delta T_{1-3}}{2\Delta x_{\mathrm{tc}}} + \frac{\Delta T_{6-8}}{2\Delta x_{\mathrm{tc}}} \right) \tag{3.1}$$

A round sample of 21 mm was inserted between the two aluminium sleeves and the thermal gradient was measured with two further thermocouples (T_4, T_5), which were located between the aluminium sleeves and the steel pistons. Because of the high thermal conductivity of the aluminium, it can be assumed to be isothermal, and the measured thermal gradient can be attributed to the thermal resistance of the sample R and the contact resistances R_{c} between the sample and the aluminium sleeves on both sides (equation 3.2).

$$R_{\mathrm{total}} = \frac{T_4 - T_5}{\dot{q}_{\mathrm{sample}}} = R + 2R_{\mathrm{c}} \tag{3.2}$$

In order to distinguish the contact resistance from the bulk resistance, samples of different thicknesses δ were measured. The thickness of the samples was measured outside the apparatus for a compaction pressure of 0 bar using an electronic micrometer (resolution 1 µm) and constantly during the testing in the apparatus under the respective pressures using two electronic gauges of the type Mitutoyo Digimatic Indicator ID-C Series 543, both with a resolution of 1 µm. The measured thermal resistances were then plotted over the sample thickness (figure 3.2). The axis intercept describes the total contact resistance $2R_{\mathrm{contact}}$, whereas the inverse of the slope describes the bulk thermal conductivity κ of the sample.
In order to examine the thermal resistances and compression of the samples at different compaction pressures, a pneumatic piston applied regulated compaction pressure up to 16 bar on the steel pistons.

3.1.2. Measurement procedure

Prior to the measurements, the rig was calibrated using samples of Polyether Ether Ketone (PEEK) with a known thermal conductivity of $\kappa = 0.25\,\mathrm{W\,m^{-1}\,K}$ [41, p. 266] in different thicknesses between 0.5 and 1.5 mm. The measurements were then conducted using the same procedure for each material:
First, a calibration of the digital gauges was conducted by applying all required pressure steps without a sample to exclude possible compaction of the rig through the applied pressure. Thereafter, samples of four thicknesses were measured, followed by another calibration without sample. Each calibration, as well as each measurement, was carried out at three different pressures

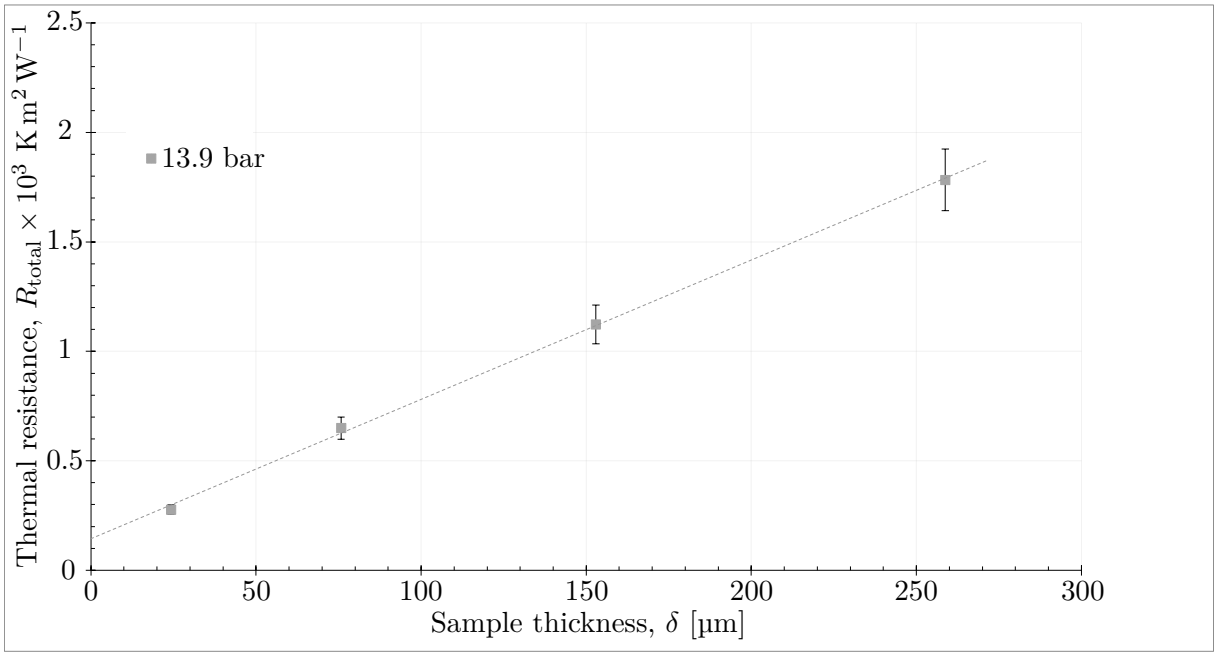

Figure 3.2.: Thermal resistance as a function of sample thickness

in increasing order. The pressures varied between FC- and EC-Materials and are summarized in table 3.1. For dry materials, the first pressure was held for 20 minutes, the second, and the third pressure for 15 minutes. Measurements were only carried out during the last five minutes of each pressure step to assure that stable temperature gradients had formed. The temperatures, pressures and gauge-readings were then recorded with a frequency of 10 Hz. After the highest pressure was measured, the pressure was again lowered to the first, lowest, pressure and the thickness was measured again to investigate possible hysteresis effects. As no thermal gradient was measured at this step, the pressure was only held for six minutes.

For the wet measurements, the pistons were sealed using Parafilm® around the aluminium section to minimize the dryout of the sample. The influence of the Parafilm® on the measurement was assessed as part of the calibration (cf. section 4.1.1). Furthermore, the holding time at each pressure step was reduced by five minutes compared to the dry measurements in order to further decrease the dryout during the measurements. The last pressure step, however, was held for ten minutes and thus longer than in the dry materials. A thermal conductivity measurement was conducted here in addition to the thickness measurement to assess the influence of the dryout during the measurements on the thermal conductivity.

In the subsequent sections, the specific measurement procedures for FC and EC materials are discussed.

Table 3.1.: Pressure steps of the conductivity measurements

Material group	Pressure 1 - time 1	Pressure 2 - time 2	Pressure 3 - time 3	Pressure 1 - time 4
FC dry	4.6 bar - 20 min	9.3 bar - 15 min	13.9 bar - 15 min	4.6 bar - 6 min
FC wet	4.6 bar - 15 min	9.3 bar - 10 min	13.9 bar - 10 min	4.6 bar - 10 min
EC dry	4.6 bar - 20 min	9.3 bar - 15 min	16 bar - 15 min	4.6 bar - 6 min
EC wet	4.6 bar - 15 min	9.3 bar - 10 min	16 bar - 10 min	4.6 bar - 10 min

Fuel cell materials

In order to verify the measurement procedure, a Nafion® 211 membrane and a slightly aged FC MEA from baltic FuelCells consisting of a Nafion® 212 membrane, a CCL with 0.3 mg Pt/cm^2 and an ACL with 0.1 mg Pt/cm^2 were measured. It was decided to measure a slightly aged MEA to include ageing effects during the first hours of operation and thus determine the thermal conductivities as close as possible to the real conditions in the FC. As only a membrane of single thickness was available for the measurements, samples of different thicknesses were created by stacking up to ten layers of membrane. The contact resistance between the single layers was assumed to be negligible because of the very flat and compressible surfaces, which were assumed to have a good contact once some pressure is applied. The MEA was also only available with layers of a single thickness. Stacks of one, two, three, and four layers of MEA were measured. The contact resistance between the samples of CLs can be neglected, as determined in [29]. The contact resistance between the membrane and CLs in the MEA was also assumed as negligible as the CLs were coated onto the membrane so that a good contact can be suspected.
The mean thermal conductivity and compressibility of the CLs was derived from the MEA measurements using the values measured for pure Nafion® membrane. The results were then compared to literature values to verify the measurement procedure. The calibrations and measurements for the FC materials were conducted at 4.6, 9.3 and 13.9 bar compaction pressure, around the usual compaction pressure in PEMFC stacks of about 10 bar [42]. These pressures also assure comparability to the findings of Burheim *et al.* [23, 29] who measured similar materials in the same apparatus at the same pressures.

For the wet measurements, the Nafion® 211 membrane was humidified by soaking the samples in purified water for one hour and removing excess water with a paper towel. The MEA was put into vacuum while soaking in purified water for one hour to allow the water to enter the hydrophobic structures of the CLs. In order to measure the amount of water in the samples, they were weighted before and after the thermal conductivity measurements, as well as after drying overnight. Using the swelling as a measure for the humidification level of Nafion® membrane was also examined, but dismissed as it was not reliable (cf. section 5.1.1).
In order to compare the wet thermal conductivity of CLs to literature, the humidification level was determined in water-molecules per sulphonic group (λ). For this, the total amount of sulphonic-group-containing Nafion® in the MEA must be known. Nafion® is used as a membrane,

but usually also as proton conducting ionomer in the CLs. Therefore, the Nafion® content in the CLs had to be determined to calculate the total amount in the MEA. Besides Nafion® , the CLs usually consist of platinum and carbon. [43, 44] The exact composition of the CLs was not disclosed by the manufacturer. In order to approximate the Nafion® content, the area density of dry Nafion® 212 ($\rho_{\mathrm{A,\ Nafion212}}$ =10 mg cm^{-2}) was taken from the manufacturer's specification. This area density was then subtracted from the measured area density of the dry MEA samples to derive the combined area density of ACL and CCL. A Nafion® content of about 33 wt.% was assumed in the CLs following recommendations in literature [43, 44]. Thus, 33 % of the combined area density of the CLs were added to the area density of Nafion® 212 to determine the total area density of Nafion®in the MEA. Using the wet (assuming $\lambda = 22$ [23]) and dry ($\lambda = 0$) weight of the Nafion® 211 samples, a constant ratio Ω between area density of water $\rho_{\mathrm{A,\ water}}$ per area density of Nafion® ($\rho_{\mathrm{A,\ Nafion}}$) and λ was calculated (equation 3.3).

$$\Omega = \frac{1}{\lambda}\frac{\rho_{\mathrm{A,\ water}}}{\rho_{\mathrm{A,\ Nafion}}} \tag{3.3}$$

It was simplified assumed that the Nafion® was evenly distributed over the MEA and λ was constant over the sample. With this assumption, λ was calculated with equation 3.3 using the calculated area density of Nafion in the MEA, the measured area density of water in the MEA after soaking ($\lambda = 22$) and the calculated value for Ω. This procedure cannot give the exact value for λ, as it highly depends on assumptions regarding the composition of the MEA, but was used to get an approximation of the humidification level for comparison with thermal conductivities measured in literature.

Electrolysis cell materials

Thermal conductivities of PEMEC materials have been far less investigated than their FC equivalents. The thermal conductivity of sintered titanium EC PTL has been studied by Bock *et al.* [7] and the conductivity of the often used Nafion® membranes is known from FC materials (cf. [23, 24, 25, 26]). However, the thermal conductivity of EC CLs has, to best of the author's knowledge, never been studied and simulations have been conducted with the assumption of a conductivity equal to the one in FCs [7], thus neglecting the difference in composition between FC and EC CLs. Therefore, a PEMEC MEA from FuelCellStore consisting of a Tion5-W PFSA membrane, an iridium ruthenium oxide anode and a platinum black cathode both with a loading of 3 mg cm^{-2} was used to approximate the thermal conductivity of the CLs. The thermal conductivity and compressibility of the membrane was determined in a second measurement using pure samples of the same membrane in 127 µm thickness and subtracted from the MEA measurements to determine the CL properties. As for the FC materials, the contact resistance between the CL and the membrane as well as between the CLs of the adjacent samples was assumed to be negligible as the materials were only available in a single thickness so that multiple samples had to be stacked to create samples of different thicknesses. The EC materials have been measured as delivered because no aged samples were available.

Electrolysers are usually operated at about 20 to 30 bar compaction pressure [45]. The maximal pressure assessed during the measurements has therefore been set to the maximal pressure of the rig of 16 bar. The examined pressures were thus 4.6, 9.3 and 16 bar. The samples have been humidified in the same way as the FC samples (cf. last section). As no literature was available regarding the λ-values of wetted Tion5 membrane, the λ-values could not be determined for the CLs.

As described above, the thermal conductivity of sintered titanium PTL has been measured ex-situ by Bock *et al.* [7] using the heat flux method. However, titanium felt PTL, which is another commonly used type of PTL in PEMECs, has only been studied in-situ by Schuler *et al.* [38] but never ex-situ under controlled conditions. Therefore, a platinized titanium fibre felt EC PTL of 250 µm is measured both dry and wet using the same procedure as before. The material was humidified by soaking it overnight in purified water and letting it soak under vacuum for another hour afterwards. The contact resistance between the samples has been assumed to be negligible as the PTL's fibrous structure is similar to the one of SIGRACET® PTL, which was proven in [23] to have a negligible contact resistance between samples of the same material. The porosity of the PTL was determined by measuring the weight after soaking in water and comparing it to the dry weight of the sample to determine the amount of water soaked into the sample. It was assumed that all void spaces had been filled with water so that the volume of the void spaces could be calculated from the amount of water in the sample. The total volume of the samples was calculated using the measured height and diameter.

During the wet thermal conductivity measurements, two mechanisms can lead to a dryout in the samples. Firstly, water can be pushed out of the sample through the application of compaction pressure so that a compressed sample contains a lower mass of water than a uncompressed one. This can be expected to also be the case in an EC stack, when compaction pressure is applied on the stack. Secondly, water can evaporate or flow out of the sample through insufficient sealing. This effect does not occur in EC operation, as water is constantly fed into the stack. The influence of the second mechanism on the measurement results must therefore be minimized and controlled during the measurements to ensure accuracy of the measurements. Because of the apparently high dryout in the EC materials (cf. section 5.1.2), all electrolysis materials were measured twice. Once, as described above, by humidifying the sample only before the first pressure step, and a second time by taking the samples out of the apparatus and re-humidifying them between each pressure step. With re-humidification, each pressure was held for 15 minutes, from which the last five minutes were used for measurements. The results of the two methods are then compared to determine the impact of dryout due to the second mechanism, which must be lower when re-humidifying the samples. The compressibility was only determined from the measurements without re-humidification, because the re-humidification process increased the uncertainty of the compression measurements, as the samples had to be re-inserted into the apparatus between the pressure steps.

3.2. Simulating temperature distribution within stack

As described in section 2.2.2, some models are available that simulate the temperature distribution within a single EC [7, 8, 9]. However, no models are known that use measured thermal conductivities of PEMEC materials for all layers in an EC, especially for the CLs usually values measured in FCs are used [7]. Furthermore, no models are known that predict the temperature distribution within the cells of an entire EC stack. This research gap should be closed in this work to provide detailed insights into the temperature distribution within the cells of an industrial-sized PEMEC stack to support the optimization of cell-compositions and operations management.

3.2.1. Model development

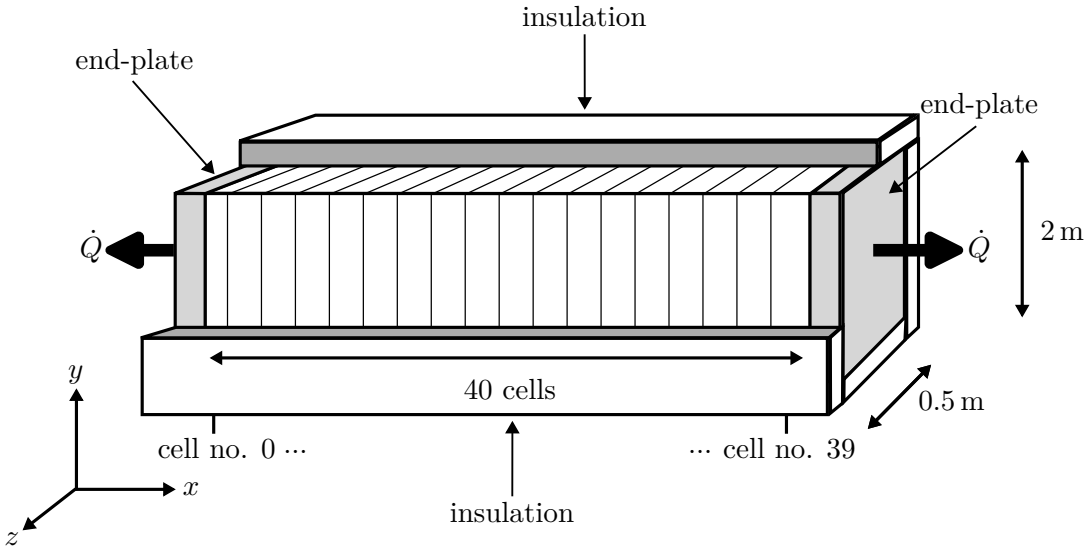

Figure 3.3.: Schematic of the simulated industrial-sized stack with $1\,m^2$ cell-area

A 2D steady-state numerical model was developed and implemented in Python. The basic equations and parameters were taken from the paper of Krenz *et al.* [5], who simulated the temperature distribution within an industrial-sized PEMEC stack but did not consider thermal gradients within the ECs in stacking direction. A schematic of the simulated stack simulated here is displayed in figure 3.3. The model considers stack- and along-the-channel-direction (x and y). Variations between the channels of the FF (z direction) were not assessed in this work. The stack was assumed to be perfectly insulated around the ECs (x and y direction). The ECs are clamped between two end-plates at the beginning and the end of the stack, which are not insulated towards the environment so that free convection was assumed to occur at the lateral faces of the end-plates. The model was validated using the temperature distributions given by Krenz *et al.* on a stack level and the temperature distribution within a single cell as predicted by Bock *et al.* [7] (cf. section 3.2.2). The thermal conductivities measured with the experimental setup described in section 3.1 were then used to model the temperature distribution within the stack in different scenarios (cf. 3.2.3).

Mesh

The mesh used in the model is depicted in figure 3.4 for a single EC and the two end-plates. The mesh of the single cell was then repeated for each EC of the stack ($N^{\text{cell}} = 40$ times) in x-direction between the two end-plates.

In x-direction, each mesh-cell describes a single EC-layer. The BPs were, however, divided into multiple layers: Two FFs and one part of solid BP in between. Each part has a thickness of one third of the BP's total thickness. The two FFs were again divided into three layers: The actual FF and one BL of $\delta^{\text{BL}} = 50\,\mu\text{m}$ on each side to account for the convective heat-transfer resistance between the fluid in the FF and the surrounding solids. The size of the boundary layer depends in reality on the exact flow-conditions inside the FF but was for simplicity here approximated by a constant value. In y-direction, each layer of the EC was divided into $N_{\text{mesh-cells,y}} = 21$ cells of the mesh to analyse the temperature variation along the channels of the FF.

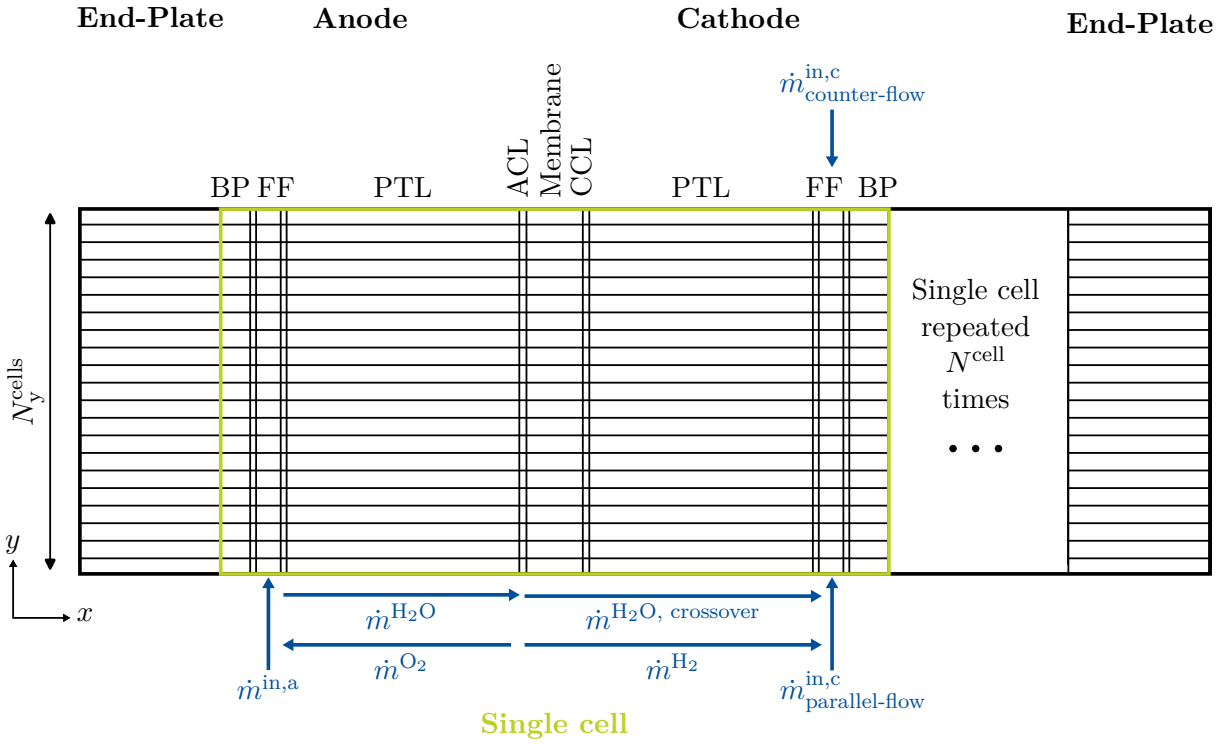

Figure 3.4.: Schematic of model's mesh and simulated mass flows

A frame of boundary cells was then added around the mesh to implement boundary conditions. Insulated boundaries were assumed on all sides. They were implemented in form of Neumann boundary conditions, setting the first derivative of the temperature at the boundary cells to zero. The only exception were the FF inlets, where the temperature in the boundary cell was set to the temperature of the incoming fluid using Dirichlet boundary conditions. The heat flux to the ambient in the end-plates was implemented in form of a source term (see section "Energy balance" in the following).

The temperatures were calculated on the boundaries of each mesh-cell, thus at the interface between two EC-layers. Energy exchange in form of heat fluxes and mass flows was considered

between the mesh-cells, and heat sources and sinks due to the electrolysis reactions were considered inside the mesh-cells. The equations used to describe these processes are presented in the following sections.

Mass balance

The simplified mass flows within a single EC of the simulation are depicted with the mesh in figure 3.4. In case of a parallel flow, the fluid inlet is at the first mesh-cell in y-direction on both the anode and cathode side of the bipolar plate. On the anode side water $\dot{m}_{\mathrm{H_2O}}^{\mathrm{in,\ a}}$ and some oxygen $\dot{m}_{\mathrm{O_2}}^{\mathrm{in,\ a}}$ is flowing into the FF of the EC. On the cathode side some water $\dot{m}_{\mathrm{H_2O}}^{\mathrm{in,\ c}}$ and hydrogen $\dot{m}_{\mathrm{H_2}}^{\mathrm{in,\ c}}$ flows into the FF. For following mesh-cells in y-direction, the products of the electrolysis reaction in the row below were added to and the educts were subtracted from the mass flow in the FF. The oxygen mass flow in the mesh-cell $y = j$ in an anodic FF was thus calculated with equation 3.4.

$$\dot{m}_{y=j}^{\mathrm{a,O_2}} = \dot{m}_{y=j-1}^{\mathrm{a,\ O_2}} + \dot{m}_{y=j-1}^{\mathrm{R,\ O_2}} \tag{3.4}$$

with the mass flow rate of oxygen $\dot{m}_{y=j-1}^{\mathrm{R,O_2}}$ produced in the row of mesh-cells below. It was calculated using the Faraday constant F, the cell area $A_{y=j-1}$ of the mesh-cell $y = j - 1$ using its size in y- and z-direction, the current density i and the molar mass of elementary oxygen $\mathrm{M}^{\mathrm{O_2}}$ (equation 3.5).

$$\dot{m}_{y=j-1}^{\mathrm{R,O_2}} = \frac{i * A_{y=j-1}}{4\mathrm{F}} * \mathrm{M}^{\mathrm{O_2}} \tag{3.5}$$

The mass flow of hydrogen on the cathode side was calculated analogously with equation 3.6.

$$\dot{m}_{y=j}^{\mathrm{c,H_2}} = \dot{m}_{y=j-1}^{\mathrm{c,H_2}} + \frac{i * A_{y=j-1}}{2\mathrm{F}} * \mathrm{M}^{\mathrm{H_2}} \tag{3.6}$$

The mass flow of water in the anodic FF decreases due to two effects. Firstly, water is used as educt in the electrolysis reaction $\dot{m}_{\mathrm{H_2O},y=j-1}^{\mathrm{R}}$ and secondly, water is dragged by the hydrogen-ions through the electrolysis membrane to the cathode side $\dot{m}_{\mathrm{H_2O},y=j-1}^{\mathrm{drag}}$ (equation 3.7).

$$\dot{m}_{y=j}^{\mathrm{a,H_2O}} = \dot{m}_{y=j-1}^{\mathrm{a,H_2O}} - \dot{m}_{y=j-1}^{\mathrm{R,H_2O}} - \dot{m}_{y=j-1}^{\mathrm{drag,H_2O}} \tag{3.7}$$

The mass flow of water consumed during the electrolysis reaction can be described analogously to the mass flow of hydrogen and oxygen with equation 3.8.

$$\dot{m}_{y=j-1}^{\mathrm{R,H_2O}} = \frac{i * A_{y=j-1}}{2\mathrm{F}} * \mathrm{M}^{\mathrm{H_2O}} \tag{3.8}$$

The water drag was modelled using the approach of Springer *et al.* [15], who postulated a mean of 2.5 water molecules to be dragged across the membrane with each hydrogen ion in a fully humidified membrane ($\lambda = 22$) under a linear decrease with humidification level (equation 3.9).

$$\dot{m}_{y=j-1}^{\mathrm{drag,H_2O}} = 2.5 * \frac{\lambda}{22} * \frac{i * A_{y=j-1}}{\mathrm{F}} * \mathrm{M}^{\mathrm{H_2O}} \tag{3.9}$$

The mass flow of water on the cathode side thus increases by the amount of water dragged through the membrane, and can be described with equation 3.10.

$$\dot{m}_{y=j}^{\mathrm{c,H_2O}} = \dot{m}_{y=j-1}^{\mathrm{c,H_2O}} + \dot{m}_{y=j-1}^{\mathrm{drag,H_2O}} \tag{3.10}$$

If the cell is operated in counter-flow, the same equations as before apply to the anodic FF but the cathodic FF is inverted in y-direction, so that the inlet is at the last mesh-cell in y-direction and the fluid flows in negative y-direction. The electrolysis reaction in the mesh-cells at $y = j+1$ was thus considered when calculating the mass flow in the mesh-cell $y = j$ in the cathode FF.

In the PTLs, CLs, the membrane and the FF-BLs facing towards the PTL, a mass flow in x-direction was considered. It was assumed that exactly the amount of water used in the electrolysis reaction and dragged through the membrane at $y = j$ flows in positive x-direction through the anode side FF-BL, the PTL and the ACL at $y = j$ while only the dragged water flows through the membrane, CCL, cathode side PTL and FF-BL. The oxygen produced in the electrolysis reaction in $y = j$ was considered to flow in negative x direction through the ACL and the anode-side PTL and FF-BL at $y = j$, while the hydrogen flows in positive x-direction through the membrane, CCL, cathode-side PTL and FF-BL.

The mass flow of water was further divided into gaseous and liquid water in each mesh-cell to account for evaporation and condensation heat. In order to calculate the amount of gaseous water in the fluid mixture, an ideal mixture of ideal gasses was assumed for the gaseous phase. The mass flow of water in the gas phase at saturation conditions was calculated by equation 3.11 for the cathode side and equation 3.12 for the anode side [5]. The equations were derived from the ideal gas law.

$$\dot{m}_{\mathrm{sat}}^{\mathrm{c}} = \frac{\mathrm{M}^{\mathrm{H_2O}}}{\mathrm{M}^{\mathrm{H_2}}} \frac{p_{\mathrm{sat}}^{\mathrm{H_2O}}}{p - p_{\mathrm{sat}}^{\mathrm{H_2O}}} \dot{m}^{\mathrm{H_2}} \tag{3.11}$$

$$\dot{m}_{\mathrm{sat}}^{\mathrm{a}} = \frac{\mathrm{M}^{\mathrm{H_2O}}}{\mathrm{M}^{\mathrm{O_2}}} \frac{p_{\mathrm{sat}}^{\mathrm{H_2O}}}{p - p_{\mathrm{sat}}^{\mathrm{H_2O}}} \dot{m}^{\mathrm{O_2}} \tag{3.12}$$

The saturation pressure of water $p_{\mathrm{sat}}^{\mathrm{H_2O}}$ was calculated using equation 3.13 as proposed by Roizard [46]. p was assumed to be ambient pressure all over the stack.

$$p_{\mathrm{sat}}^{\mathrm{H_2O}} = 133.3223684 * 10^{\frac{8.07131 - 1730.63}{T - 39.724}} \tag{3.13}$$

The actual flow of gaseous water was then taken from the smaller value of $\dot{m}_{\mathrm{sat}}$ and the total mass flow of water in the respective mesh-cell. The remainder of the total mass flow of water in the cell was considered to be present in form of liquid water.

Cell potential

As described in section 2.2.2, the cell potential consist of the reversible cell voltage $V_{\mathrm{rev}}^{\mathrm{cell}}$ and the activation- (μ_{act}), ohmic- (μ_{ohm}) and mass transfer (μ_{mt}) overpotentials (equation 2.15).

These potentials were calculated individually for each EC and every row in y-direction. The V-i characteristics were taken from Krenz *et al.* [5] for comparability.
The reversible cell voltage depends on the temperature and activity of the species taking part in the reaction and can be calculated using the Nernst-equation. If liquid water without gas bubbles is assumed in the CL, the Nernst equation can then be written in form of equation 3.14 [5, 47].

$$V_{\mathrm{rev}}^{\mathrm{cell}} = V_{\mathrm{rev}}^{\mathrm{cell},\Theta} + \frac{\mathrm{R}T^{\mathrm{cell}}}{2\mathrm{F}} \ln\left[\left(\frac{c_{\mathrm{sat}}^{\mathrm{c,\ H_2}}}{c_{\mathrm{sat}}^{\mathrm{c,\ H_2},\Theta}}\right)^{1}\left(\frac{c_{\mathrm{sat}}^{\mathrm{a,\ O_2}}}{c_{\mathrm{sat}}^{\mathrm{a,\ O_2},\Theta}}\right)^{\frac{1}{2}}\left(a^{\mathrm{a,H_2O}}\right)^{-1}\right] \tag{3.14}$$

The reversible cell potential at standard conditions $V_{\mathrm{rev}}^{\mathrm{cell},\Theta}$ was calculated from the Gibbs free energies at standard conditions (equation 2.10). R denotes the universal gas constant and F the Faraday constant. The mean temperature over the ACL, CCL and membrane T^{cell} was used as the temperature relevant for the reaction. The activity of the water $a^{\mathrm{a,H_2O}}$ can be assumed to be unity for liquid water. The concentrations of oxygen at the ACL and hydrogen at the cathode CCL can be assumed to be the saturation concentrations of the respective gas in water at a given temperature and pressure ($c_{\mathrm{sat}}^{\mathrm{a,\ O_2/c,\ H_2}}$) [5].
The saturation concentrations were calculated using the pressure p and Henry's coefficient H_{S} (equation 3.15, [5]). The stack was considered to be operated without pressurization and ambient pressure was assumed all over the stack. The temperature in the ACL was considered for the saturation concentration of oxygen, and the temperature in the CCL for the saturation concentration of hydrogen at non-standard conditions.

$$c_{\mathrm{sat}} = pH_{\mathrm{S}}(T) \tag{3.15}$$

Henry's coefficient was calculated using the approach published by Ito *et al.* [48] with equation 3.16 for hydrogen in water and equation 3.17 for oxygen in water.

$$H_{\mathrm{S}}^{\mathrm{H_2}}(T^{\mathrm{c}}) = \exp\left[-48.1611 + \frac{5528.45}{T^{\mathrm{c}}} + 16.8893 * \ln\left(\frac{T^{\mathrm{c}}}{100}\right)\right] * \frac{10}{18}\left[\frac{\mathrm{mol}}{\mathrm{m^3Pa}}\right] \tag{3.16}$$

$$H_{\mathrm{S}}^{\mathrm{O_2}}(T^{\mathrm{a}}) = \exp\left[-66.73538 + \frac{8747.547}{T^{\mathrm{a}}} + 24.45264 * \ln\left(\frac{T^{\mathrm{a}}}{100}\right)\right] * \frac{10}{18}\left[\frac{\mathrm{mol}}{\mathrm{m^3Pa}}\right] \tag{3.17}$$

The activation overpotential describes losses due to electrochemical reaction activation, and thus depends on the reaction rate. The relationship between the activation overpotential and the reaction rate, expressed in form of the current density, is described by the Butler-Volmer equation. It was simplified approximated with equation 3.18 by Krenz *et al.* to calculate the anodic activation overpotential [5]. For comparability, the same approach was used here.

$$\mu_{\mathrm{act}}^{\mathrm{a}} = \frac{\mathrm{R}T^{\mathrm{a}}}{2\alpha_{\mathrm{ct}}^{\mathrm{a}}\mathrm{F}} \ln\left(\frac{i}{i_0^{\mathrm{a}}}\right) \tag{3.18}$$

with the anodic charge transfer coefficient $\alpha_{\mathrm{ct}}^{\mathrm{a}}$ and the anodic exchange current density i_0^{a}. Both coefficients were calculated using an Arrhenius approach to include temperature effects (equation 3.19 and 3.20 [5]).

$$\alpha_{\mathrm{ct}}^{\mathrm{a}} = \alpha_{\mathrm{ct,\,ref}}^{\mathrm{a}} \exp\left[E_{\mathrm{ct}}^{\mathrm{a}}\left(\frac{1}{333.15\,\mathrm{K}} - \frac{1}{T^{\mathrm{a}}}\right)\right] \tag{3.19}$$

$$i_0^{\mathrm{a}} = i_0^{\mathrm{a,\,ref}} \exp\left[\frac{E_{\mathrm{cd}}^{\mathrm{a}}}{\mathrm{R}}\left(\frac{1}{353.15\,\mathrm{K}} - \frac{1}{T^{\mathrm{a}}}\right)\right] \tag{3.20}$$

Where $\alpha_{\mathrm{ct,\,ref}}^{\mathrm{a}}$ is the reference charge transfer coefficient at 333.15 K and $E_{\mathrm{ct}}^{\mathrm{a}}$ the activation energy for the charge transfer coefficient. $i_0^{\mathrm{a,\,ref}}$ is the reference anodic exchange current density at 353.15 K and $E_{\mathrm{cd}}^{\mathrm{a}}$ the activation energy for the anodic exchange current density. The values of these parameters depend on the electrochemical properties of the stack and must be fitted to the stack of interest. The parameters used in this study are presented in section 3.2.1.
Krenz *et al.* neglects the cathodic activation overpotential, which is small compared to the anodic activation overpotential. However, this overpotential might have an influence on the temperature distribution within the single ECs and was therefore included into this simulation. As no parameter values could be found in literature to use the equations above also for the cathodic overpotential, a slightly different definition was used here (equation 3.21 [18]).

$$\mu_{\mathrm{act}}^{\mathrm{c}} = \frac{\mathrm{R}T^{\mathrm{c}}}{\alpha_{\mathrm{ct}}^{\mathrm{c}}\mathrm{F}}\mathrm{arcsinh}\left(\frac{i}{2i_0^{\mathrm{c}}}\right) \tag{3.21}$$

The temperature dependency of the cathodic charge transfer coefficient $\alpha_{\mathrm{ct}}^{\mathrm{c}}$ is mostly neglected in literature due to its small impact and was therefore also not considered here [18]. The temperature dependency of the cathodic exchange current density was calculated in analogy to the anodic exchange current density with equation 3.22 [11].

$$i_0^{\mathrm{c}} = i_0^{\mathrm{c,\,ref}} \exp\left[\frac{E_{\mathrm{cd}}^{\mathrm{c}}}{\mathrm{R}}\left(\frac{1}{298.15\,\mathrm{K}} - \frac{1}{T^{\mathrm{c}}}\right)\right] \tag{3.22}$$

Where $E_{\mathrm{cd}}^{\mathrm{c}}$ is the activation energy for the cathodic exchange current density and $i_0^{\mathrm{c,\,ref}}$ the reference cathodic exchange current density at 298.15 K. The parameter values provided by Correa *et al.* [11] were used to calculate the cathodic activation overpotential as no experimental data was available to fit the overpotential to actual values of the simulated system. $\alpha_{\mathrm{ct,\,ref}}^{\mathrm{a}}$ was adjusted, so that the sum of the activation overpotentials was the same as the anodic activation overpotential described by Krenz *et al.* to not alter the V-i-characteristics.

The ohmic overpotential describes ohmic resistances against proton- and electron fluxes. However, as resistances of the electron fluxes are very small compared to ionic resistances, they are mostly neglected in literature [18]. Here, the two main resistances consisting of the ionic membrane resistance $R_{\mathrm{el}}^{\mathrm{mem}}$ and the ionic contact resistance $R_{\mathrm{el}}^{\mathrm{c}}$ were considered to calculate the ohmic

overpotential (equation 3.23 [5]).

$$\mu^{\mathrm{ohm}} = i\,(R_{\mathrm{el}}^{\mathrm{mem}} + R_{\mathrm{el}}^{\mathrm{c}}) \tag{3.23}$$

The contact resistance was assumed to be constant over the temperature and is listed in table 3.2. The ionic membrane resistance was calculated using the ionic conductivity of the membrane σ^{mem} and its thickness δ^{mem} (equation 3.24).

$$R_{\mathrm{el}}^{\mathrm{mem}} = \frac{\delta^{\mathrm{mem}}}{\sigma^{\mathrm{mem}}} \tag{3.24}$$

The ionic conductivity of the membrane depends on its humidification level in water molecules per sulfonic group λ and the temperature T^{mem}. The relationship can be estimated using the approach of Springer *et al.* [15] (equation 3.25).

$$\sigma^{\mathrm{mem}} = (K^{\mathrm{mem}}\lambda - 0.326)\exp\left[E^{\mathrm{mem}}\left(\frac{1}{303\mathrm{K}} - \frac{1}{T^{\mathrm{mem}}}\right)\right] \tag{3.25}$$

Where K^{mem} is a linear fitting factor and E^{mem} the activation energy (cf. table 3.2).

The mass transfer overpotentials gain significant impact on the cell voltage at high current densities when the reaction sites become overpopulated by reaction products so that the concentration of reactants decreases. Mass transfer overpotentials are usually estimated using the Nernst equation, and were here calculated using equation 3.26 for the anode side and equation 3.27 for the cathode side [5].

$$\mu_{\mathrm{mt}}^{\mathrm{a}} = \frac{\mathrm{R}T^{\mathrm{a}}}{4\mathrm{F}}\ln\left(\frac{c_{\mathrm{supersat}}^{\mathrm{a,\,O_2}}}{c_{\mathrm{sat}}^{\mathrm{a,\,O_2}}}\right) \tag{3.26}$$

$$\mu_{\mathrm{mt}}^{\mathrm{c}} = \frac{\mathrm{R}T^{\mathrm{c}}}{2\mathrm{F}}\ln\left(\frac{c_{\mathrm{supersat}}^{\mathrm{c,\,H_2}}}{c_{\mathrm{sat}}^{\mathrm{c,\,H_2}}}\right) \tag{3.27}$$

The saturated concentrations c_{sat} were calculated analogously to the saturated concentrations in the reversible cell potential using Henry's law (equation 3.15). The supersaturated concentrations describe the supersaturation of product gasses in the CL, which occur due to mass-transfer resistances. To calculate the concentrations in supersaturated state, the production rate was calculated from the current density. The mass flow away from the CL was considered towards the FF of the same electrode. Crossover of H_2 and O_2 through the membrane was here neglected. The supersaturated concentration were thus calculated using equation 3.28 [49].

$$c_{\mathrm{supersat}} = \frac{\frac{i}{z\mathrm{F}} + k_{\mathrm{l}}c_{\mathrm{sat}}}{k_{\mathrm{l}}} \tag{3.28}$$

Where z is the number of electrons transferred per molecule, thus $z = 4$ for O_2 and $z = 2$ for H_2. k_{l} is the mass transfer coefficient, which accounts for mass transport resistances such as desorption, diffusion and bubble formation, growth and detachment for the mass transport through CL and PTL to the FF [49].

Energy balance

After deriving the overpotentials, which act as heat sources in the EC, an energy balance can be drawn to determine heat fluxes and temperature gradients within the ECs. For this, heat sinks and sources were assigned to the relevant layers within the ECs. They were calculated individually for each row in y-direction using the prevailing conditions in this section of the respective EC. Besides the sources of heat described by the overpotentials, several heat sinks occur over the EC. As described in section 2.2.2, some heat is consumed by the endothermic electrolysis reaction. The remaining heat warms up the fluids flowing through the cell or exits the stack over the non-insulated end-plates.

The heat generated by a certain overpotential was calculated using the current flowing through the respective section of the EC with the current density, the area of the mesh-cell in y- and z-direction A and the overpotential calculated for the respective section (equation 3.29)

$$\dot{Q}_{\mathrm{overpot}} = iA\mu \tag{3.29}$$

The heat flow generated by the anodic activation- and anodic mass-transfer overpotentials was applied to the ACL. The heat flow from cathodic activation and cathodic mass-transfer overpotentials was applied to the CCL. Heat from ohmic overpotentials was employed to the membrane.

The molar reversible heat required for the electrolysis reaction $Q_{\mathrm{m,rev}}$ was calculated using equation 2.12 using the mean temperature T^{cell} over ACL, membrane and CCL. The entropies of the pure fluids at T^{cell} were calculated from the entropies at reference temperature $T_0 = 343.15\,\mathrm{K}$ using equation 3.30 with the isochoric molar heat capacity $C_{\mathrm{v,m}}$ at T_0. The isochoric heat capacity and the entropy at reference temperature were taken from the Cantera Python library.

$$S_{\mathrm{m}}(T^{\mathrm{cell}}) = S_{\mathrm{m}}(T_0) + C_{\mathrm{v,m}} \ln\left(\frac{T^{\mathrm{cell}}}{T_0}\right) \tag{3.30}$$

The reversible molar heat was then multiplied by the reaction rate in the relevant mesh-cell to derive the reversible heat flow $\dot{Q}_{\mathrm{rev}}$ (equation 3.31).

$$\dot{Q}_{\mathrm{rev}} = Q_{\mathrm{m,rev}} \frac{iA}{2\mathrm{F}} \tag{3.31}$$

Half of the heat flow was then applied as a sink to the ACL and half to the CCL as proposed by Bock *et al.* [7].

As described earlier, some heat was assumed to dissipate over the lateral faces of the stack's end-plates into the environment. This heat flow was assumed to occur mainly due to free convection of the ambient air. The heat transfer coefficient was presumed as $h_{\mathrm{t}} = 45\,\mathrm{W\,m^{-2}\,K^{-1}}$ as proposed by Krenz *et al.* [5]. The heat flux was then calculated from the difference in temperature between the outer side of the end-plates and ambient $T^{\mathrm{amb}} = 294.15\,\mathrm{K}$ using equation 2.5. The heat flow

was then derived with the area of the respective mesh-cell using the sizes in y- and z-direction. The calculated heat flow was applied in form of a heat sink to the end-plates in the simulation.

Using the mass flows within the ECs in x- and y-direction as well as the respective temperatures, an enthalpy balance was drawn for each mesh-cell by summing up the enthalpies of incoming and outgoing mass flows to account for heat transported by the mass flow. An ideal mixture was assumed for all fluids and the total change in enthalpy was calculated by setting up an energy balance for each component α in the fluid (equation 3.32). Due to energy conservation, the total change in enthalpy equals the amount of heat exchanged with the fluids. This heat-flow was applied as a source/sink to the respective mesh-cell.

$$\dot{Q} = \sum_{\alpha,\mathrm{Out}} h^{\alpha}_{\mathrm{Out}} * \dot{m}^{\alpha}_{\mathrm{Out}} - \sum_{\alpha,\mathrm{In}} h^{\alpha}_{\mathrm{In}} * \dot{m}^{\alpha}_{\mathrm{In}} \tag{3.32}$$

The specific enthalpies $h^{\alpha}_{\mathrm{In/Out}}$ of the component α were calculated from the enthalpy h^{α}_{0} at reference temperature $T_0 = 343.15\,\mathrm{K}$ assuming ideal gasses and incompressible fluids. For gasses, the specific isobaric heat capacity c_{p} was used (equation 3.33). For liquids, the specific isochoric heat capacity c_{v} was considered (equation 3.34).

$$h^{\alpha}_{\mathrm{In/Out}} = h^{\alpha}_{0} + c^{\alpha}_{\mathrm{p}} * \left(T_{\mathrm{In/Out}} - T_0\right) \tag{3.33}$$

$$h^{\alpha}_{\mathrm{In/Out}} = h^{\alpha}_{0} + c^{\alpha}_{\mathrm{v}} * \left(T_{\mathrm{In/Out}} - T_0\right) \tag{3.34}$$

The enthalpies at reference temperatures as well as the specific heat capacities at T_0 were calculated using the Cantera library in Python.
It was simplified assumed, that the fluids have the same temperature as the solids in the respective mesh-cell. Determining the actual fluid-temperature would require deep knowledge about the flow conditions within the different EC layers and the complex heat transfer mechanisms within the porous structures, which are still subject of ongoing research [5].

In order to evaluate and compare the efficiency of the electrolysis reaction within the different scenarios of the simulation, the voltage efficiency according to the higher heating value $\epsilon^{\mathrm{HHV}}_{\mathrm{V}}$ is used. It is calculated using the cell voltage and the thermo-neutral voltage (equation 3.35) [5]. The efficiency is derived separately for every row in y-direction in every EC in the stack. The arithmetic mean of all calculated values is then used as the stack's voltage efficiency.

$$\epsilon^{\mathrm{HHV}}_{\mathrm{V}} = \frac{V_{\mathrm{thn}}}{V^{\mathrm{cell}}} \tag{3.35}$$

After applying all sources and sinks to the mesh, the resulting heat fluxes between the mesh-cells and thus the temperature gradients could be derived.

Heat transfer

In order to describe the temperature field due to conduction with sources and sinks, the Fourier-Biot equation was derived by setting up a three-dimensional energy-balance based on Fourier's law [50, pp. 57 sq.]. Assuming a constant temperature in z-direction, the correlation can be written in form of equation 3.36 to describe a two-dimensional temperature distribution in x- and y-direction.

$$\frac{1}{\alpha}\frac{\partial T}{\partial t} = \kappa_{\mathrm{x}}\frac{\partial^2 T}{\partial x^2} + \kappa_{\mathrm{y}}\frac{\partial^2 T}{\partial y^2} + \dot{q} \tag{3.36}$$

Where t is the time, $\kappa_{\mathrm{x/y}}$ the thermal conductivity in x and y direction, $\dot{q}$ heat flux source term and α the thermal diffusivity, which depends on the heat capacity and thermal conductivity of the material.

The thermal conductivities measured in this study for membrane and CLs were used both in x- and y-direction, as isotropic thermal conductivities are commonly assumed for these materials in literature [6, 7, 51]. It was assumed that the thermal conductivity of the ACL and CCL are the same, as both CLs usually have a similar composition [4]. The thermal conductivity in carbon fibre based FC PTL is highly anisotropic, and the thermal conductivity is by a factor ten higher in-plane than the through-plane conductivity [7]. For sintered EC PTL, however, Bock *et al.* [7] postulated isotropic properties. Because of the fibrous structure of the titanium felt PTL ([35]), an anisotropic behaviour similar to the one in carbon fibre was assumed. The measured through-plane conductivity was therefore used as κ_{x} in the PTLs and the in-plane thermal conductivity κ_{y} was assumed to be ten times κ_{x}. For all layers wet thermal conductivities at 16 bar compaction pressure were used to best mimic the conditions within the actual EC with compaction pressures of 20 to 30 bar [45]. Contact resistances between the single layers were assumed to be negligible.

The thermal conductivities for the isotropic stainless steel bipolar plates were taken from literature. In the FFs, the thermal conductivity was assumed to be half the value of pure stainless steel, with the assumption of half the cell area being ribs out of stainless steel and half of the cell area being channels with negligible across-the-channel conductivity. The thermal conductivity in the BLs of the FFs was fitted using literature values for temperature gradients between fluid in the FF and adjacent solids in EC FFs [7].

All mentioned parameter-values are summarized in table 3.2 for constant parameters and in table 3.3 and 3.4 for varied parameters.

Solver

In order to apply the Fourier-Biot equation to the mesh and solve it using the Euler method, the equation was discretised using second order finite differences in space and first order forward differences in time (equation 3.37). As the heat capacity was unknown for most layers of the EC, the time-step was combined with the thermal diffusivity of the Fourier-Biot equation to the equivalent time-step Δt_{e}. As only the steady-state temperature is of interest, the resulting

distortion in time-dimension is not relevant.

$$T_{i,j}^{n+1} = T_{i,j}^{n} + \Delta t_{\mathrm{e}} \left[\frac{\kappa_{\mathrm{x},i,j} \frac{T_{i+1,j}-T_{i,j}}{x_{i+1,j}-x_{i,j}} + \kappa_{\mathrm{x},i-1,j} \frac{T_{i-1,j}-T_{i,j}}{x_{i,j}-x_{i-1,j}}}{x_{i+1,j} - x_{i,j}} + \frac{\kappa_{\mathrm{y},i,j} \frac{T_{i,j+1}-T_{i,j}}{y_{i,j+1}-y_{i,j}} + \kappa_{\mathrm{y},i,j-1} \frac{T_{i,j-1}-T_{i,j}}{y_{i,j}-y_{i,j-1}}}{y_{i,j+1} - y_{i,j}} + \dot{q} \right] \tag{3.37}$$

with the iteration n, the position in x-direction i, and the position in y-direction j. The volume specific heat flux $\dot{q}$ applies the calculated heat sources and sinks to the temperature field. The scheme is stable under condition 3.38 [52].

$$\Delta t_{\mathrm{e}} \leq \frac{1}{4 \left[\max\left(\frac{\kappa_{\mathrm{x}}}{\Delta x^2}\right) + \max\left(\frac{\kappa_{\mathrm{y}}}{\Delta y^2}\right) \right]} \tag{3.38}$$

Equation 3.37 was then solved iteratively until the convergence criteria $|T^{n+1} - T^{n}| < \epsilon_{\mathrm{T}}$, with the maximal allowable temperature change per iteration ϵ_{T}, was fulfilled. In each iteration all source terms were recalculated as depicted in the flowchart (figure 3.5) before calculating the temperature step. The size of the time-step was chosen to the maximal value within the stable region to minimize the number of required iterations.

The cell voltage is usually given through the power electronics and is, due to the high electric conductivity of the BPs, uniform over each cell [5]. In order to derive the current densities under the respective conditions in every mesh-cell, the current density was iterated together with the temperature using the ratio between the voltage calculated from reversible cell voltage and overpotentials $V^{\mathrm{cell},n}$ and the voltage set-point $V_{\mathrm{set}}^{\mathrm{cell}}$ (equation 3.39).

$$i^{n+1} = i^{n} \frac{V_{\mathrm{set}}^{\mathrm{cell}}}{V^{\mathrm{cell},n}} \tag{3.39}$$

In order to ensure sufficient convergence for the current density, a second convergence criteria was implemented: $|i^{n+1} - i^{n}| < \epsilon_{\mathrm{i}}$. ϵ_{i} and ϵ_{T} were chosen individually for every simulation case to ensure convergence (cf. section 3.2.2).

Parameters

Most parameters for the calculations described in the last sections were taken from the study of Krenz *et al.* [5] to ensure comparability to literature. Some parameters, which are only relevant on a cell-level and thus not considered by Krenz *et al.* were taken from other studies.
Some parameters were varied in different simulated scenarios to assess their effect on the temperature distribution. These parameters are discussed in section 3.2.2 and section 3.2.3. All other parameters are summarized in table 3.2.

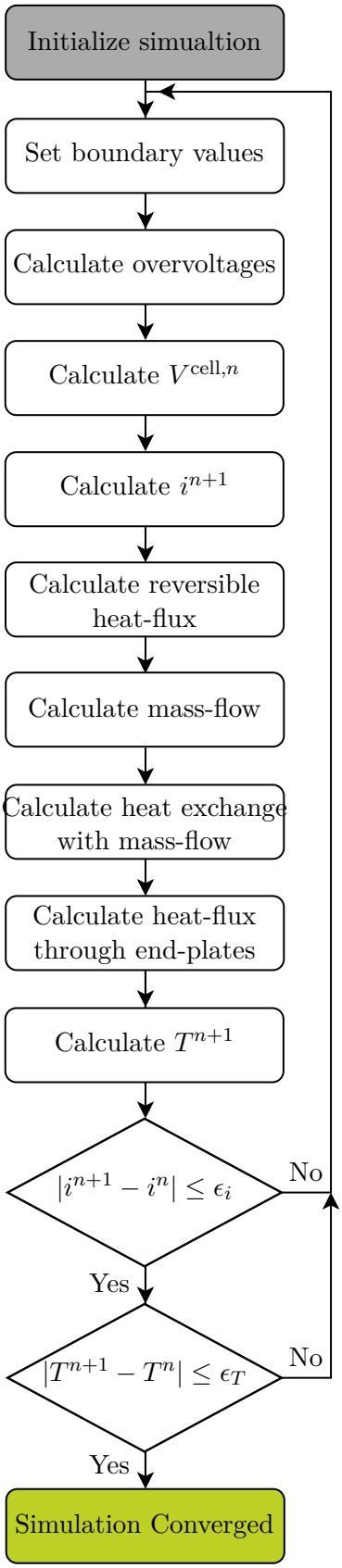

Figure 3.5.: Flowchart of simulation

Table 3.2.: Simulation parameters not varied between simulation cases

Symbol	Description	Value	Unit	Source
$\alpha^{\mathrm{a}}_{\mathrm{ct,\ ref}}$	Reference anode charge transfer coefficient at 333.15 K	0.515	-	fitted
$\alpha^{\mathrm{c}}_{\mathrm{ct}}$	Cathode charge transfer coefficient	0.50	-	[11]
δ^{BL}	Thickness of BL	50	µm	[7]
δ^{EP}	Thickness of end-plate	50	mm	[5]
κ^{BP}	Thermal conductivity of BP-layer without FFs (stainless steel)	15	$\mathrm{W\,m^{-1}\,K^{-1}}$	[5]
κ^{EP}	Thermal conductivity of end-plate (stainless steel)	15	$\mathrm{W\,m^{-1}\,K^{-1}}$	[5]
κ^{FF}	Thermal conductivity of FF without boundary-layer	7.5	$\mathrm{W\,m^{-1}\,K^{-1}}$	$\frac{1}{2}\kappa^{\mathrm{BP}}$
λ	Water molecules per sulphonic group in Nafion®	22	-	[23]
$E^{\mathrm{a}}_{\mathrm{cd}}$	Activation energy for the anodic current density	4300	-	[5]
$E^{\mathrm{c}}_{\mathrm{cd}}$	Activation energy for the cathodic current density	15070	-	[11]
$E^{\mathrm{a}}_{\mathrm{ct}}$	Activation energy for the anodic charge transfer coefficient	510	-	[5]
E^{mem}	Activation energy for the membrane conductivity	1268	-	[5]
h^{BL}	Heat transfer coefficient of boundary-layer	4000	$\mathrm{W\,m^{-2}\,K^{-1}}$	Fitted to [7]
h^{EP}	Heat transfer coefficient of end-plate to ambient	45	$\mathrm{W\,m^{-2}\,K^{-1}}$	[5]
$i_0^{\mathrm{a,\ ref}}$	Reference anodic exchange current density at 353.15 K	$8 * 10^{-5}$	$\mathrm{A\,m^{-2}}$	[5]
$i_0^{\mathrm{c,\ ref}}$	Reference cathodic exchange current density at 298.15 K	32401	$\mathrm{A\,m^{-2}}$	[11]
k_{l}	Mass transport coefficient in catalyst layer	0.023	$\mathrm{m\,s^{-1}}$	fitted within range from [49]
K^{mem}	Linear fitting factor for membrane conductivity	0.5139	$\Omega\,\mathrm{m^{-1}}$	[5]
l_{y}	EC-size in y-direction	2	m	[5]
l_{z}	EC-size in z-direction	0.5	m	[5]
$N_{\mathrm{mesh\text{-}cells,y}}$	Number of mesh-cells in y-direction	21	-	-
p	Fluid pressure in stack (absolute)	101325	Pa	-
$R_{\mathrm{el,c}}$	Ionic contact resistance membrane to CLs	$4.6 * 10^{-6}$	$\Omega\,\mathrm{m^{-2}}$	[5]

3.2.2. Model validation

In order to verify that the results of the simulation depict the actual conditions within a PEMEC stack, different measures were taken. Firstly, the convergence of the simulation was verified for each simulation cycle. Secondly, different tests were conducted as part of a validation procedure to verify the implementation of the simulation: A mesh refinement study was carried out, the implementation was tested using high and low thermal conductivity values and as a last step, the simulated temperature distribution was compared to literature.

In order to ensure sufficiently small convergence criteria ϵ_T and ϵ_i and thus convergence of the simulation, it was inspected that the temperatures and current densities in the mesh did not relevantly change during the last 10 % of iterations. If the temperatures did change more than 0.05 K or the current density more than $0.001\,\mathrm{A\,cm^{-2}}$ within these iterations, the simulation was repeated with lower values for ϵ_T and ϵ_i. Additionally, the energy balance was inspected to ensure that the total difference between heat produced by sources and heat consumed by sinks in one EC was below 0.1 % of the maximal amount of heat produced in a single mesh-cell. If the difference was higher, the simulation was repeated with lower values for ϵ_T and ϵ_i. These tests were conducted for every simulated scenario to ensure convergence.

As part of the validation procedure after implementation of the model, a mesh refinement study was carried out for a stack in counter-flow by doubling the number of mesh cells in y-direction to $N_\mathrm{mesh\text{-}cells,y} = 42$. This was done to rule out possible influences of the mesh on the results of the simulation. The number of mesh cells in x-direction was not part of the mesh-refinement study, as the temperature gradient within the single layers of the cell was approximated to be linear because the heat transport is assumed to occur mainly due to conduction with constant thermal conductivity within each layer. Counter-flow was chosen here as it shows a more complex temperature distribution over the ECs and thus requires a finer resolution than parallel flow.
In order to verify the correct implementation in principle, one simulation run was then conducted for parallel flow assuming a high conductivity of $15\,\mathrm{W\,m^{-1}\,K^{-1}}$ in all layers (except of FFs and FF-BLs) and another simulation assuming a low conductivity of $2\,\mathrm{W\,m^{-1}\,K^{-1}}$. The results were then compared to inspect compatibility with physical principles. The conductivity in the FF was always set to half the conductivity of the BP (cf. section 3.2.1) and the thermal conductivity in the BLs was kept at the constant value listed in table 3.2 to take the physical correlations into account as described in section 3.2.1. Parallel flow was chosen here for simpler gradients within the cells that were better suited to test the correctness of the implementation in principle.

Lastly, in order to verify the assumptions made during modelling, the results were compared to literature. As not sufficient data was available from measurements regarding the temperature distribution within ECs, the simulated temperatures were compared to predictions from validated models, both on a cell- and stack-level.
The temperature distribution within a single PEMEC has been modelled by Bock *et al.* [7] in stacking direction and between the channels of the FF (x- and z-direction). The model of this

thesis was fed with the thermal conductivities, fluid temperature and layer-thicknesses used by Bock *et al.* and solved for a single cell without end-plates to replicate the results. The mass flow in the FFs was set to a high value to assure a constant temperature of 80 °C in the FFs over the entire ECs to produce a situation similar to the one described by Bock *et al.*, where gradients along the channel are not considered. The simulation was conducted two times at a current density of $3\,\mathrm{A\,cm^{-2}}$, firstly using simple overpotentials as proposed by Bock *et al.* for best comparability and secondly using the overpotentials of this model as described in section 3.2.1. A cross-section through all layers in the middle of the EC ($y = 1\,\mathrm{m}$) was then compared to the results of Bock *et al.* for the three PTLs with different thermal conductivities measured by Bock *et al.* to verify the model on an EC-level.

The temperature within an industrial-sized EC stack has been modelled by Krenz *et al.* [5] for parallel and counter-flow, assuming a constant temperature within each EC of the stack. The model of this study was fed with the parameters used by Krenz *et al.* and solved for both flow arrangements in the stack including end-plates as described in section 3.2.1. The thicknesses of the CLs were estimated, as they were not given by Krenz *et al.* The temperature and current density distribution over the stack were simulated at $2\,\mathrm{A\,cm^{-2}}$ and compared to the results of Krenz *et al.* to verify the model on a stack-level.

The parameters used to reproduce the results from Bock *et al.* and Krenz *et al.* are summarized in table 3.3.

Table 3.3.: Parameters used for model validation with [5] and [7]

Symbol	Description	Value Bock *et al.* [7]	Value Krenz *et al.* [5]	Unit
κ^{CL}	Thermal conductivity of ACL / CCL	0.54	7	$\mathrm{W\,m^{-1}\,K^{-1}}$
κ^{MEM}	Thermal conductivity of membrane	0.25	2.5	$\mathrm{W\,m^{-1}\,K^{-1}}$
$\kappa_{\mathrm{x}}^{\mathrm{PTL}}$	Thermal conductivity of PTL in x-direction	5.6; 6.9; 8.2	7	$\mathrm{W\,m^{-1}\,K^{-1}}$
$\kappa_{\mathrm{y}}^{\mathrm{PTL}}$	Thermal conductivity of PTL in y-direction	5.6; 6.9; 8.2	7	$\mathrm{W\,m^{-1}\,K^{-1}}$
δ^{BP}	Thickness of BP without FFs	0.87	0.67	mm
$\delta^{\mathrm{CL,a}}$	Thickness of ACL	10	15	µm
$\delta^{\mathrm{CL,c}}$	Thickness of CCL	20	15	µm
δ^{FF}	Thickness FF without BL	0.77	0.57	mm
δ^{MEM}	Thickness membrane	127	100	µm
δ^{PTL}	Thickness of PTL	1.5	4.935	mm
$\dot{m}_{\mathrm{in}}^{a,\mathrm{H_2O}}$	Mass flow water into anodic FF per cell	0.1	0.15	$\mathrm{kg\,s^{-1}}$
$\dot{m}_{\mathrm{in}}^{a,\mathrm{O_2}}$	Mass flow oxygen into anodic FF per cell	10^{-6}	10^{-5}	$\mathrm{kg\,s^{-1}}$
$\dot{m}_{\mathrm{in}}^{c,\mathrm{H_2O}}$	Mass flow water into cathodic FF per cell	0.1	0.15	$\mathrm{kg\,s^{-1}}$
$\dot{m}_{\mathrm{in}}^{a,\mathrm{H_2}}$	Mass flow hydrogen into cathodic FF per cell	10^{-3}	10^{-5}	$\mathrm{kg\,s^{-1}}$
N^{cell}	Number of cells in the stack	1	40	-
$T_{\mathrm{in}}^{\mathrm{m,a}}$	Temperature of fluid at anodic inlet	353.15	333.15	K
$T_{\mathrm{in}}^{\mathrm{m,c}}$	Temperature of fluid at cathodic inlet	353.15	333.15	K
$V_{\mathrm{set}}^{\mathrm{cell}}$	Set-point cell voltage	2.34	1.965; 1.971 (par, counter)	V

3.2.3. Simulated scenarios

After validating the model, the impact of different parameters on the temperature distribution over the stack was investigated. Therefore, six different scenarios were defined. Each scenario was simulated twice, once in parallel and once in counter-flow. Firstly, a simulation was conducted to predict the temperature distribution within the stack described by Krenz *et al.* [5] using the thermal conductivities at the upper boundary of uncertainty measured in this study ("Max. measured conductivities"). This scenario was used as the base scenario, and only single parameters were varied in the other scenarios. The results were then compared back to this scenario.
It was assumed that all ECs in the stack are fully wetted throughout all layers as both FFs are flooded with water. Thus, thermal conductivities measured on the fully wetted materials at 16 bar compaction pressure were used. The current density was always kept at $2.0\,\mathrm{A\,cm^{-2}}$ by varying the cell voltage in the simulated scenarios. The individual parameter values used in each scenario are listed in table 3.4.

In a second scenario, the thermal conductivity values at the lower boundary of uncertainty measured in this study were used to determine the impact of the uncertainty of measurement on the predicted thermal gradients ("Min. measured conductivities").
A third scenario was set up to compare the titanium felt PTL used in the other scenarios to a sintered titanium PTL ("Sinter PTL"). The mean values of the thermal conductivities of wet sintered PTL measured by Bock *et al.* [7] were here used for both anodic and cathodic PTL. The same thermal conductivity values were used both for in- and through-plane conductivities, as isotropic behaviour was postulated by Bock *et al.* for the sintered PTL.
In order to determine the impact of higher current densities on the maximal temperatures in parallel and counter-flow, the current density was increased to $3\,\mathrm{A\,cm^{-2}}$ in a fourth scenario ("High current density").
In a fifth scenario, the impact of the water drag through the membrane on the temperature distribution within the ECs was investigated. For this, the first scenario was simulated again without consideration of the water drag ("Without water drag"). As all parameters were the same as in "Max. measured conductivities", this scenario is not listed in table 3.4. It was only simulated for parallel flow, as the simpler gradients within the EC made it easier to understand the interconnections between water drag and heat distribution within the ECs along the channels.
In a sixth scenario, the temperature was increased by 3 K at the inlet of the cathodic FF and decreased by 3 K at the inlet of the anodic FF to investigate the impact on the temperature gradient inside the MEA and possible benefits on efficiency ("Warmer cathode").

Table 3.4.: Parameters used for simulation

Symbol	Description	Max. measured conductivities	Min. measured conductivities	Sinter PTL	High current density	Warmer cathode	Unit
κ^{CL}	Thermal conductivity of ACL / CCL	0.222	0.164	0.222	0.222	0.222	$\mathrm{W\,m^{-1}\,K^{-1}}$
κ^{MEM}	Thermal conductivity of membrane	0.324	0.302	0.324	0.324	0.324	$\mathrm{W\,m^{-1}\,K^{-1}}$
$\kappa_{\mathrm{x}}^{\mathrm{PTL}}$	Thermal conductivity of PTL in x-direction	2.884	2.458	7	2.884	2.884	$\mathrm{W\,m^{-1}\,K^{-1}}$
$\kappa_{\mathrm{y}}^{\mathrm{PTL}}$	Thermal conductivity of PTL in y-direction	28.84	24.58	7	28.84	28.84	$\mathrm{W\,m^{-1}\,K^{-1}}$
δ^{BP}	Thickness of BP without FFs	0.67	0.67	0.67	0.67	0.67	mm
$\delta^{\mathrm{CL,a}}$	Thickness of ACL	15	15	15	15	15	µm
$\delta^{\mathrm{CL,c}}$	Thickness of CCL	15	15	15	15	15	µm
δ^{FF}	Thickness FF without BL	0.57	0.57	0.57	0.57	0.57	mm
δ^{MEM}	Thickness membrane	100	100	100	100	100	µm
δ^{PTL}	Thickness of PTL	4.935	4.935	4.935	4.935	4.935	mm
$\dot{m}_{\mathrm{in}}^{a,\mathrm{H_2O}}$	Mass flow water into anodic FF per cell	0.15	0.15	0.15	0.15	0.15	$\mathrm{kg\,s^{-1}}$
$\dot{m}_{\mathrm{in}}^{a,\mathrm{O_2}}$	Mass flow oxygen into anodic FF per cell	10^{-5}	10^{-5}	10^{-5}	10^{-5}	10^{-5}	$\mathrm{kg\,s^{-1}}$
$\dot{m}_{\mathrm{in}}^{c,\mathrm{H_2O}}$	Mass flow water into cathodic FF per cell	0.15	0.15	0.15	0.15	0.15	$\mathrm{kg\,s^{-1}}$
$\dot{m}_{\mathrm{in}}^{a,\mathrm{H_2}}$	Mass flow hydrogen into cathodic FF per cell	10^{-5}	10^{-5}	10^{-5}	10^{-5}	10^{-5}	$\mathrm{kg\,s^{-1}}$
N^{cell}	Number of cells in the stack	40	40	40	40	40	-
$T_{\mathrm{in}}^{\mathrm{m,a}}$	Temperature of fluid at anodic inlet	333.15	333.15	333.15	333.15	330.15	K
$T_{\mathrm{in}}^{\mathrm{m,c}}$	Temperature of fluid at cathodic inlet	333.15	333.15	333.15	333.15	336.15	K
$V_{\mathrm{set}}^{\mathrm{cell}}$	Set-point cell voltage (parallel, counter-flow)	1.964, 1.959	1.9615, 1.956	1.973, 1.966	2.062, 2.054	1.964, 1.959	V

4. Results

4.1. Measured thermal conductivity and compressibility

Thermal conductivities and compressibilities of the materials-layers used in PEM FCs and ECs were measured ex-situ using the heat-flux method. Below, first the results of the calibration using PEEK are presented followed by the measurements for FC and EC materials.

4.1.1. PEEK calibration

After the calibration, the maximum deviation between the measured thermal conductivity of PEEK and the literature value of $\kappa = 0.25\,\mathrm{W\,m^{-1}\,K^{-1}}$ [41, p. 266] was less than $0.005\,\mathrm{W\,m^{-1}\,K^{-1}}$ and thus below the uncertainties of measurement. The measured values are to be found in table 4.1.
Thereafter, the conductivity of the PEEK samples was measured again with a Parafilm® sealing around the Aluminium rods to imitate the conditions during wet measurements. The measured conductivities are listed along with the unsealed measurements in table 4.1. The mean deviation to the measurements without sealing was below $0.002\,\mathrm{W\,m^{-1}\,K^{-1}}$, and thus below the uncertainties of the measurement. The influence of the Parafilm® sealing on the measured thermal conductivities was therefore negligible.

Table 4.1.: Measured thermal conductivities of PEEK in $\mathrm{W\,m^{-1}\,K^{-1}}$ at different compaction pressures

Material	4.6 bar	9.3 bar	13.9 bar
PEEK	0.253 ± 0.069	0.249 ± 0.034	0.250 ± 0.029
PEEK sealed	0.249 ± 0.026	0.249 ± 0.018	0.250 ± 0.017

4.1.2. FC materials

The thermal conductivities measured for the FC components are depicted in figure 4.1 and listed in table A.1 in the appendix. The measured compressibilities are listed in table 4.2.
The dry Nafion® 211 showed a thermal conductivity of about $(0.18 \pm 0.01)\,\mathrm{W\,m^{-1}\,K^{-1}}$ with no significant influence of the pressure. A compression of about $(12 \pm 10)\,\%$ was measured under slight pressure of 4.6 bar, which did not significantly change when applying more pressure. The thermal conductivity of wet Nafion® 211 was with $(0.26 \pm 0.02)\,\mathrm{W\,m^{-1}\,K^{-1}}$ significantly higher

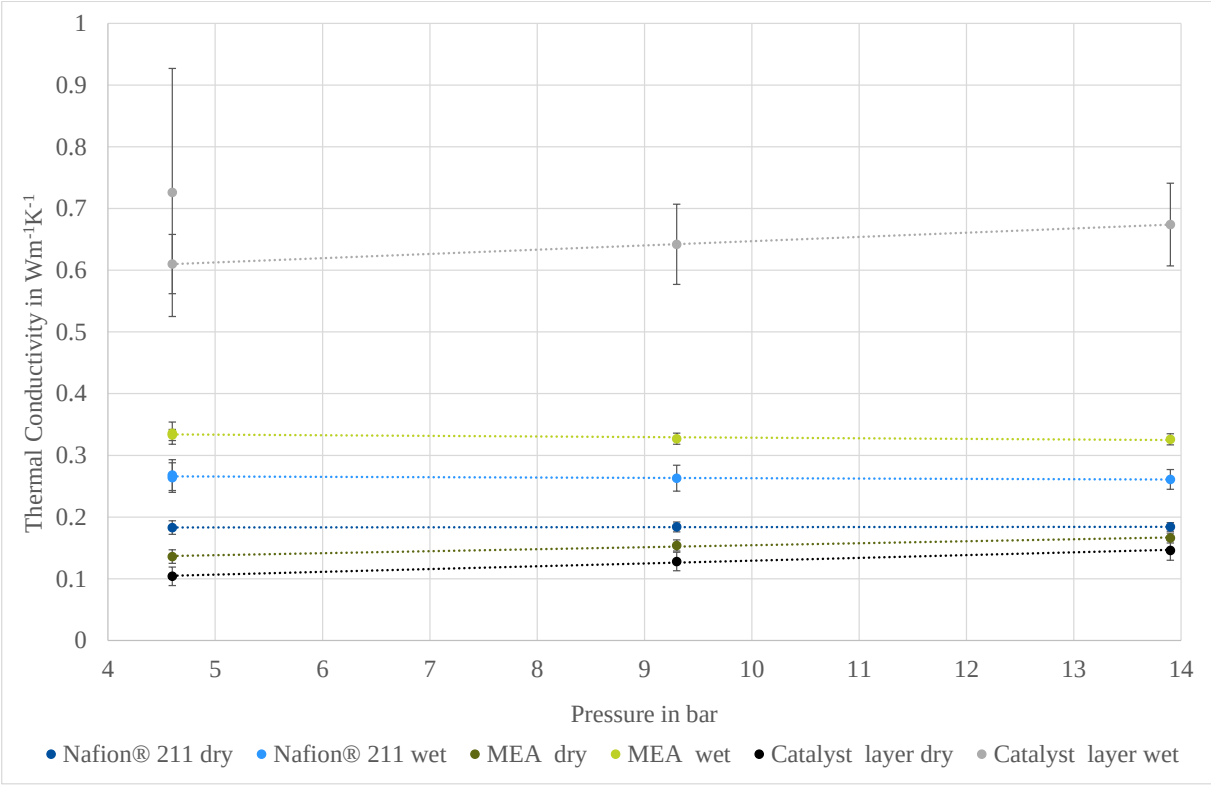

Figure 4.1.: Measured thermal conductivities of FC materials over compaction pressure

than that of dry Nafion®, but was also not notably affected by compaction pressure. With a compression of about $(7 \pm 12)\,\%$ the wet Nafion® seemed to be less compressible than dry Nafion®, but the difference was within the uncertainties of measurement. It showed the same behaviour as dry Nafion® and compressed already at low pressures, with almost no further compression at increasing pressures. The mean water content in the samples was (24 ± 10) wt.% before the measurement and (11 ± 7) wt.% after the measurement. However, the difference in measured thermal conductivity was below the uncertainties of measurement between the first and last measurement at 4.6 bar. The wet samples were on average $(12 \pm 8)\,\%$ thicker than the dry ones, but the values varied a lot from 5 to 21 % between the samples.

The dry MEA showed a pressure dependent thermal conductivity with $(0.14 \pm 0.01)\,\mathrm{W\,m^{-1}\,K^{-1}}$ at 4.6 bar and $(0.17 \pm 0.01)\,\mathrm{W\,m^{-1}\,K^{-1}}$ at 13.9 bar (cf. figure 4.1). The thermal conductivity of the CLs calculated to $(0.10 \pm 0.02)\,\mathrm{W\,m^{-1}\,K^{-1}}$ at 4.6 bar, increasing to $(0.15 \pm 0.02)\,\mathrm{W\,m^{-1}\,K^{-1}}$ at 13.9 bar, and was thus lower than that of Nafion®. The compression of the dry MEA seemed to increase with pressure from $(10 \pm 6)\,\%$ at 4.6 bar to $(15 \pm 6)\,\%$ at 13.9 bar (cf. table 4.2), which was, however, below the uncertainties of measurement. The compressibility of the dry CLs calculated to $(8 \pm 15)\,\%$ at 4.6 bar and $(18 \pm 14)\,\%$ at 13.9 bar. The hysteresis effect was below the uncertainties of measurement.
The wet MEA showed with $(0.33 \pm 0.01)\,\mathrm{W\,m^{-1}\,K^{-1}}$ a significantly higher thermal conductivity than the dry MEA. The impact of pressure on the thermal conductivity was negligible. The CLs showed a thermal conductivity of $(0.61 \pm 0.05)\,\mathrm{W\,m^{-1}\,K^{-1}}$ at 4.6 bar, with an increase under

compaction pressure close to the borders of uncertainty. The last conductivity measurement of wet MEA samples in the hysteresis at 4.6 bar showed high uncertainties of measurement. This led to an outlier in the calculated thermal conductivities of the CLs, as the calculations depend on a high accuracy of the measurement. The outlier was therefore excluded from the trendline calculation of the wet CLs in figure 4.1. As the dry MEA, also the wet MEA showed compressibility under pressure. However, the compressibility could here only be measured under a high level of uncertainty. It compressed by (17 ± 23) % at 4.6 bar compaction pressure and by (19 ± 25) % at 13.9 bar. The hysteresis effect was below the uncertainties of measurement. The compressibility of the CLs was calculated to (16 ± 23) % at 4.6 bar and (25 ± 24) % at 13.9 bar. The water content in the wet MEA was on average (40 ± 3) wt.% before and (17 ± 3) wt.% after the measurements. The average wetting during the measurement was therefore (28.5 ± 0.2) wt.%, or approximately $\lambda = 35 \pm 24$, assuming a uniform distribution of the water in the MEA and (33 ± 10) % Nafion in the CLs (cf. section 3.1.2).

Table 4.2.: Measured compression of FC materials in % at different compaction pressures. Measurement order was from left to right in table

Material	4.6 bar	9.3 bar	13.9 bar	4.6 bar
Nafion® 211 dry	12 ± 10	12 ± 10	12 ± 9	12 ± 9
Nafion® 211 wet	7 ± 13	7 ± 12	7 ± 12	7 ± 12
MEA dry	10 ± 6	13 ± 6	15 ± 6	12 ± 6
MEA wet	17 ± 23	22 ± 23	25 ± 24	19 ± 25
Catalyst layer dry	8 ± 15	15 ± 14	18 ± 14	12 ± 15
Catalyst layer wet	16 ± 23	22 ± 23	25 ± 24	19 ± 25

4.1.3. EC materials

The thermal conductivities for the EC membrane, CL and MEA are depicted in figure 4.2 and listed in Table A.2 for the measurements with single humidification. The results of the measurements with re-humidification are presented at the end of this section. The measured compressions are presented in table 4.3.

The dry Tion5-W PFSA membrane showed a thermal conductivity of $(0.19 \pm 0.01)\,\mathrm{W\,m^{-1}\,K^{-1}}$, with no significant change under variation of pressure. The compression was measured to be (3.5 ± 3.9) % at 4.6 bar without significant increase under higher pressures. The wet thermal conductivity was notably higher. The effect of pressure on the thermal conductivity was below the uncertainties of measurement. At the beginning of the measurements, the wet membrane showed with (0.8 ± 6.4) % a lower compressibility than the dry membrane. At the end of the measurements the compression increased to (2.3 ± 6.3) %, however this effect was within the uncertainties of measurement. The membrane samples contained on average (24 ± 2) wt.% water before and (20 ± 1) wt.% water after the measurements.

The MEA almost doubled its conductivity from $(0.17 \pm 0.01)\,\mathrm{W\,m^{-1}\,K^{-1}}$ to $(0.31 \pm 0.03)\,\mathrm{W\,m^{-1}\,K^{-1}}$

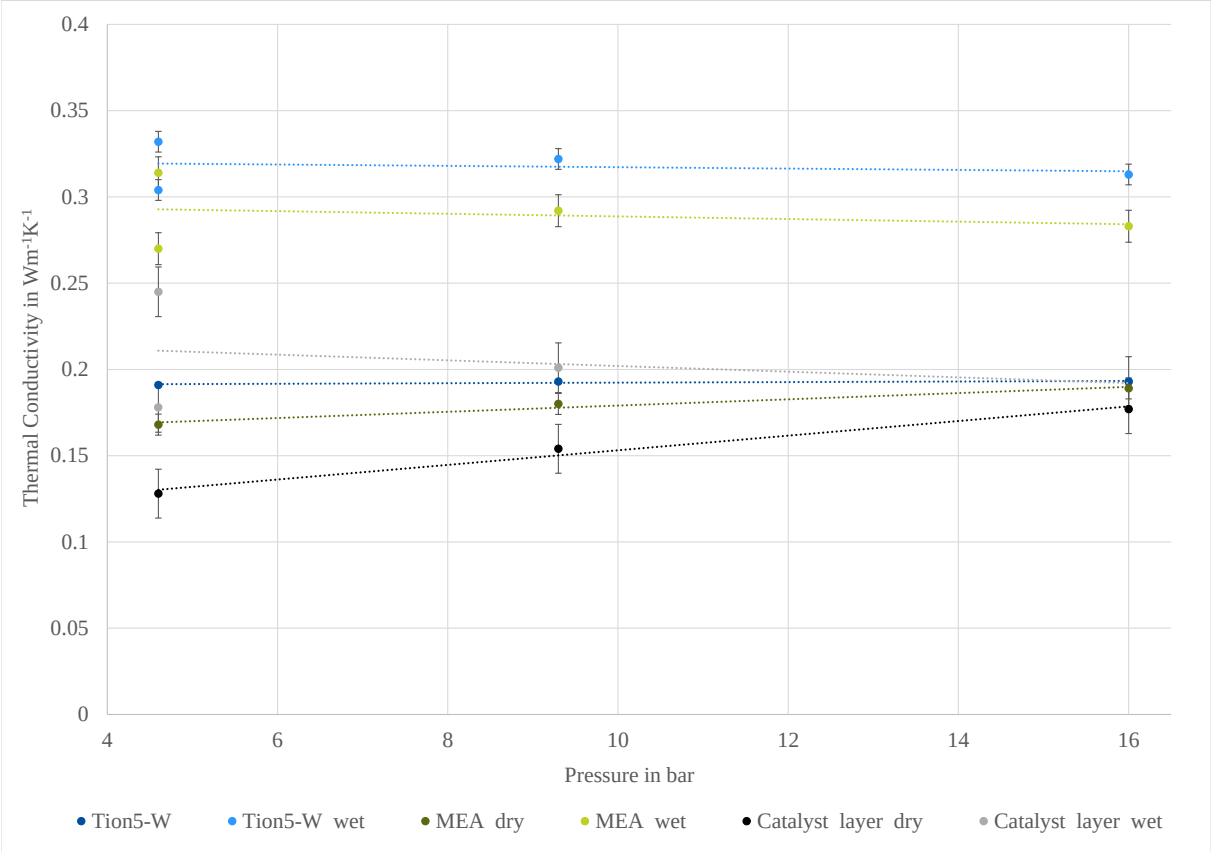

Figure 4.2.: Measured thermal conductivities of EC MEA materials over compaction pressure

at 4.6 bar when being humidified. The wet conductivity decreased with increasing pressure to $(0.28 \pm 0.02)\,\mathrm{W\,m^{-1}\,K^{-1}}$ at 16 bar, which was at the borders of the measurement uncertainty. The dry measurements, though, showed an increase in thermal conductivity by over 10 % to $(0.19 \pm 0.01)\,\mathrm{W\,m^{-1}\,K^{-1}}$ at 16 bar. The dry MEA had a compressibility of (8.6 ± 3.6) % at 4.6 bar, with a slight increase within the uncertainties of measurement under increasing pressure. The wet MEA showed about the same compressibility at 4.6 bar, decreasing within the uncertainties during the measurement, both with increasing and decreasing pressure. The wet MEA samples contained (15 ± 1) wt.% water before and (10 ± 1) wt.% water after the measurements.
The thermal conductivity of the dry CL calculated to $(0.13 \pm 0.01)\,\mathrm{W\,m^{-1}\,K^{-1}}$ at 4.6 bar, increasing to $(0.18 \pm 0.01)\,\mathrm{W\,m^{-1}\,K^{-1}}$ at 16 bar. The thermal conductivity of wet CL was with $(0.25 \pm 0.09)\,\mathrm{W\,m^{-1}\,K^{-1}}$ during the first measurement significantly higher. A decreasing conductivity could be noted under increasing pressure, with a conductivity of $(0.19 \pm 0.02)\,\mathrm{W\,m^{-1}\,K^{-1}}$ at 16 bar. The dry CL showed significant compressibility, with (19 ± 11) % compression at 4.6 bar and (31 ± 9) % at 16 bar. The compression of the wet CL could not be evaluated to meaningful results due to the high uncertainties of measurement. The hysteresis effect was within the uncertainties of measurement for both the dry and wet CL. The humidification level of the CL was not calculated, as only speculations can be made on the distribution of water between the membrane and CL because of unknown material-properties of both the Tion5 membrane and the EC CL used in the MEA.

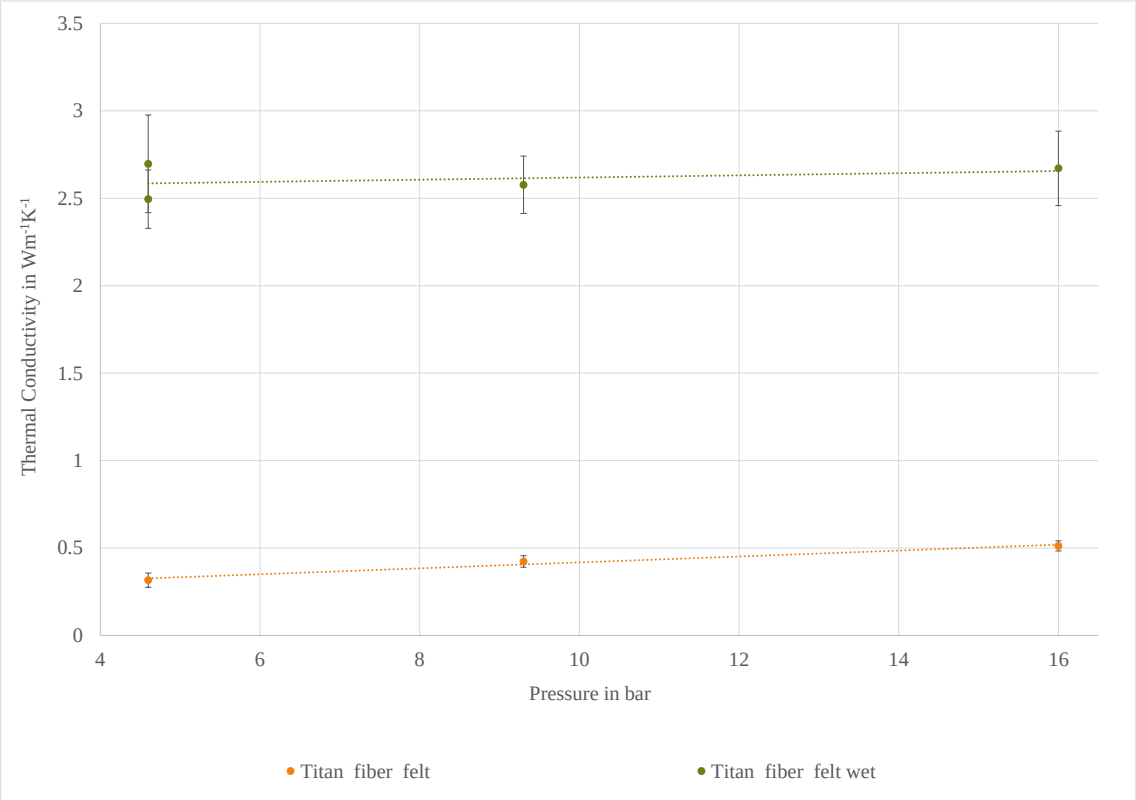

Figure 4.3.: Measured thermal conductivity EC platinum felt PTL over compaction pressure

The thermal conductivities of the platinized titanium felt PTL measured with single humidification of each sample are plotted over the compaction pressure in figure 4.3 and are listed in Table A.2. The dry PTL showed increasing thermal conductivity under pressure with $(0.32 \pm 0.04)\,\mathrm{W\,m^{-1}\,K^{-1}}$ at 4.6 bar and $(0.51 \pm 0.03)\,\mathrm{W\,m^{-1}\,K^{-1}}$ at 16 bar, while being only slightly compressible (cf. table 4.3). The wet PTL showed a significantly higher thermal conductivity with $(2.50 \pm 0.17)\,\mathrm{W\,m^{-1}\,K^{-1}}$ at 4.6 bar and $(2.67 \pm 0.21)\,\mathrm{W\,m^{-1}\,K^{-1}}$ at 16 bar. The wet PTL did not show significant compressibility either. The water content in the PTL samples was (25 ± 1) wt.% before the measurements and (11 ± 8) wt.% after the measurements. Using the weight of the water in the samples before the measurements with an average of (45 ± 3) mg per sample, their thickness of (250 ± 2) µm and diameter of (21 ± 1) mm, the samples were calculated to have an average porosity of (52 ± 5) %.

All wet thermal conductivity measurements showed significant hysteresis effects between the first and the second measurement at 4.6 bar. This must be attributed to dryout as the samples had been precompressed during the dry measurements. To determine if the dryout of the samples had to be attributed to the compression or to time-dependent dryout (cf. section 3.1.2), they were measured again with re-humidifying the samples between each pressure step.
In table 4.4 the humidification levels of these measurements are compared to the humidification levels of the measurements described above. The deviation between the measurements with- and without re-humidification was within the uncertainties of measurement for both the humidification

level and the thermal conductivities. The thermal conductivities measured with re-humidification are here therefore not separately discussed, but listed in the appendix in table A.3.

Table 4.3.: Measured compression of EC materials in % at different compaction pressures. Measurement order was from left to right in table

Material	4.6 bar	9.3 bar	16.0 bar	4.6 bar
Tion5-W	3.3 ± 3.0	3.6 ± 3.1	3.5 ± 3.9	3.2 ± 3.0
Tion5-W wet	0.8 ± 6.4	1.7 ± 6.3	2.4 ± 6.3	2.3 ± 6.3
MEA dry	8.6 ± 3.6	11.1 ± 3.3	12.8 ± 3.3	10.3 ± 4.3
MEA wet	8.3 ± 4.4	5.1 ± 4.4	6.5 ± 4.3	4.8 ± 4.4
Catalyst layer dry	19.0 ± 10.5	25.6 ± 9.3	30.8 ± 8.7	24.2 ± 9.6
Catalyst layer wet	13.4 ± 26.5	16.5 ± 25.5	19.8 ± 24.3	12.7 ± 26.5
Titan fibre felt	0.7 ± 0.7	1.2 ± 0.5	1.4 ± 0.6	1.1 ± 0.7
Titan fibre felt wet	1.7 ± 4.8	1.6 ± 5.0	1.8 ± 4.6	1.5 ± 4.1

Table 4.4.: Mean humidification level during the thermal conductivity measurements in wt.% measuring all pressures at once compared to re-humidifying the sample before changing the pressure

Material	**Once humidified**	**Re-humidified**
Tion5-W wet	22 ± 1	22 ± 2
MEA wet	13 ± 1	12 ± 1
Titan fibre felt	18 ± 4	20 ± 3

4.2. Simulated temperature distribution

After measuring the thermal conductivities within the different layers in the EC, the temperature distribution was modelled for a PEM electrolysis stack. In the following firstly, the results of the validation of the model are presented. Afterwards, the simulated temperature distribution within the stack is presented under different operating conditions.

4.2.1. Validation

In the following, the results of general tests as mesh refinement study and variation of thermal conductivities are presented first. Afterwards, the model is compared to literature on a cell level and lastly on a stack level.

Doubling the number of cells in y-direction did not have a notable impact on the results of the simulation, as shown in figure 4.4a and 4.4b on for the middle cell in the stack (EC no. 21). The results on a stack level are for further reference depicted in the appendix in figure A.1a and A.1b.

21 mesh-cells in z-direction are thus proven to be sufficient to model the relevant temperature gradients of this study.

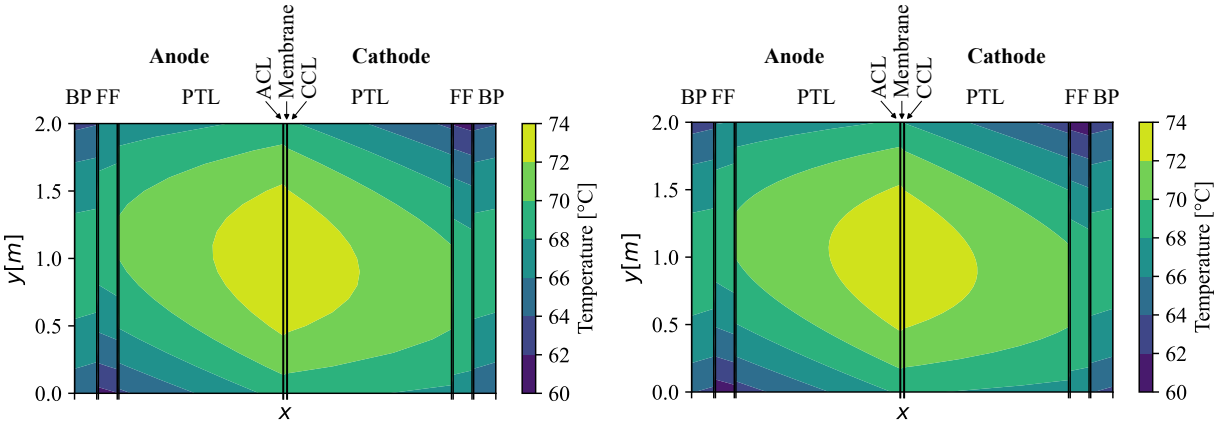

(a) $N_{\text{mesh-cells,y}} = 21$ **(b)** $N_{\text{mesh-cells,y}} = 42$

Figure 4.4.: Results mesh refinement study for middle cell in stack with counter-flow

The simulated temperature gradients using uniformly high/low conductivities are depicted in figure 4.5a and 4.5b on a cell level and for further reference in the appendix in figure A.2a and A.2b on a stack-level. As expected, high temperature gradients occurred in x-direction with low conductive layers, whereas temperature gradients along the channels of the FFs in y-direction prevailed when highly conductive materials were considered in the cells. The maximal temperature gradient over the cell was with about 10 K significantly lower when high conductivities were used in the simulation compared to 24 K using low conductivities. This indicates a correct implementation in principle.

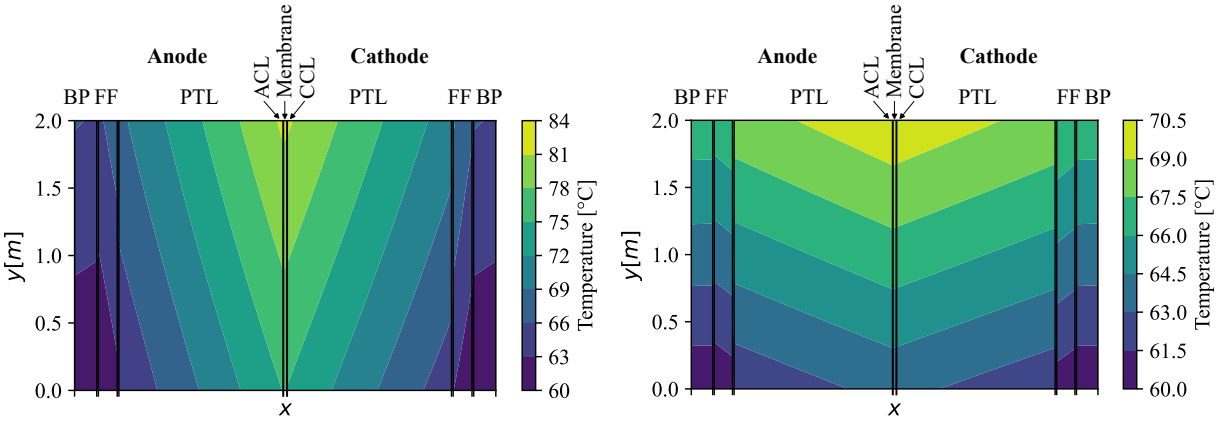

(a) Low conductivity: $2\,\mathrm{W\,m^{-1}\,K^{-1}}$ **(b)** High conductivity: $15\,\mathrm{W\,m^{-1}\,K^{-1}}$

Figure 4.5.: Results for high and low conductivities for middle cell in stack with parallel flow

The simulation was then first validated for the temperature distribution within a single EC. The results generated using the model of this study and the parameters from Bock *et al.* [7] are depicted in figure 4.6 and are compared to the results of Bock *et al.*'s model (figure 4.7). Both simulations used the V-i-characteristic described by Bock *et al.* at a current density of $3\,\mathrm{A\,cm^{-2}}$. The temperatures at the outer side of the FFs were 2 K higher in the results of Bock *et*

al. than predicted here. The increase in temperature in the FFs including their BLs was similar in both simulations. Each of the simulations also showed a significantly higher temperature in the ACL than in the CCL with the highest temperature at the ACL-membrane interface. The temperature gradients over the anodic PTL and ACL were similar, with about 4 K for the least conducting material (Sinter 3 with 5.6 $\mathrm{W\,m^{-1}\,K^{-1}}$), about 3.5 K for Sinter 2 (6.9 $\mathrm{W\,m^{-1}\,K^{-1}}$) and about 2.8 K for the most conductive PTL (Sinter 1 with 8.2 $\mathrm{W\,m^{-1}\,K^{-1}}$). On the cathode side, however, the temperature gradients only agreed for the high conductive PTLs but were slightly lower for the Sinter 3 using this study's model. Also, the maximal temperatures were with 87.4 °C using Sinter 1 and 88.5 °C using Sinter 3 slightly lower and had a smaller deviation between the different PTLs than the values measured by Bock *et al.* with 92.0 °C using Sinter 3 and 89.1 °C using Sinter 1. On the right side of the anodic FF BL, the PTL with the highest conductivity had a higher temperature than the PTLs with lower conductivities, which was not the case in the results of Bock *et al.*

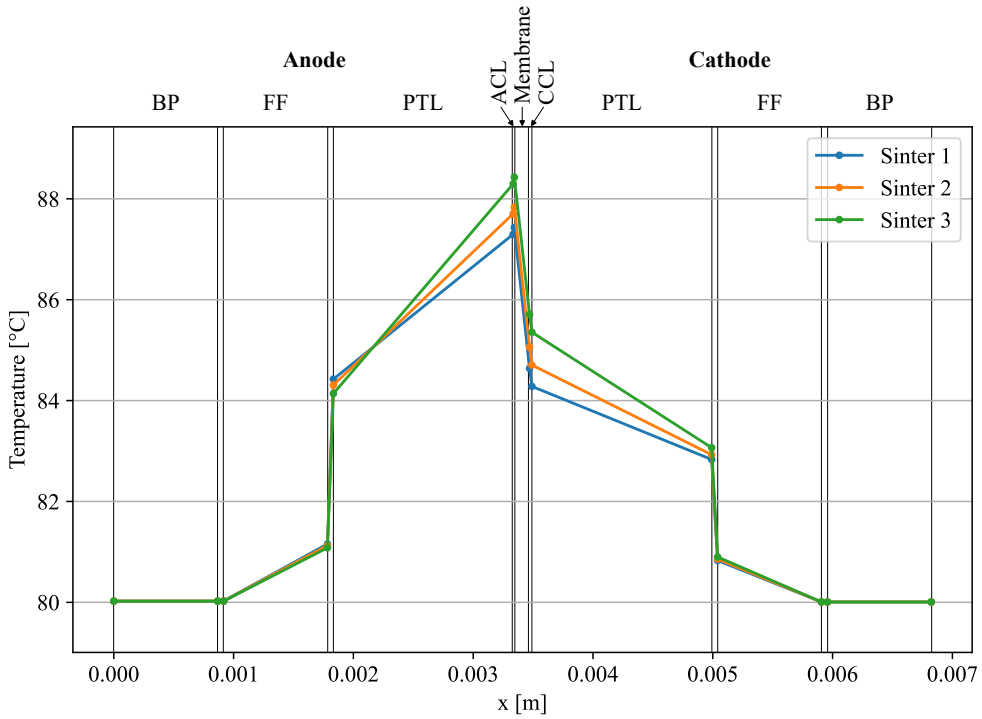

Figure 4.6.: Simulated temperatures within a single EC with $i = 3\,\mathrm{A\,cm^{-2}}$

Bock *et al.* assumed higher overpotentials and thus a steeper V-i-characteristic than Krenz *et al.* [5]. Both V-i characteristics are compared in figure 4.8. The model was solved a second time at $i = 3\,\mathrm{A\,cm^{-2}}$ using the overpotentials described by Krenz *et al.*, which were used in the course of this study (cf. section 3.2.1). The results are illustrated in figure 4.9. The shape of the temperature distribution was the same as before, but the temperatures were overall lower, with a maximal temperature of about 85.7 °C at the anode side of the membrane with a Sinter 3 PTL and about 85 °C using Sinter 1.

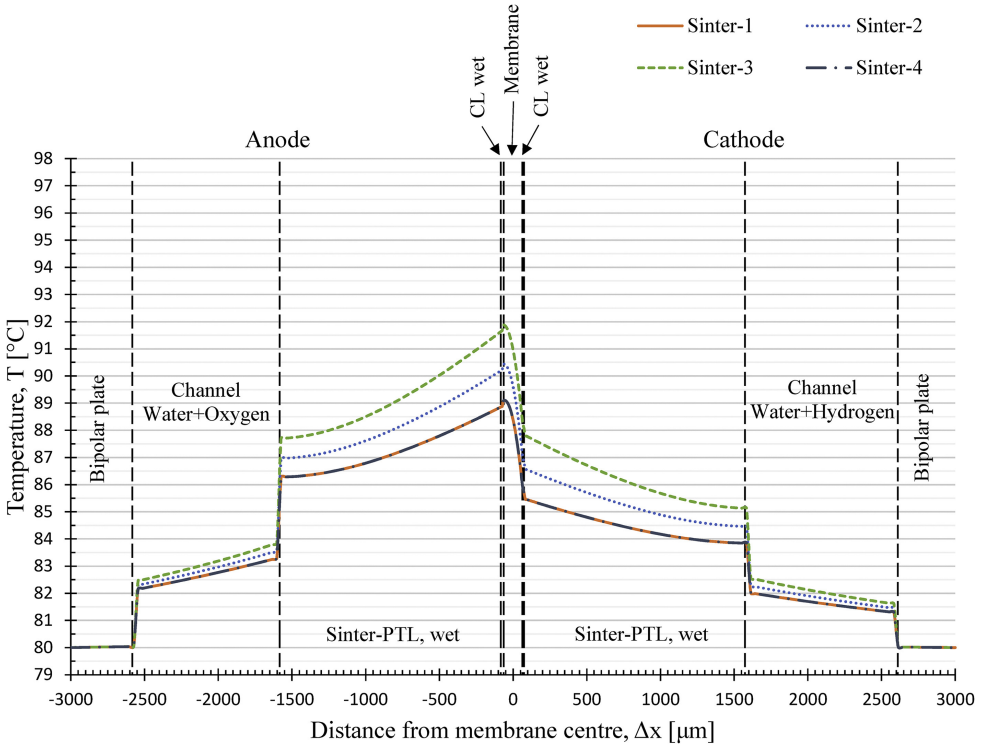

Figure 4.7.: Temperatures within a single EC with $i = 3\,\mathrm{A\,cm^{-2}}$ from Bock *et al.* [7]

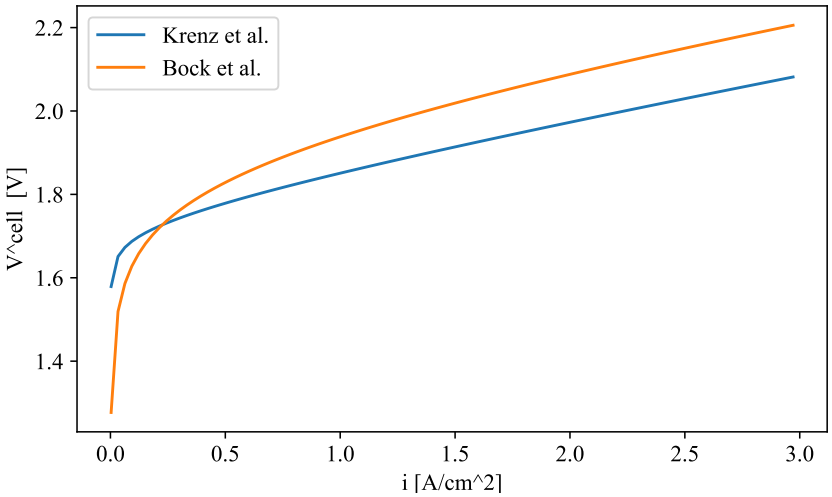

Figure 4.8.: Comparison V-i characteristics Bock *et al.* and Krenz *et al.*

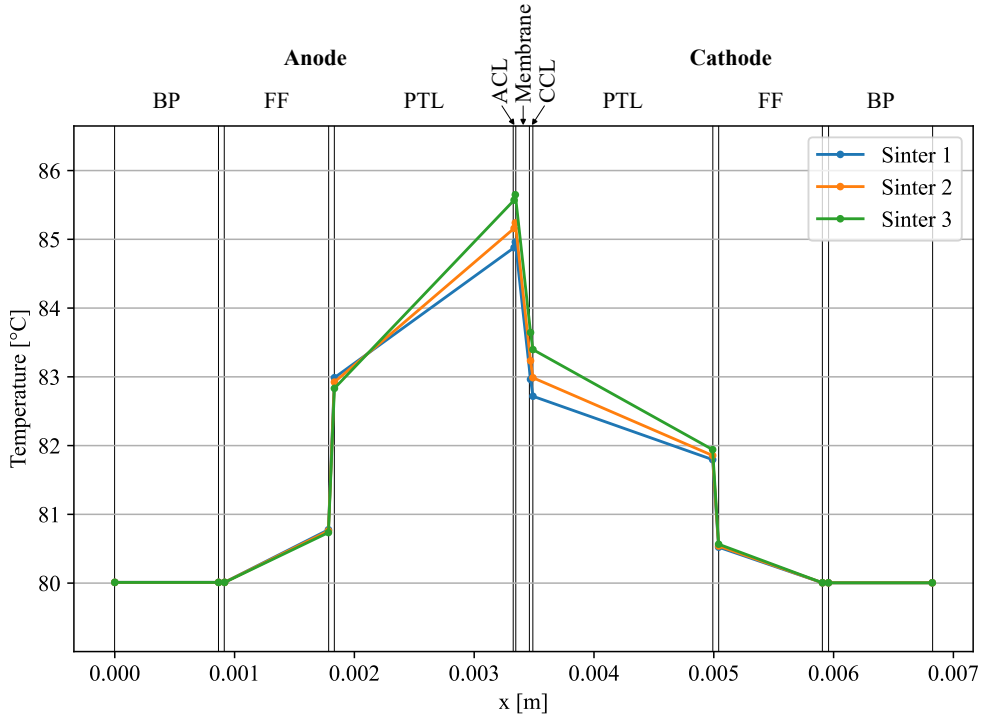

Figure 4.9.: Simulated temperature-gradients using parameters from Bock *et al.* and overpotentials from Krenz *et al.*

Secondly, the simulation was validated for a PEMEC stack at a mean current density of $2\,\mathrm{A\,cm^{-2}}$ using parameters from Krenz *et al.* [5]. The simulated temperature distribution over a stack in parallel flow is depicted in figure 4.10. The temperatures at the side of the FF inlets were predicted to lie between 60 °C in the FFs and 65 °C in the membranes. At the outlet side, the temperatures reached a maximum with about 67 °C in the FFs and 71 °C in the membranes. The temperatures in the outer cells of the stack were, with a decrease of 1.4 K in maximal temperature on the left side and 1.1 K on the right side, slightly lower than in the middle cells. This corresponds well with the distribution of the mean temperatures in the ECs predicted by Krenz *et al.* (figure 4.11a).

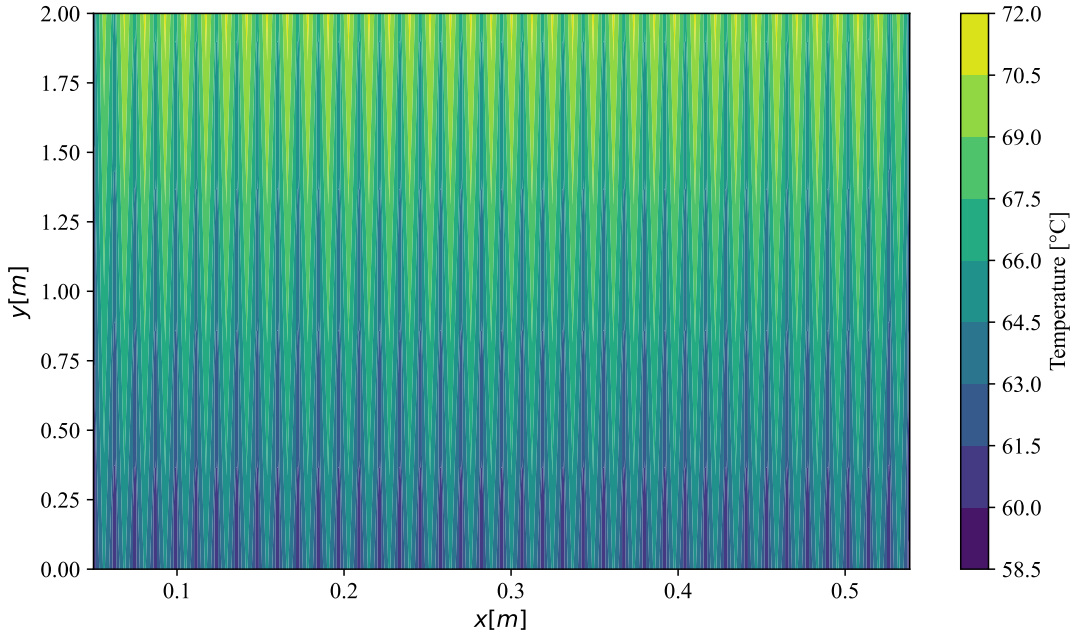

Figure 4.10.: Simulated temperatures within a 40 cell EC stack at $\bar{i} = 2\,\mathrm{A\,cm^{-2}}$ in parallel flow

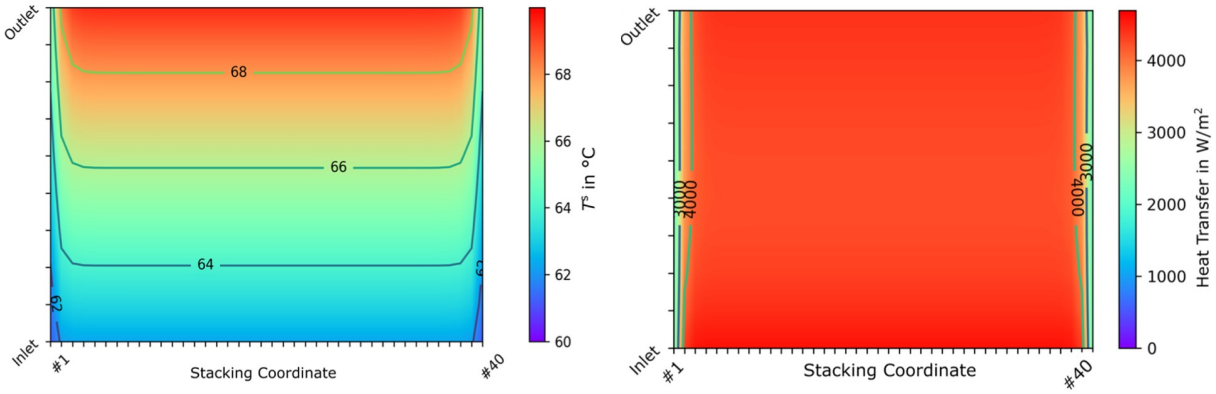

(a) Temperature **(b)** Heat flux to anodic fluid

Figure 4.11.: 40 cell EC stack at $\bar{i} = 2\,\mathrm{A\,cm^{-2}}$ under parallel flow as simulated by Krenz *et al.* (images from [5])

The simulated heat flux in x-direction in a cross-section through the stack in the middle of ECs ($y = 1\,\mathrm{m}$) is presented in figure 4.12 to compare the heat flux into the anodic fluid with the predictions of Krenz *et al.* (figure 4.11b). Positive values indicate a heat flux towards the cathode side, negative values to the anode side. The heat flux at the inner (right) BL of the anodic FF is represented by the point left of the most negative heat flux in each EC and was at about $-4200\,\mathrm{W\,m^{-2}}$ in the middle of the stack. The heat flux at the interface to the outer (left) BL of the anodic FF (next visible point to the left) was predicted to be close to zero for all ECs but the first. The value of the heat flux at the inner BL of the anodic FF thus represented the heat flux into the anodic fluid. In the first EC on the left a significant heat flux was leaving the anodic FF towards the BP on the left so that the heat flux absorbed by the anodic fluid was

here lower with about 3200 W m^{-2}. Also the heat flux into the anodic fluid in the last cell of the stack (right side) was lower than in the middle of the stack. This corresponds well with the findings of Krenz *et al.*

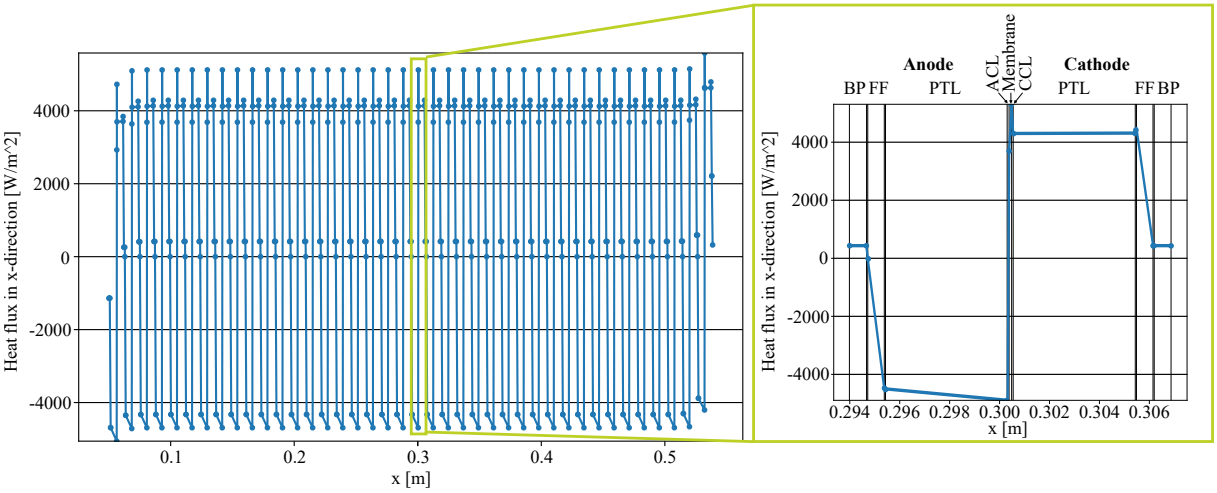

Figure 4.12.: Simulated heat flux within a 40 cell EC stack at $y = 1$ m at $\bar{i} = 2$ A cm^{-2} with parallel flow. Right: Magnified view of single cell in stack

As a last validation step, the simulated temperatures were compared to the results of Krenz *et al.* for a EC stack in counter-flow at a mean current density of 2 A cm^{-2}. The maximal simulated temperatures occurred here close to the centre of the cells at $y = 1$ m with about 73.5 °C in the membranes and about 69 °C in the FFs (figure 4.13) and were thus higher than the maximal temperatures in parallel flow. The temperature in the outer ECs was with a decrease in maximal temperature of 3.4 K on the left side and 2.6 K on the right side slightly more affected than in parallel flow. These results correspond well with the findings of Krenz *et al.* (figure 4.14).

The predicted conditions thus correspond in general quite well to the predictions in literature. Differences between predictions of the model and literature are further discussed in section 5.2.1.

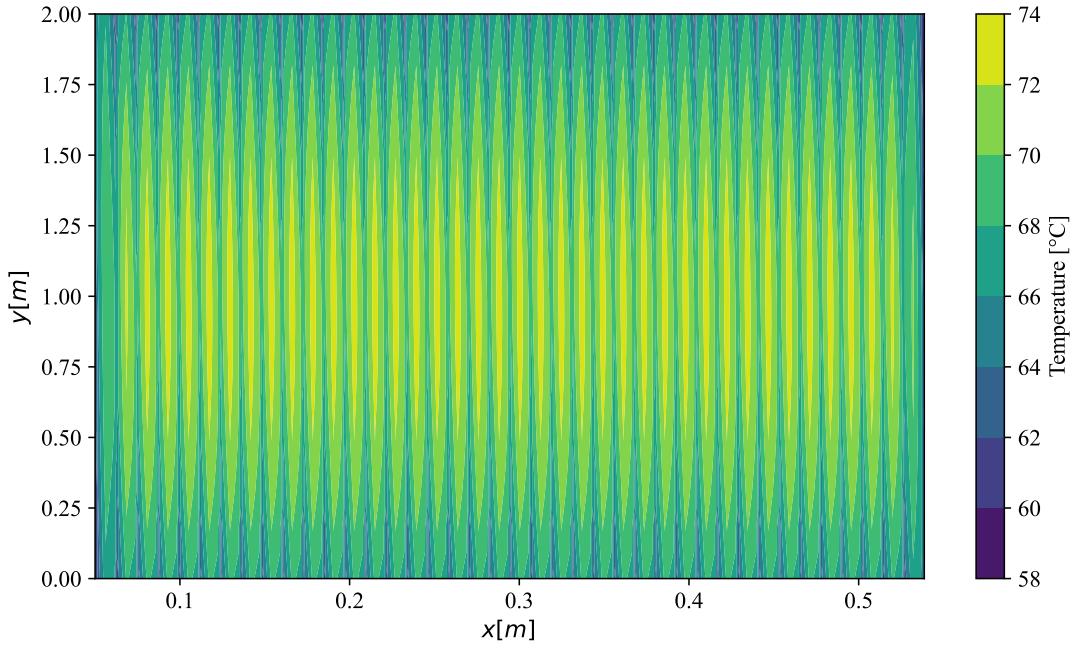

Figure 4.13.: Simulated temperatures within a 40 cell EC stack at $\bar{i} = 2\,\mathrm{A\,cm^{-2}}$ at counter-flow

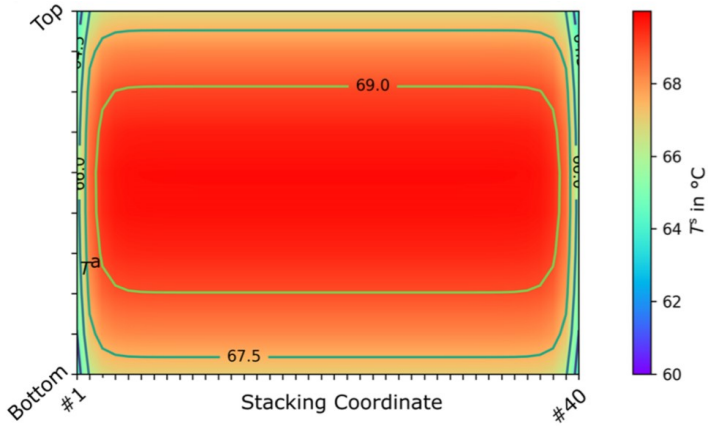

Figure 4.14.: Temperatures in a 40 cell EC stack at $\bar{i} = 2\,\mathrm{A\,cm^{-2}}$ under counter-flow as simulated by Krenz *et al.* (image from[5])

4.2.2. Simulated scenarios

In the following, the simulated temperature distributions under the different scenarios described in section 3.2.3 are presented. Table 4.5 summarizes the voltage efficiencies under parallel and counter-flow conditions. Table 4.6 summarizes the maximal temperature gradients that occur within a single cell in the stack. Efficiencies and gradients of the scenario "Without water drag" are not included in the table as this scenario does not investigate an actual operating scenario but the influence of an effect that always occurs during operation. The detailed temperature distributions within the stack and cells are presented in more detail within the next sections.

Table 4.5.: Voltage efficiency

Simulated scenario	Parallel flow	Counter-flow
Max. measured conductivities	75.03 %	75.20 %
Min. measured conductivities	75.12 %	75.31 %
Sinter PTL	74.72 %	74.97 %
High current density	71.40 %	71.65 %
Warmer cathode	75.03 %	75.20 %

Table 4.6.: Maximal temperature gradient within a single cell in the stack

Simulated scenario	Parallel flow	Counter-flow
Max. measured conductivities	15.95 K	17.08 K
Min. measured conductivities	17.12 K	18.07 K
Sinter PTL	12.07 K	13.61 K
High current density	26.13 K	27.02 K
Warmer cathode	18.98 K	20.45 K

Maximal measured conductivities parallel flow (base scenario)

Using the thermal conductivities at the upper boundary of uncertainty of the values measured in this study for PTL, CL and membrane yielded a maximal temperature gradient of 16.0 K within a single cell under parallel flow conditions. The temperature distribution within the middle cell of the stack is depicted in figure 4.15. The highest temperature was reached between the ACL and membrane at the side of the outlets of the FFs with 76.0 °C. The temperature in the anodic half-cell was always slightly higher than in the cathodic half-cell, but otherwise similarly distributed. Within the stack, a similar temperature distribution was predicted for all cells in the middle of the stack (figure 4.16). Only the first and last cell adjoining to the end-plates were notably colder, with a maximal temperature of 74.0 °C in the first and 75.1 °C in the last cell.

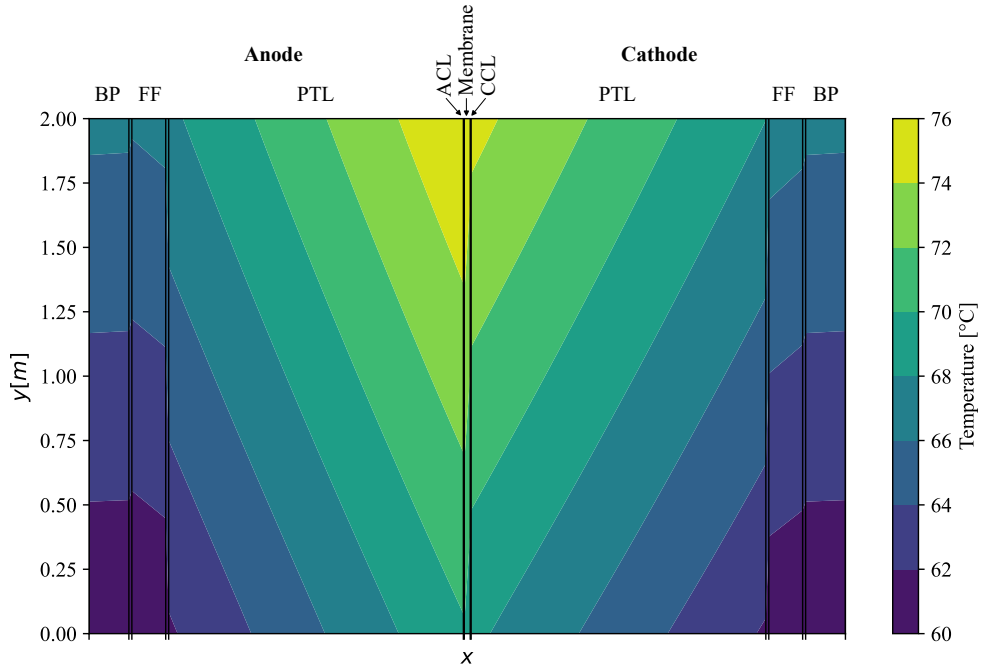

Figure 4.15.: Simulated temperature distribution in middle cell (no. 20) under parallel flow using maximal values of measured conductivities

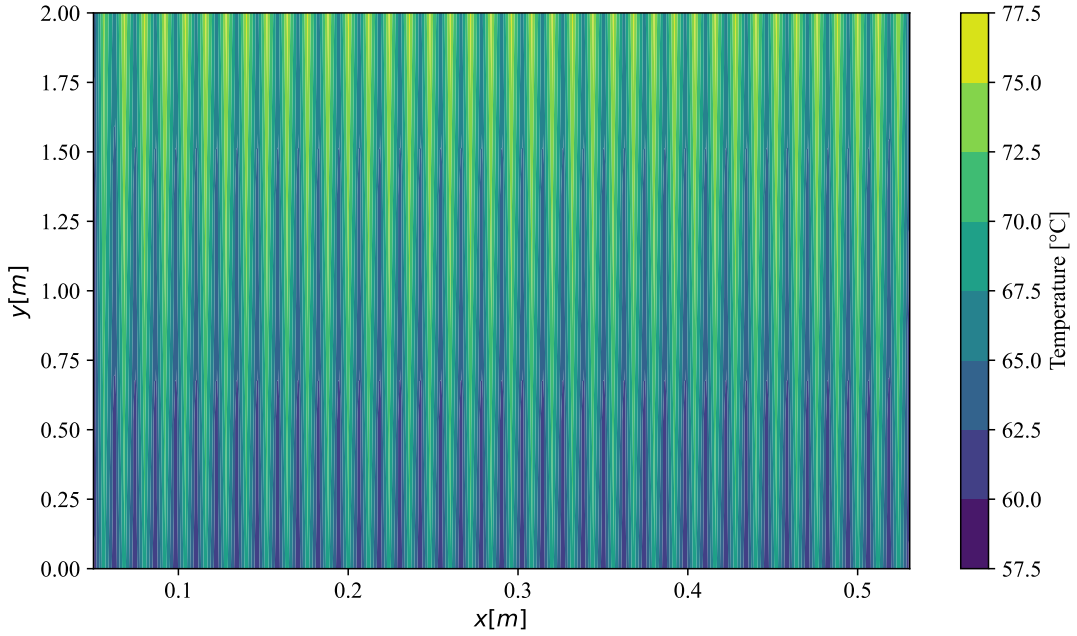

Figure 4.16.: Simulated temperature distribution in stack under parallel flow using maximal values of measured conductivities

Maximal measured conductivities counter-flow (base scenario)

Assuming the same thermal conductivities under counter-flow conditions, the maximal temperature gradient within the ECs increased by 1.1 K to 17.1 K. The temperature distribution within the middle cell of the stack is depicted in figure 4.17. The maximal temperature occurred here

between the ACL and membrane slightly above the centre of the cell in y-direction with 77.1 °C. In the cathodic half-cell, the maximal temperatures were reached slightly below the middle of the cell and thus closer to the outlet of the respective half-cell.

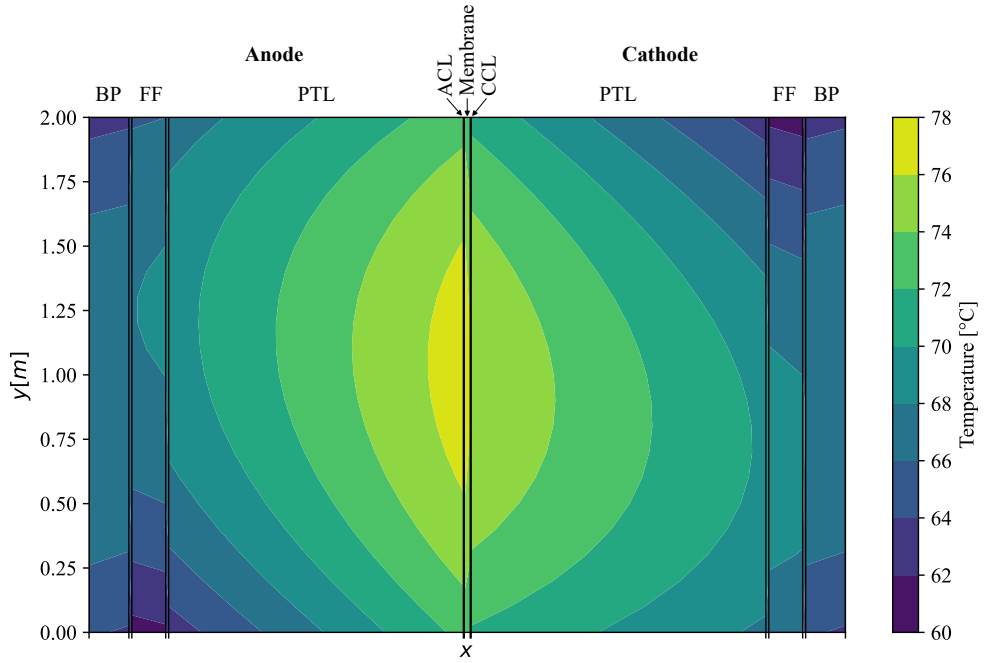

Figure 4.17.: Simulated temperature distribution in middle cell (no. 20) under counter-flow using maximal values of measured conductivities

Compared to parallel flow, the current density was more uniformly distributed across the cell in y-direction with a lower maximal and higher minimal value, while the mean current density was $2\,\mathrm{A\,cm^{-2}}$ in both cases (cf. figure 4.18). Also, a slightly higher voltage efficiency was reached under counter-flow conditions with 75.2 % compared to 75.0 % under parallel flow. Because of the higher efficiency, this flow-arrangement was considered more relevant and is presented in more detail in the following scenarios.

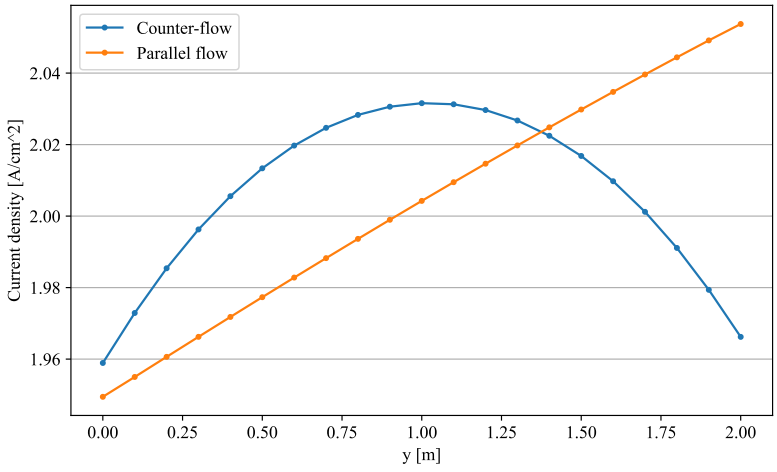

Figure 4.18.: Comparison of simulated current densities along the y-axis in the middle cell under counter- and parallel flow conditions using maximal measured conductivities

The temperature gradients on a stack level are depicted in figure 4.19. The temperature distribution was similar in all cells in the middle of the stack. Only the outer cells of the stack were significantly colder. As shown in figure 4.20a, the temperature within the first cell on the left side of the stack was more uniformly distributed between the anodic and cathodic side inside the MEA than in the middle cells. However, the thermal gradient in the anodic half-cell increased. The maximal temperature was with 73.4 °C about 4 K lower than in the cells in the middle of the stack. In the last cell on the right side of the stack, the temperature gradient between anodic- and cathodic side of the MEA was higher than in the middle cells (figure 4.20b). The temperature decreased here more significantly in the cathodic half-cell. The maximal cell temperature lies with about 75.0 °C between the temperature in the first cell and the temperature in the middle of the stack.

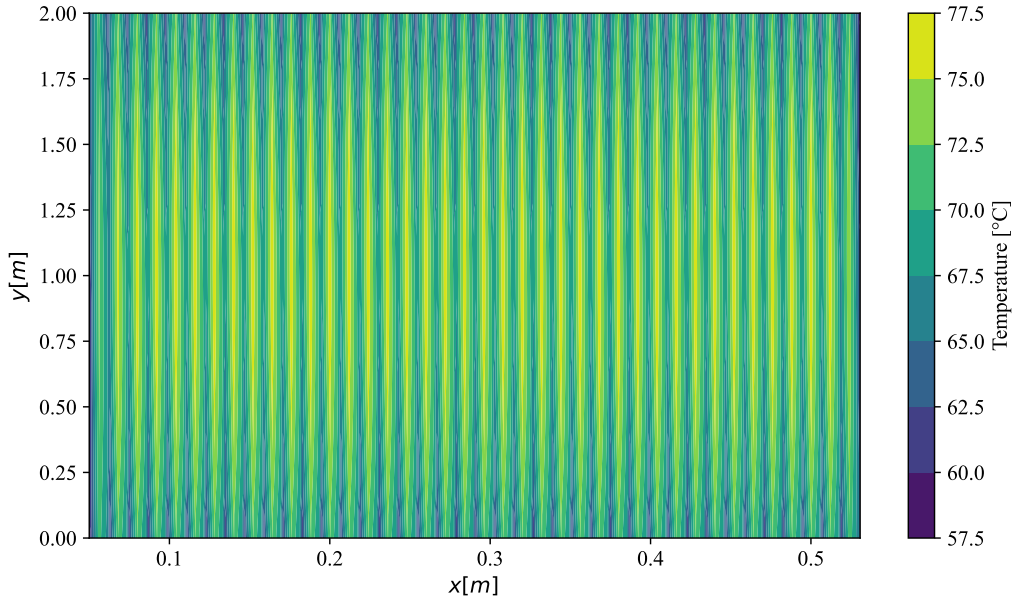

Figure 4.19.: Simulated temperature distribution in stack under counter-flow using maximal values of measured conductivities

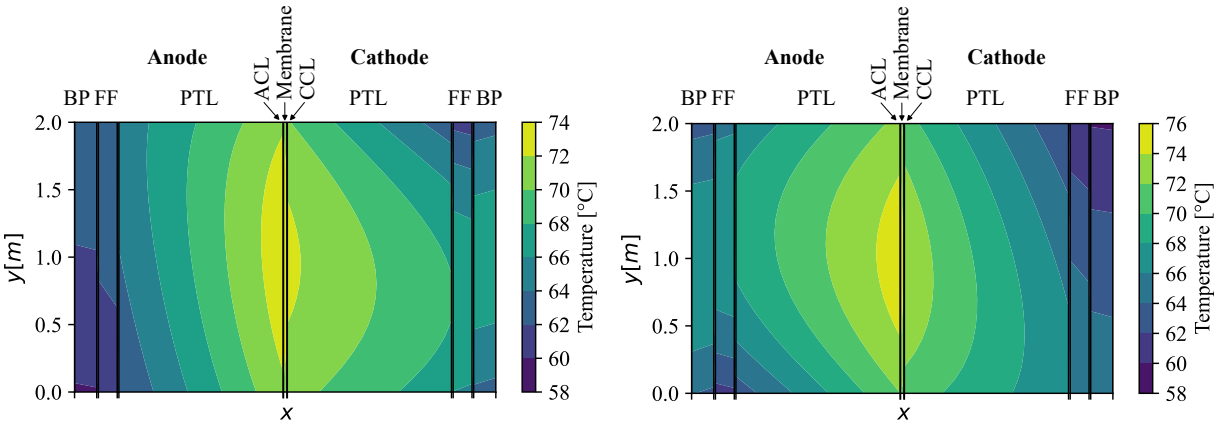

(a) First cell (no. 0) **(b)** Last cell (no. 39)

Figure 4.20.: Simulated temperature distribution in first and last cell under counter-flow using maximal values of measured conductivities

Minimal measured conductivities counter-flow

The thermal conductivities at the lower uncertainty boundary of the values measured in this study for the PTL, CLs and membrane were then used for a simulation in counter-flow. The shape of the derived temperature distribution within the cells was similar to the one calculated using the maximal conductivities (figure 4.21). However, the maximal temperature was with 78.1 °C in the middle of the cell, 1 K higher than using maximal conductivities. Thus, the maximal temperature gradient within the cell increased to 18.1 K, leading to an increase by 0.11 % in voltage efficiency. The temperature distribution over the stack is presented in figure 4.22 in form of the maximal temperatures in each cell in both and compared to the case with maximal measured conductivities. The general shape of the temperature distribution is the same, but the temperatures are overall higher when minimal conductivity values were used.

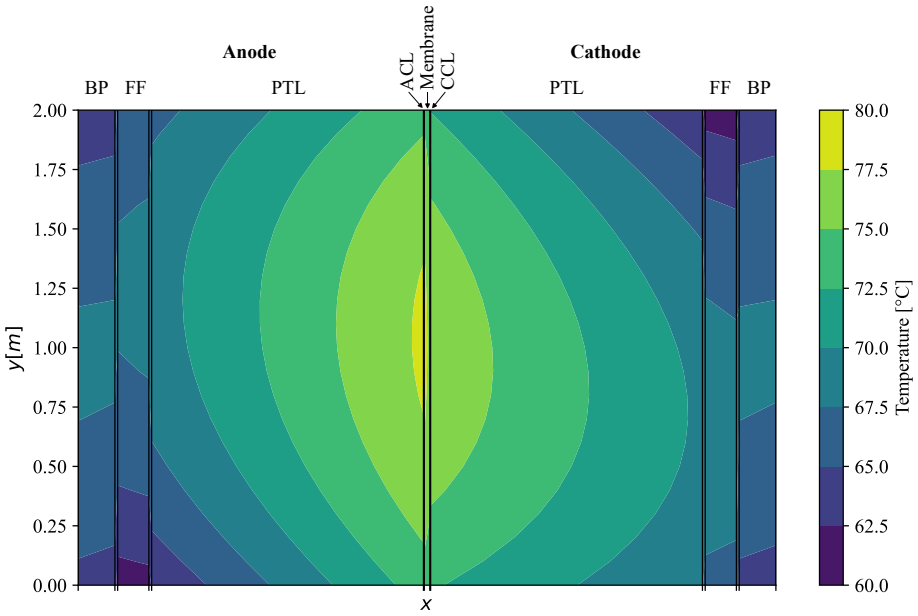

Figure 4.21.: Simulated temperature distribution in middle cell (no. 20) under counter-flow using minimal values of measured conductivities

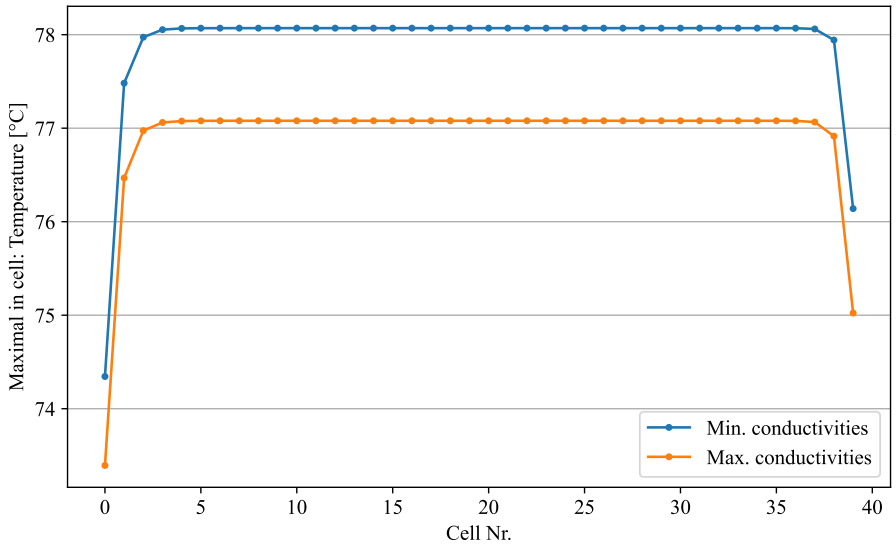

Figure 4.22.: Maximal temperatures in each cell of the stack under counter-flow using minimal and maximal values of measured conductivities

Minimal measured conductivities parallel flow

The same parameters were applied to a stack in parallel flow. The maximal temperature predicted in the cells increased by 1.1 K and reached 77.1 °C, and thus a maximal temperature gradient within a single cell of 17.1 K. The efficiency increased by 0.09 %. The general shape of the temperature distribution did not change notably compared to using maximal conductivities, as presented in figure 4.23. Also the temperature-distribution on a stack-level was predicted to be similar in both scenarios, however, with overall higher maximal temperatures when using the lower conductivity values (figure 4.24).

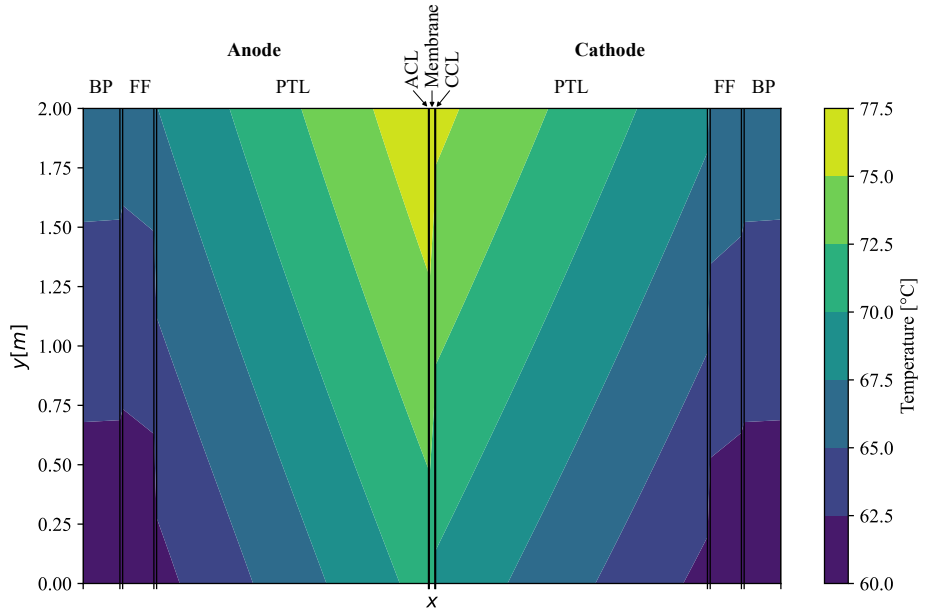

Figure 4.23.: Simulated temperature distribution in middle cell (no. 20) under parallel flow using minimal values of measured conductivities

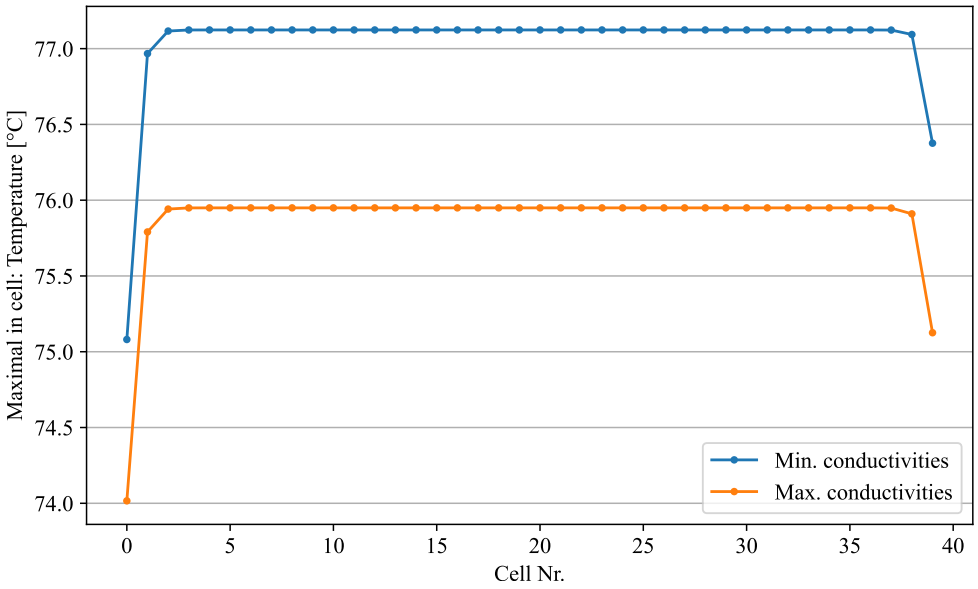

Figure 4.24.: Maximal temperatures in each cell of the stack under parallel flow using minimal and maximal values of measured conductivities

Sinter PTL

Another simulation was conducted using maximal measured conductivity values for membrane and CLs, but literature values of sintered titanium PTL for the PTL-layers. The simulated temperature distribution within the middle cell of the stack is depicted in figure 4.25 for the counter-flow case. The maximal temperature in the cell was with 73.6 °C about 3.5 K lower than in the base-scenario, with a maximal thermal gradient of 13.6 K within a single cell. Also the voltage efficiency was with a decrease of 0.2 % slightly lower than in the base scenario. The temperature gradient decreased especially in x-direction and much less in y-direction, which altered the shape of the thermal gradients compared to the base scenario. The temperature-distribution over the stack was similar to the base scenario, however, shifted to lower temperatures and with a slightly higher cooling effect on the outer cells on the right side (cf. figure 4.26).

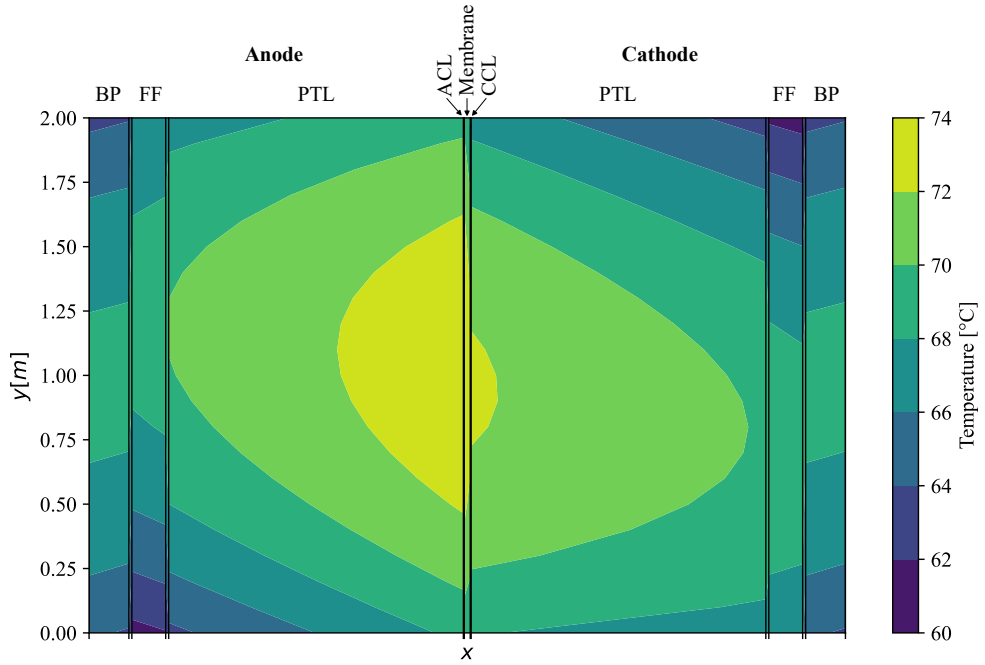

Figure 4.25.: Simulated temperature distribution in middle cell (no. 20) under counter-flow using sintered PTLs

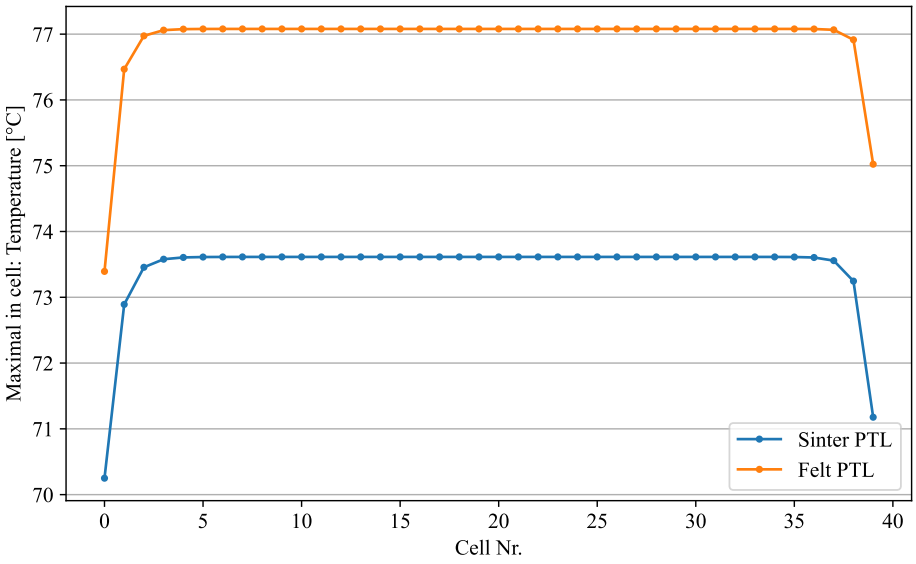

Figure 4.26.: Maximal temperatures in each cell of the stack under counter-flow with sinter PTLs compared to the base case

Using the thermal conductivities of sinter PTL in a stack under parallel flow had a similar impact. The maximal temperature decreased about 3.8 K to 72.1 °C compared to the base scenario, giving a maximal temperature gradient of 12.1 K within the cells. The voltage efficiency decreased with 0.3 % slightly more than in counter-flow. As pictured in figure 4.27, the temperature gradient decreased also in parallel flow especially in x-direction, leading to flatter isotherms. Also the impact on the temperature distribution over the stack was similar to the counter-flow case, with a higher cooling effect on the right side of the stack compared to the base scenario (figure 4.28).

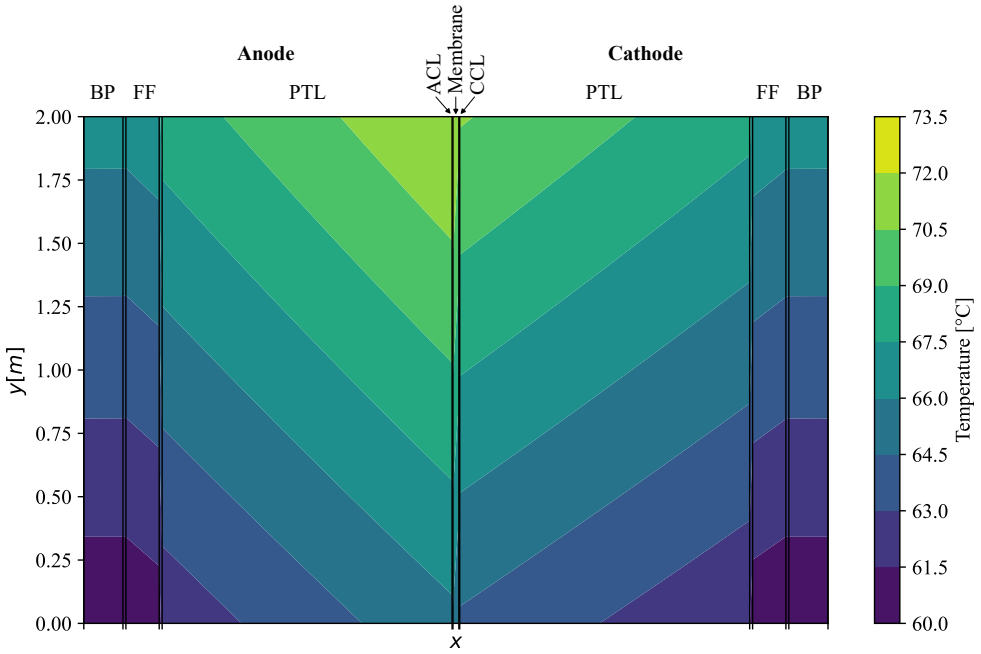

Figure 4.27.: Simulated temperature distribution in middle cell (no. 20) under parallel flow using sintered PTLs

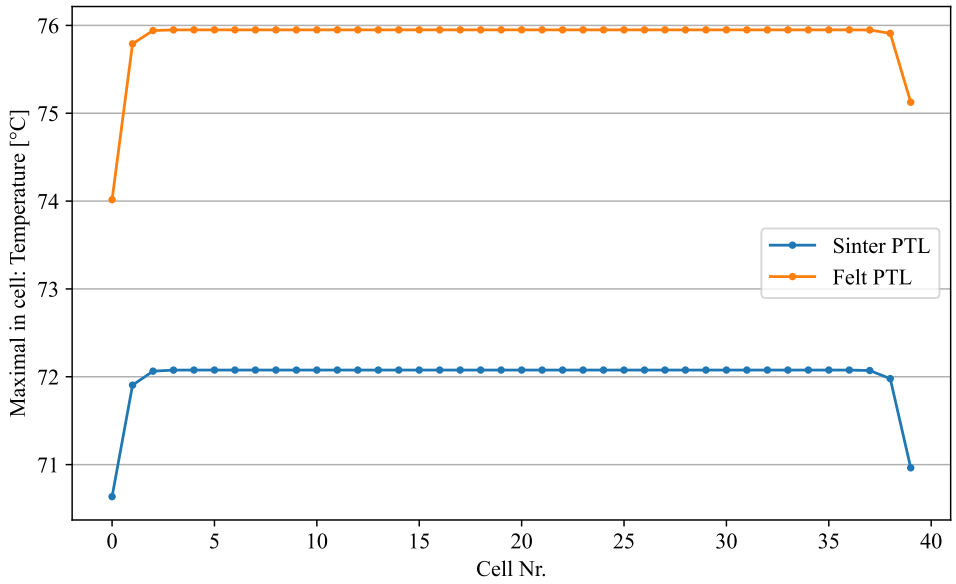

Figure 4.28.: Maximal temperatures in each cell of the stack under parallel flow with sinter PTL compared to the base case

High current density

When the current density was increased to $3\,\mathrm{A\,cm^{-2}}$, compared to the base scenario, the maximal temperature increased in counter-flow by 9 K to 87.0 °C. This resulted in an increase in temperature-gradient within the ECs in the stack by more than one half to 27.0 K. The voltage efficiency decreased in this case by 3.6 %. The temperature-distribution within the ECs did not change significantly and is presented in figure 4.29 for the middle cell in the stack in counter-flow. The thermal gradient between the FFs and the adjacent MEA increased from about 10 K at

$2\,\mathrm{A\,cm^{-2}}$ to 14 K in the middle of the ECs ($y = 1\,\mathrm{m}$) as shown in figure 4.30. The temperature in the FFs also increased significantly by 5 K in this cross-section under a constant mass flow of water.

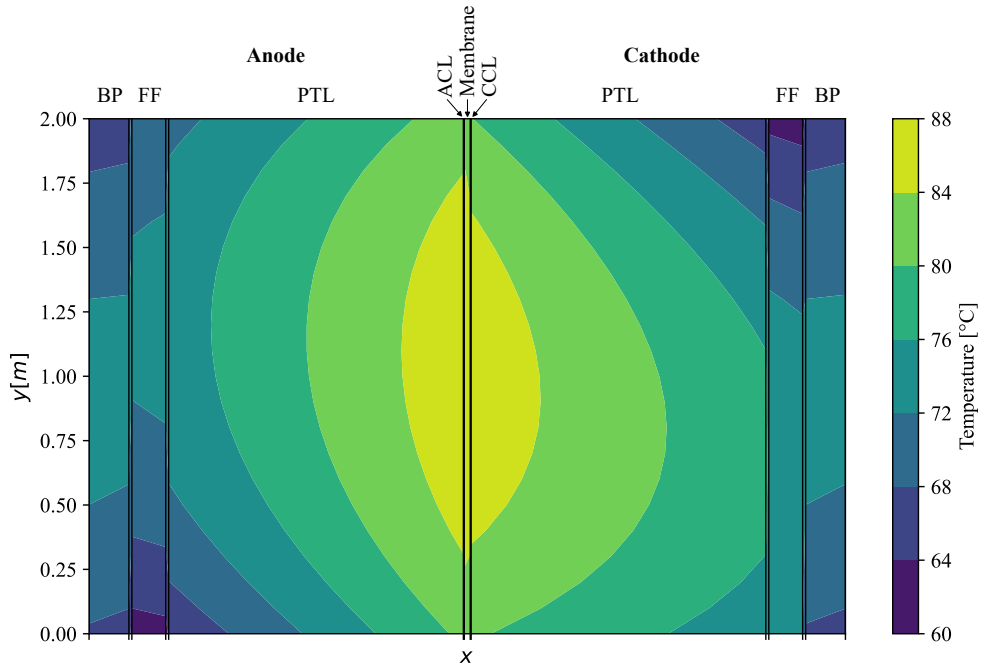

Figure 4.29.: Simulated temperature distribution in middle cell (no. 20) under counter-flow with a mean current density of $3\,\mathrm{A\,cm^{-2}}$

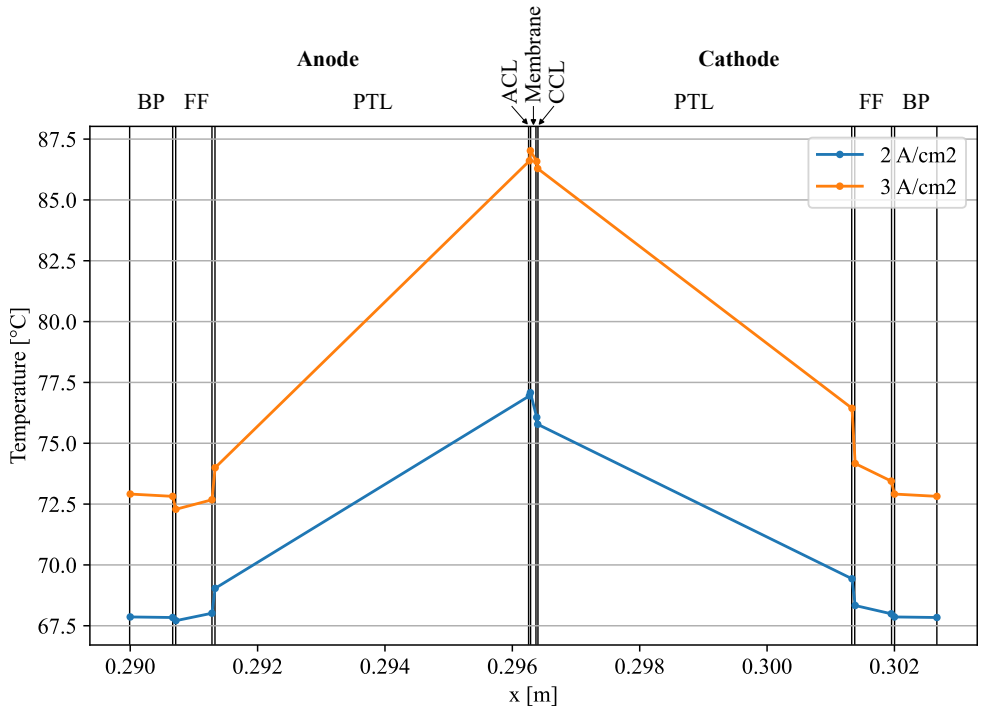

Figure 4.30.: Simulated temperature distribution at cross-section through middle cell (no. 20) at ($y = 1\,\mathrm{m}$) under counter-flow with a mean current density of $3\,\mathrm{A\,cm^{-2}}$

On a stack-level, the temperature-distribution did not change significantly. Only the temperature gradients over the last two cells on the right side decreased slightly compared to lower current densities, and temperatures were overall higher (figure 4.31).

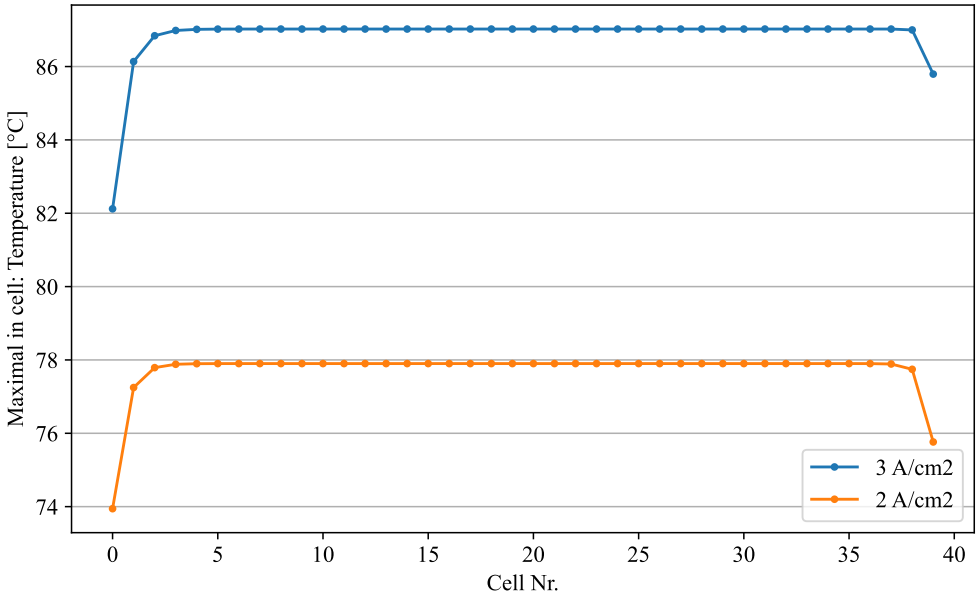

Figure 4.31.: Maximal temperatures in each cell of the stack under counter-flow with a mean current density of 2 and 3 $\mathrm{A\,cm^{-2}}$

The results were similar for the stack in parallel flow. The maximal temperature-gradient within the ECs increased to 26.1 K, with a maximal temperature of 86.1 °C. The temperature gradient was thus in this scenario higher in parallel flow than in counter-flow. Also here the voltage efficiency decreased by 3.6 %. The temperature distribution within the ECs did not change significantly, as depicted in figure 4.32. On a stack-level, the temperature gradient over the last cells in the stack decreased also in parallel flow. Otherwise, the temperature gradients over the cells in the stack did not change significantly (figure 4.33).

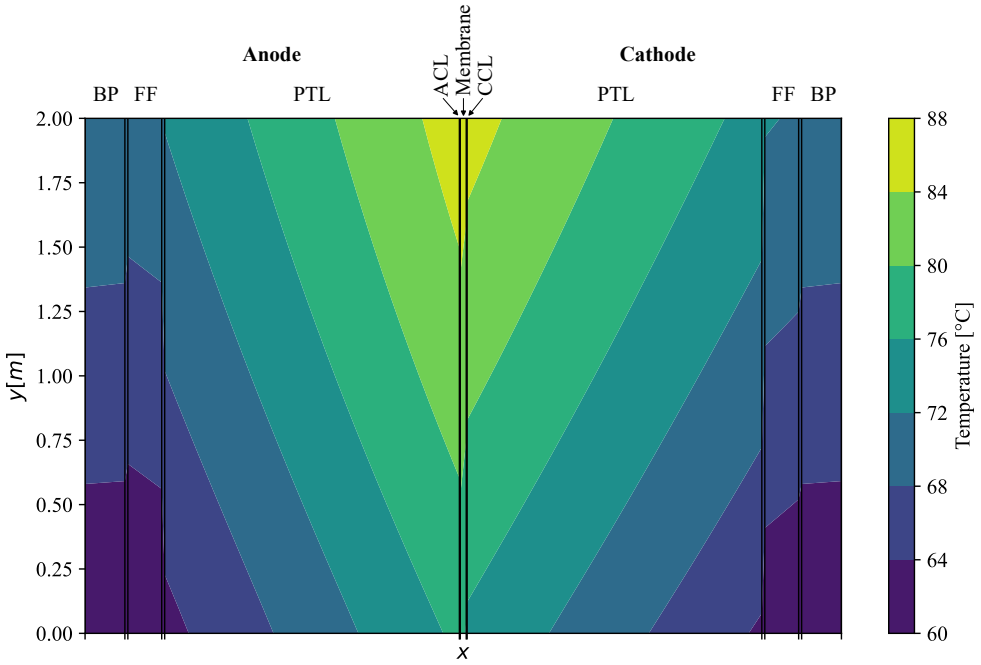

Figure 4.32.: Simulated temperature distribution in middle cell (no. 20) under parallel flow with a mean current density of 3 A cm^{-2}

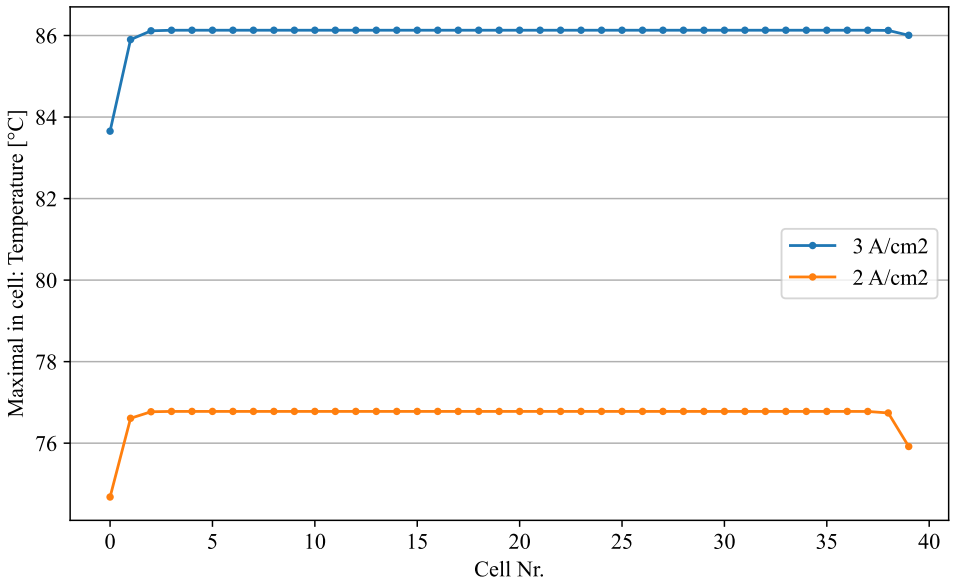

Figure 4.33.: Maximal temperatures in each cell of the stack under parallel flow with a mean current density of 2 and 3 A cm^{-2}

Without water drag

The effect of water drag through the membrane was then investigated by simulating the temperature distribution in parallel flow without water drag and comparing it to the base scenario with water drag. Figure 4.34 compares the temperature distribution at the FF inlets ($y = 0$ m) in the middle EC of the stack. Here the maximal temperature in the cell was about 2 K lower when

considering water drag through the membrane. The temperature decreased less in the cathodic PTL than in the anodic PTL, resulting in a slightly lower thermal gradient over the MEA with water drag.

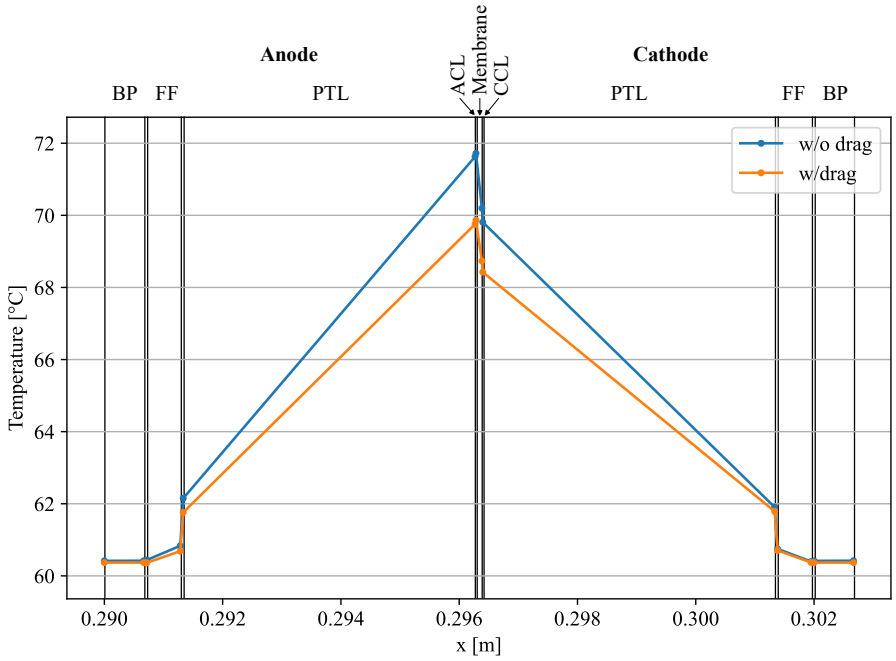

Figure 4.34.: Simulated temperature over middle cell (no. 20) at the FF-inlets under parallel flow with and without water drag

The difference between the maximal cell temperatures at the FF outlets ($y = 2\,\mathrm{m}$, figure 4.35) was with about 3 K 50 % higher than the difference at the inlets.

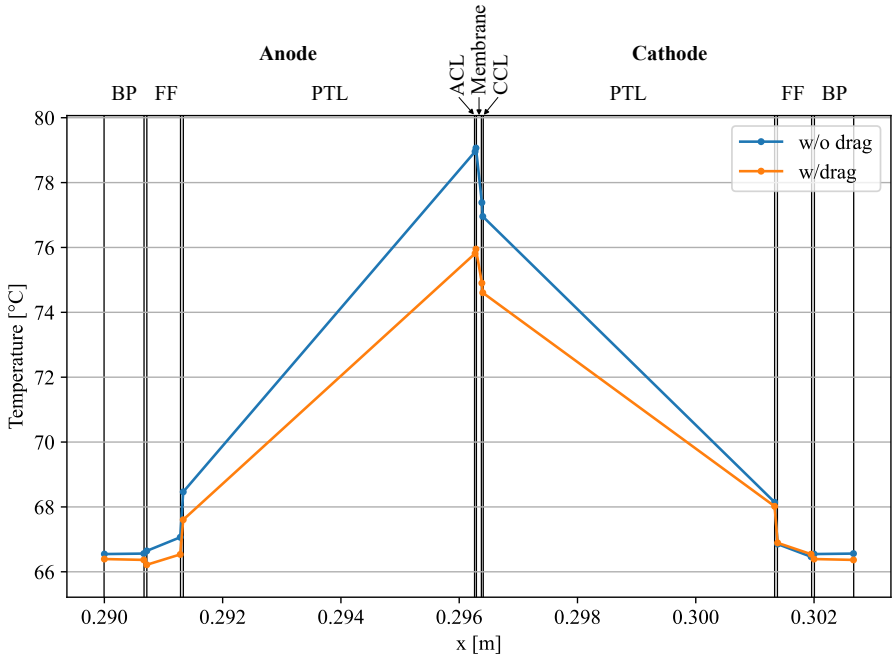

Figure 4.35.: Simulated temperature over middle cell (no. 20) at the FF-outlets under parallel flow with and without water drag

In order to compare the increase in temperature along the channels of the FF, the maximal temperature, occurring at the anodic surface of the membrane, is plotted along the channels (y-direction) in figure 4.36. The temperature in the membrane was predicted to be overall lower when water drag was considered. The difference increased towards the outlets, as described before. In the anodic FF, the temperature was also overall lower with water drag, with a difference of about 0.5 K at the outlets (figure 4.37a). The temperature in the cathodic FF was with a difference of about 0.1 K slightly higher when water drag was considered (figure 4.37b). The water drag thus led to a significant decrease in overall cell temperature, but slightly increased the temperatures in the cathodic FF.
The current density within the ECs increased from 2.008 A cm^{-2} to 2.044 A cm^{-2} at a constant cell-voltage of 1.964 V when the water drag was disabled.

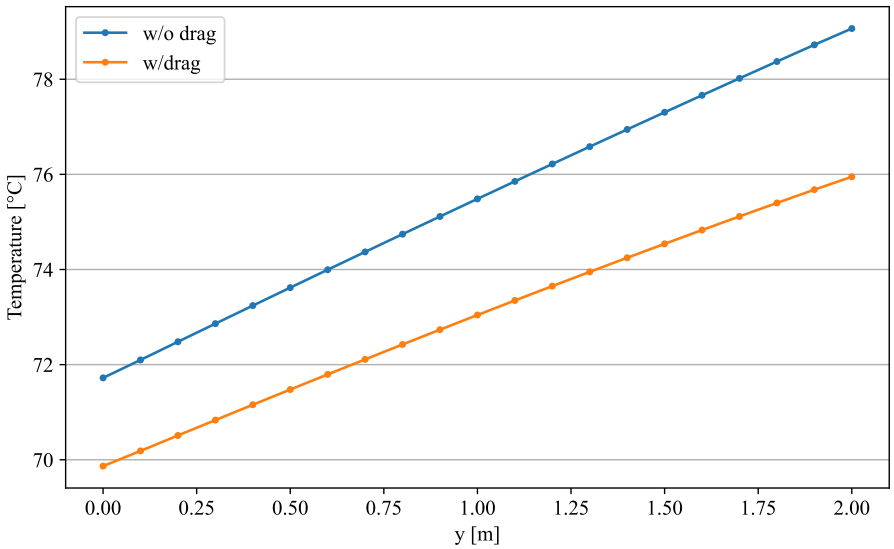

Figure 4.36.: Simulated temperature in the membrane of the middle cell (no. 20) under parallel flow along the y-axis with and without water drag

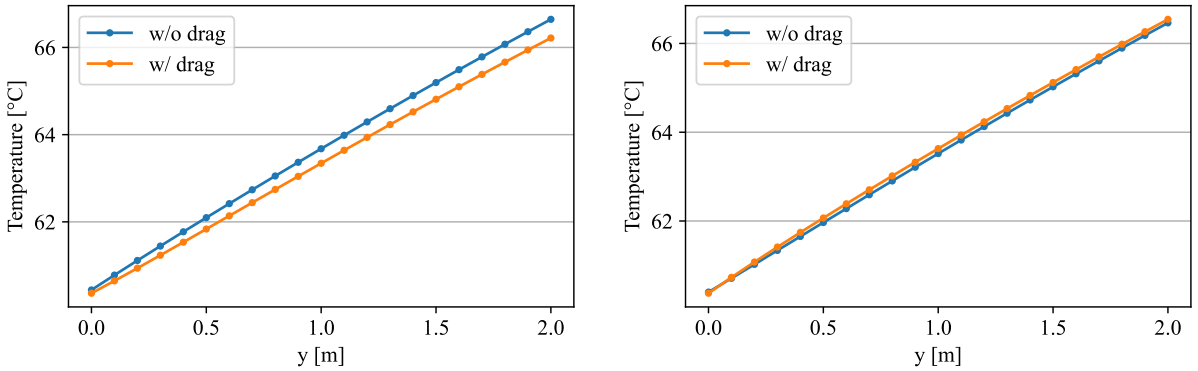

(a) Anodic FF **(b)** Cathodic FF

Figure 4.37.: Simulated temperature in the FFs of the middle cell (no. 20) under parallel flow along the y-axis with and without water drag

Warmer cathode

The temperature at the inlet of the cathodic FF was then increased to 63 °C, while the anodic inlet-temperature was decreased to 57 °C. This led to an overall increase in temperature in the cathodic half-cell and a decrease in temperature in the anodic half-cell. The thermal gradients within the ECs increased by 3.4 K with an almost constant maximal temperature of 77.4 °C in counter-flow. The thermal gradient over the MEA could not notably be reduced by altering the inlet-temperatures, as shown in figure 4.38 for a cross-section through the middle of the cell ($y = 1\,\text{m}$). Thus, also the voltage efficiency did not change. The temperature in the FFs in this cross-section only deviated by 0.8 K in the cathodic FF and by 0.3 K anodic FF from the scenario with equal temperatures at the FF inlets. Over the stack, compared to equal inlet temperatures, a higher temperature decrease could be noted in the outer cells on the left side of the stack and a lower gradient over the last cells on the right side (figure 4.39). The two-dimensional temperature distribution over the cell is for further reference depicted in the appendix in figure A.3.

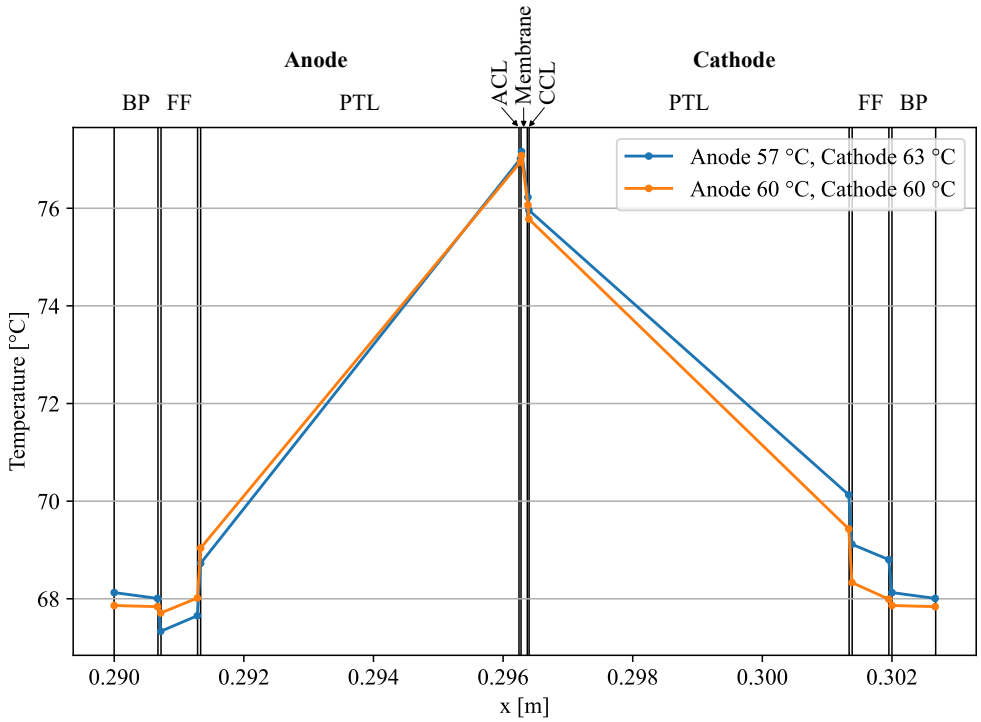

Figure 4.38.: Simulated temperature distribution in middle cell (no. 20) at $y = 1\,\text{m}$ under counter-flow with an increased inlet-temperature in the cathodic FF compared to the base case

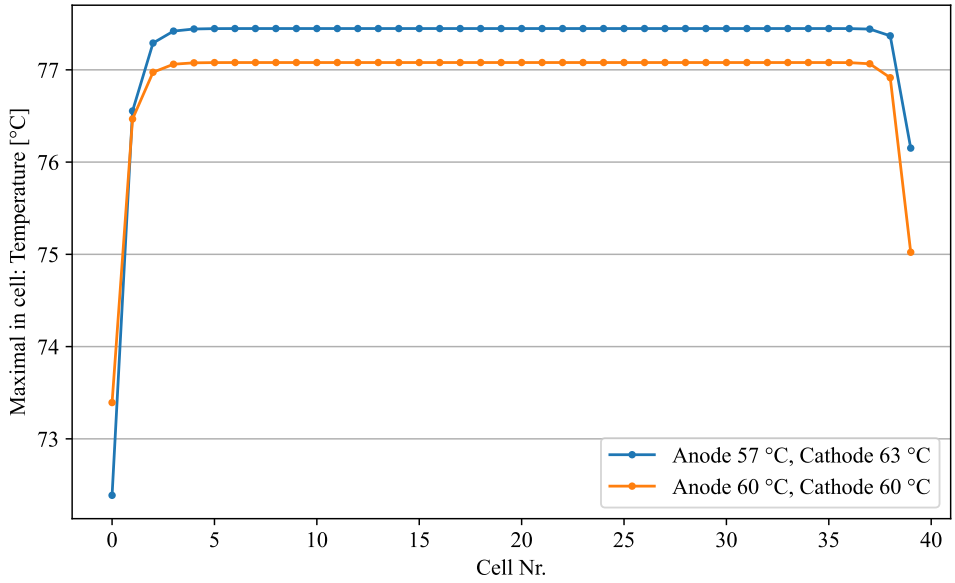

Figure 4.39.: Maximal temperatures in each cell of the stack under counter-flow with an increased inlet-temperature in the cathodic FF compared to the base case

Similar effects were predicted for parallel flow, where the thermal gradient increased by 3.0 K and thus slightly less than in counter-flow. This resulted in a maximal temperature of 76.0 °C with no change in voltage efficiency. The temperature distribution within the ECs was outside the FFs not notably affected as depicted in figure 4.40 for a cross-section through the middle of the cell ($y = 1\,\mathrm{m}$). The impact on the temperatures in the FFs was here even lower than in counter-flow. The impacts on the temperature distribution over the stack were in analogy to counter-flow, with a higher decrease on the left side and a smaller decrease on the right side of the stack (figure 4.41). The two-dimensional temperature distribution over the cell is for further reference depicted in the appendix in figure A.4.

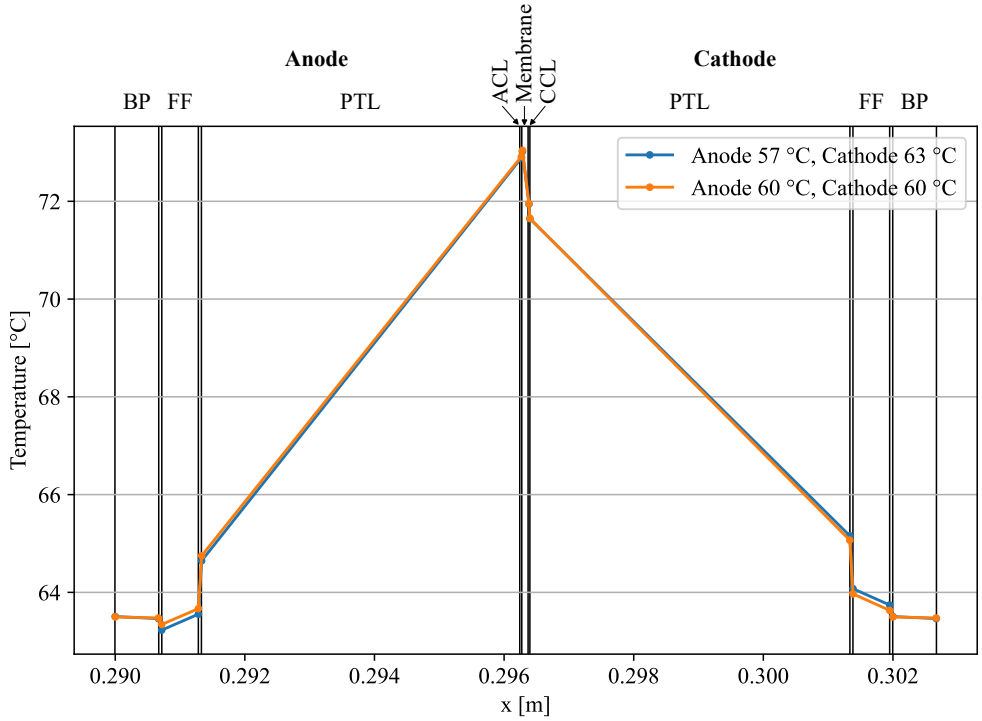

Figure 4.40.: Simulated temperature distribution in middle cell (no. 20) at $y = 2\,\mathrm{m}$ under parallel flow with an increased inlet-temperature in the cathodic FF compared to the base case

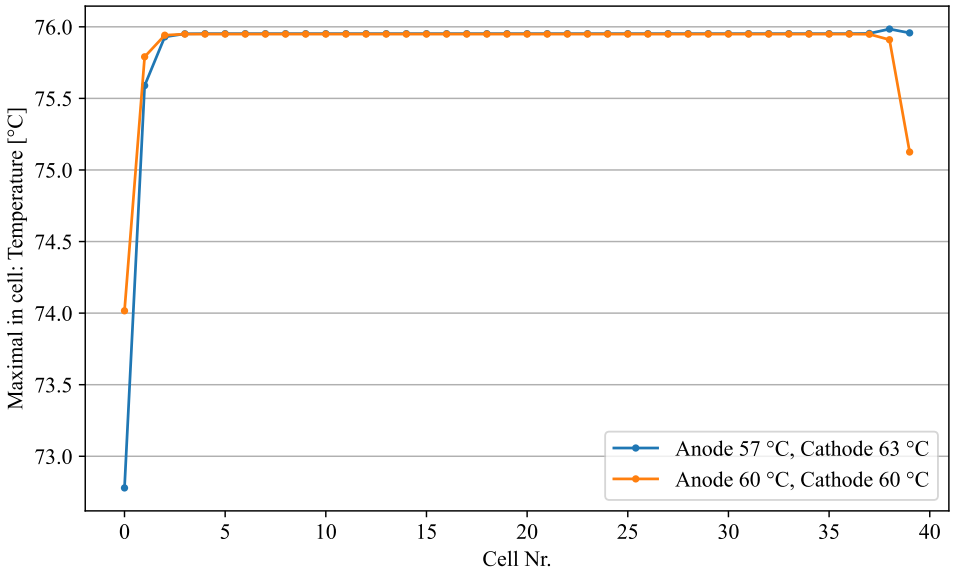

Figure 4.41.: Maximal temperatures in each cell of the stack under parallel flow with an increased inlet-temperature in the cathodic FF compared to the base case

5. Discussion

5.1. Thermal conductivity and compressibility

In the following, the measured thermal conductivities are discussed and compared with literature. The thermal conductivities of the FC materials were measured to validate the procedure, which was then used to determine the thermal conductivities of EC materials.
All thermal conductivities were measured close to ambient temperature to minimize the heat flux between the measurement apparatus and ambient to guarantee a high certainty of the measurements. During actual PEMEC operation, however, the temperature is higher with about 50 to 80 °C [3]. Khandelwal and Mench [24] measured the temperature dependency for the thermal conductivity of Nafion® 1100 EW, which decreased with water content and was negligible for 80 or 100 % humidified material. For the other layers, no study is known that examined the temperature dependency of the thermal conductivity. Measuring the conductivities at different temperatures would exceed the scope of this work. It was therefore assumed that the thermal conductivity at PEMEC operating temperature can be approximated by the thermal conductivity at ambient temperature for all relevant materials.
The uncertainty of the compression measurements was high for all measured materials. This can be explained by the manual thickness measurements, which were used to determine the thickness without compaction pressure outside the thermal conductivity measurement apparatus. The thickness was measured at different locations of the sample with an electronic micrometer to derive a mean thickness. The thickness often varied over the sample, which can be explained by manufacturing tolerances in the material and eventually slight punctual compaction pressure applied through the micrometer. The uncertainty of the results was therefore high compared to the small thickness of the samples. As the thickness measured with the micrometer has always been used as a reference value for the thicknesses measured under compaction pressure, the calculated compression also has a relatively high uncertainty. Measuring the thickness within the thermal conductivity apparatus without applying compaction pressure was not possible as some pressure was always applied through the weight of the apparatus itself. However, as the compressibility of the materials was not of high importance for the temperature simulation in this study, the accuracy of the compression measurements was regarded as sufficient for the purpose of this work. The absolute thicknesses of the samples under pressure, which were used to calculate the thermal conductivities from the thermal resistances, were not affected as they were measured with higher precision using the gauges inside the apparatus.

5.1.1. FC materials

Thermal conductivities of fuel-cell materials have been measured in several studies [23, 24, 25, 26, 27, 28, 29] and were used here to verify the measurement procedure. The reported values for dry Nafion® vary between 0.16 and 0.24 $\mathrm{W\,m^{-1}\,K^{-1}}$. The here measured thermal conductivity of $(0.18 \pm 0.01)\,\mathrm{W\,m^{-1}\,K^{-1}}$ lies within these values and fits very well with the conductivity measured by Burheim *et al.* [23] on the same rig with a deviation of only $2\,\mathrm{mW\,m^{-1}\,K^{-1}}$, which is below the uncertainties of measurement. Both Burheim *et al.* and this study measured only a small increase in thermal conductivity with increasing compaction pressure, which lies within the uncertainties of measurement. The other studies did not assess the influence of compaction pressure on the thermal conductivity. A significant compressibility for Nafion® at increased pressure could neither be identified in this work nor by Burheim *et al.*

The thermal conductivity of wet Nafion® has, to best of the author's knowledge, only been measured by Burheim *et al.* [23] to $(0.25 \pm 0.02)\,\mathrm{W\,m^{-1}\,K^{-1}}$ for a membrane soaked in purified water. The wet thermal conductivity measured here was with $(0.26 \pm 0.03)\,\mathrm{W\,m^{-1}\,K^{-1}}$ slightly higher, but the deviation was within the uncertainties of measurement. The samples showed no sign of compressibility under higher pressure, which matches the findings of Burheim *et al.*

Using the thickness as a measure of water content in the membranes proved as very unreliable, with an uncertainty of more than 65 % of the measured values. This can be explained by the fact that the increase in thickness due to humidification depends highly on the temperature of the membrane. Peron *et al.* [53] measured an increase of (10 ± 4) % in thickness after humidification for Nafion® 211 at 23 °C and (29 ± 2) % at 100 °C. The measurements are therefore highly dependent on the temperature distribution in the sample which is, among others, highly affected by the time since the sample had been taken out of the heated measurement apparatus as well as by the thermal mass of the sample. Measuring the thickness using a micrometer was furthermore only possible with limited accuracy, as described above. The weight, however, could be measured with a high certainty of 1 mg. The thickness was therefore not regarded an appropriate measure for the humidification level of the sample. In the following, the difference in weight between dry and wet sample was used as a measure.

The deviation between the water content before and after the measurement of the wet membrane was relatively high, with a decrease from (24 ± 10) wt.% to (11 ± 7) wt.%. The effect could be attributed to dryout where water leaves the sample area by bypassing the sealing. In order to rule out possible influences of this effect on the measurements, the thermal conductivity at 4.6 bar was measured again at the end of the measurement and compared to the initial measurement. No significant difference could be noticed here. The dryout was therefore attributed to the fact that some water was pressed out of the sample due to the compressing forces in the rig prior to the first conductivity measurement. The same effect is to be expected in actual fuel cell operation once compaction pressure is applied. The humidification during the measurement was therefore considered to be the maximal humidification level for each measured pressure with exception for the last pressure step at 4.6 bar.

Peron *et al.* [53] measured a water uptake of (20 ± 1) wt.% at 23 °C in Nafion® 211. This lies

close to the humidification measured prior to the conductivity measurements. The slightly higher value measured in this study might be attributed to small water droplets on the sample, which could not be fully eliminated by drying with the paper towel. The membrane can therefore be assumed to be fully humidified and thus have a λ of 22 ± 1 [54, 55].
Both Burheim *et al.* and this study did not find a significant impact of compaction pressure on the thermal conductivity of the Nafion® membrane. The assumption of having no significant contact resistance between the single layers of Nafion® had therefore been proven valid, as the deviation between this study, which stacked Nafion® of a single thickness, and Burheim *et al.*, who used Nafion® samples of different thicknesses, lies within the uncertainties of measurement.

The measured thermal conductivity of dry CLs varies in the literature from 0.04 to 0.27 $\mathrm{W\,m^{-1}\,K^{-1}}$ [24, 27, 28, 29]. The high variation might be attributed to different compositions of the CLs examined in the studies. The conductivity measured here lies with $(0.13 \pm 0.02)\,\mathrm{W\,m^{-1}\,K^{-1}}$ within the interval and is therefore assumed to be valid. In order to determine the reason for the deviation of the conductivity to each mentioned study, a more detailed analysis of the composition of the CLs used in the examined MEA would be required. This was out of the scope of this work. All mentioned studies in literature as well as this work detected an increasing thermal conductivity with increasing pressure in the CL. To best of the author's knowledge, no literature exists on the compressibility of the CLs. However, due to the highly porous structure of the CLs, the measured compressibility seems reasonable. The high uncertainties of measurement can be attributed to the indirect measurement using the MEA.
The thermal conductivity of wet CLs has, to best of the author's knowledge, only been measured by Burheim *et al.* [29]. Burheim *et al.* measured thermal conductivities between (0.10 ± 0.13) and $(0.2 \pm 0.3)\,\mathrm{W\,m^{-1}\,K^{-1}}$ at 4.6 bar as well as between (0.12 ± 0.02) and $(0.4 \pm 0.9)\,\mathrm{W\,m^{-1}\,K^{-1}}$ at 13.8 bar depending on the composition of the CL. Especially the Nafion®-content showed a high influence on the thermal conductivity. The thermal conductivities measured in this paper were with a value from $(0.61 \pm 0.05)\,\mathrm{W\,m^{-1}\,K^{-1}}$ at 4.6 bar to $(0.67 \pm 0.07)\,\mathrm{W\,m^{-1}\,K^{-1}}$ at 13.9 bar above Burheim *et al.*'s measurements. The increase in thermal conductivity with compaction pressure was with about $(0.06 \pm 0.07)\,\mathrm{W\,m^{-1}\,K^{-1}}$ lower than the uncertainties of measurement, and lower than the increase measured by Burheim *et al.* with $(0.3 \pm 1.0)\,\mathrm{W\,m^{-1}\,K^{-1}}$ for the samples with the highest thermal conductivity. As the hysteresis effect was also very pronounced in the measurements of Burheim *et al.*, an explanation for the difference might be that Burheim *et al.* used fresh samples for the measurement, while this work used samples that were already precompressed through being used in a fuel cell. This could also explain the higher thermal conductivity under lower compaction pressures in this study. Yet, it cannot explain the difference in thermal conductivity at high compaction pressures. One explanation for this could be a different humidification level. The humidification in this work was with $\lambda = 35 \pm 24$ lower than the humidification of $\lambda = 70 \pm 30$ determined by Burheim *et al.* However, the here calculated humidification level underlay assumptions on the composition of the CL and the water distribution within the MEA and had high uncertainties in this work as well as in the work of Burheim *et al.* To determine the exact humidification level, the composition of the CL and the

water distribution within the MEA would have to be examined in detail, which was out of the scope of this work. Another reason for the deviation could be a difference in composition, which seem to have a high influence on the wet thermal conductivities as measured by Burheim *et al.* [29] and also had a high influence on dry thermal conductivities of CL as described before. As no other literature was available on the thermal conductivity of wet CL and the measurements fitted well with literature for the dry measurements, the measured values were assumed to be valid and the differences to the values measure by Burheim *et al.* were accounted to a different composition, precompression, difference in humidification and measurement uncertainties.
The measurement in hysteresis at 4.6 bar showed a much higher thermal conductivity and uncertainty than all other measurements. This might be attributed to an altered water distribution in the samples (e.g. water pressed out of the membrane in the CLs or vice versa) or a non-settled temperature-gradient over the measurement rods. The value was considered an outlier and is therefore not further discussed here.
As for the dry CLs, no literature is known to exist on the compressibility of wet CL. As the compressibility over the measured pressures lies within the same range as the compressibility measured for dry CLs, it was assumed as valid.

The measurement procedure had thus been proven valid, as thermal conductivities comparable to the literature values for Nafion® have been measured. The thermal conductivities were also measured within the literature values for dry CL and close to the literature values for wet CL. However, the comparability of the measured thermal conductivities of the CLs with literature is limited due to the unknown composition of the CLs used in the MEA, which has a high influence on the thermal conductivity as proven in literature [29].

5.1.2. EC materials

The deviation between the measurement results with and without re-humidifying the samples before changing the pressure was within the uncertainties of measurement. The decrease in humidification during the measurements was therefore assumed to be mainly a result of increasing compaction and not the duration of measurement. The decrease in humidification can therefore be expected to be the same in actual EC operation, where compaction pressure is applied on the stack. Therefore, in the following only the results of the measurements without re-humidification are discussed, but the same conclusions apply to the measurements with re-humidification because of the similar results.

The Tion5 membrane showed a slightly higher thermal conductivity than the Nafion® membranes, with an increase by about 5 % in the dry and about 20 % in the wet measurements. However, the Nafion® 211 membrane was with 25.4 µm much thinner than the Tion5 PFSA membrane with a thickness of 127 µm (both thicknesses according to manufacturer). The Nafion® membrane has therefore a lower total thermal resistance than the Tion5 membrane even though it has a lower thermal conductivity. The Tion5 membrane was measured to be less compressible than the Nafion® samples and showed an increase in thermal conductivity with pressure for dry material.

Both membranes were more conductive and less compressible when being wet. The impact of pressure on the thermal conductivities was negligible for both wet Nafion® and wet Tion5. These similarities can be attributed to the fact that both are PFSA membranes and thus have a similar chemical structure.
Thus, the Tion5 samples showed a higher conductivity than Nafion® , with a significant increase in conductivity when being humidified. The conductivity was not relevantly affected by pressure for both the dry and wet material.

The wet MEA showed a higher conductivity than the dry one. The humidification level was with an average of (13 ± 1) wt.% significantly lower than that of the FC MEA with an average of (28 ± 1) wt.%. Both the Nafion® and the Tion5 membrane had a similar humidification level after being soaked in water (about 24 wt.%), which means that the examined EC CL absorbed less water than the one used in the FC sample.
The thermal conductivities and compressibility for the CL had been derived by combining the MEA and membrane measurements. The thermal conductivity of the dry EC CL was calculated to be higher than the one calculated for the FC CL in this study, but was within the literature values for FC CL. As for the FC MEA, the conductivity increased significantly when applying more compaction pressure. This effect can be attributed to the fibrous porous structure of the CL, which contains less void spaces and a better fibre-fibre contact when being compressed. This was underlined by the high compressibility of the material with a compression of (19 ± 10) % at 4.6 bar and (31 ± 9) % at 16 bar.
The wet CL showed a thermal conductivity that was significantly lower than measured in this study for the FC CL but within the literature values of FC CL and higher than the thermal conductivity of dry CL. The thermal conductivity decreased during the measurement. This effect could be attributed to the pressure-induced dryout of the sample as described earlier, which can be assumed to also be present in-situ, when compaction pressure is applied on the stack. That this effect does not occur in the FC CL could be explained by the lower initial humidification level of the EC CL. Another possible explanation for the effect is a lower increase in thermal conductivity of the Tion5 membrane under pressure when inside a MEA than in the separate measurements. This would lead to an underestimation of the CL's thermal conductivity. In order to further investigate the behaviour of the EC CL, its thermal conductivity would have to be measured outside the MEA, e.g. printed onto a copper foil as in [29], which was out of the scope of this work.
While the compression of the wet sample did not show any significant hysteresis, the dry sample was more compressed at the end of the measurement than in the beginning. This might be attributed to the fact that the MEA was new and had not been compressed before, however the hysteresis effect was within the uncertainties of measurement and might therefore also be attributed to arbitrary influences.
The thermal conductivities of the both dry and wet CL were thus within the literature values for FC CL. This shows that in CLs the impact of the actual composition is higher than the difference between EC and FC materials. The thermal conductivity of the dry CL increased

with compaction pressure, whereas the thermal conductivity of the wet CL decreased with compaction pressure. Whether this effect can be attributed to pressure-induced dryout or a change in conductivity in the Tion5 membrane must be examined in further experiments. For the further course of this study, however, it was assumed that the decrease is due to pressure induced dryout and the measured values were used in the simulation.

The conductivity of dry platinized titanium felt PTL was measured to $(0.32 \pm 0.04)\,\mathrm{W\,m^{-1}\,K^{-1}}$ at 4.6 bar, increasing by over 60 % when the compaction pressure was increased to 16 bar. As the thickness did not change significantly ((1.4 ± 0.6) % maximal compression), the increase in thermal conductivity cannot be attributed to an increasing density of the material. However, as the conductivity within solid titanium fibres is with $21\,\mathrm{W\,m^{-1}\,K^{-1}}$ [56, p. 206] very high compared to the conductivity of the air-filled void spaces ($0.025\,\mathrm{W\,m^{-1}\,K^{-1}}$ [57, p. 375]), the main thermal resistance in the pathway of the heat through the PTL can be attributed to the fibre-fibre contact areas. When thermal conductivity is increased in these areas, the overall conductivity of the material increases significantly, as Burheim *et al.* showed for fibrous PEMFC PTL layers [23, 33]. The contact between the fibres can be assumed to increase with increasing pressure without significantly altering the thickness of the material, which can explain the increase in thermal conductivity. A significant increase in thermal conductivity with increasing compaction pressure was also measured by Bock *et al.* [7] for sintered titanium PTL. Both Bock *et al.* and this study assumed the contact resistance between the samples to be negligible for the titan PTL. It may be questioned if this assumption is valid when a cross-section of the sample-sample contact area is inspected under the microscope, as in figure 5.1. It is visible, that the samples are mainly in contact at discrete regions where fibres stick out of the surface of either sample (red circle in figure 5.1). This can be explained by the rigid structure of the material. The air-gap between the samples is significantly larger than the void volumes inside the samples, which could imply a non-negligible sample-sample contact resistance. Another impacting factor for the increasing conductivity with compaction pressure could therefore also be a decrease in air-gap between the samples, resulting in a lower sample-sample contact resistance. In this case, the inherent bulk thermal conductivity of the samples would be underestimated at low pressures. However, also in literature the thermal sample-sample contact resistance is neglected in similar experiments [38]. In order to determine the main factor responsible for the increased thermal conductivity under higher pressures, titanium PTL samples of different thicknesses would have to be used in the thermal conductivity measurements instead of stacked samples. This was out of the scope of this work as the material was only available in a single thickness.
The overall thermal conductivity measured by Bock *et al.* for dry sintered titanium PTL was with 1.2 to $1.7\,\mathrm{W\,m^{-1}\,K^{-1}}$ at 5 bar compaction pressure higher than measured in this study for the titanium felt. The difference to the measurements in this study can be explained by the fact, that the porosity in the sintered samples measured by Bock *et al.* was only about 30 % compared to a porosity of (52 ± 5) % in this study, so that more solid titanium was available for heat conduction in the sintered titanium than in the titanium felt. Sintered titanium also has a more bulky structure, whereas titanium felt consists of thin titanium threads (cf. [7, 35]), so that

different thermal conductivities can be to be expected even for the same porosity.

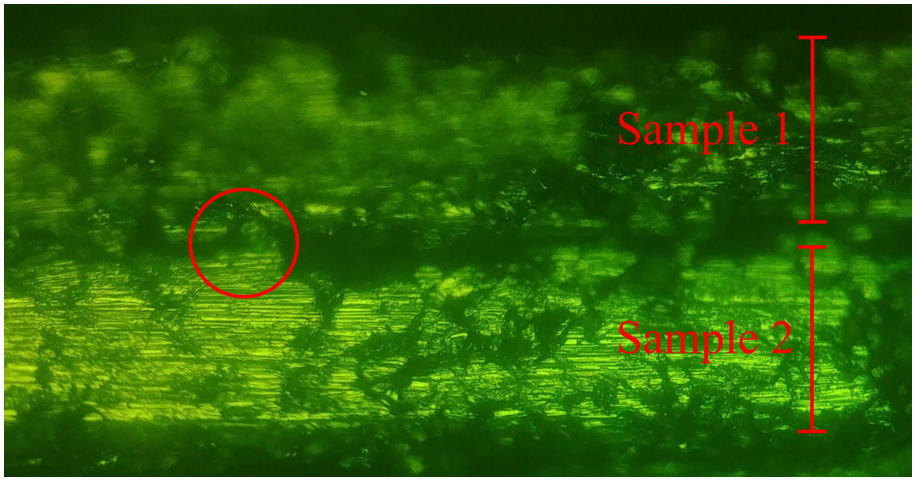

Figure 5.1.: Microscopic image of sample-sample contact area of platinized titanium felt with a thickness of 250 µm per sample

The wet titanium felt had with $(2.50 \pm 0.17)\,\mathrm{W\,m^{-1}\,K^{-1}}$ at 4.6 bar a significantly higher thermal conductivity than the dry material. The increase can be explained by the fact that the conductivity in the fibre-fibre contact regions is improved by the induced water, which has with $0.6\,\mathrm{W\,m^{-1}\,K^{-1}}$ [57] a higher thermal conductivity than the air filled void spaces. Thus, the heat has a larger area of conductive material to pass from one titanium fibre to another (cf. figure 5.2). As for the dry PTL, the conductivity of the wet PTL increased further with compaction pressure. This can be explained by the same effects as for the dry PTL: The compaction pressure increases the contact between the titanium fibres and might decrease the contact resistance between the samples. The humidification level decreased significantly during the measurements, which would imply a decrease in conductivity. However, for the thermal conductivity mainly the water-droplets at the fibre-fibre contact areas are of importance, which are also the last droplets of water that dry out [58]. As enough water was left in the sample, the contact areas were still surrounded by water so that the conductivity was not significantly affected.

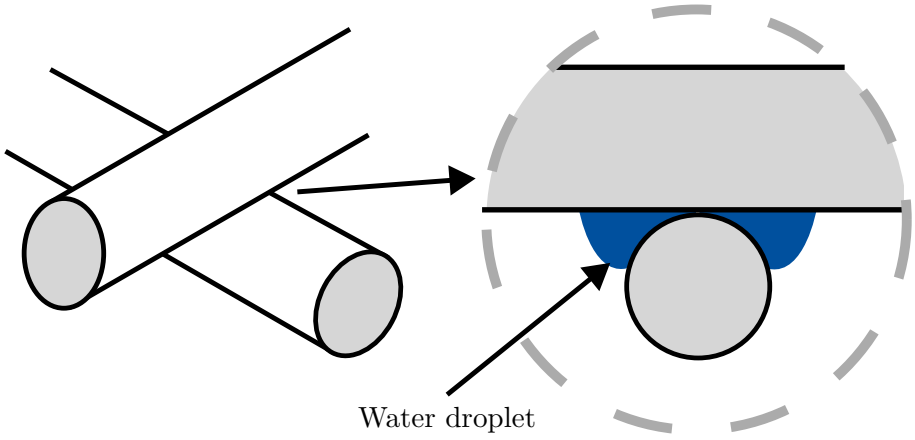

Figure 5.2.: Schematic of fibre-fibre contact in felt PTL with water droplet (based on [23])

Schuler *et al.* [38] approximated the thermal conductivity of titanium felt with varying porosities and fibre diameters in-situ in an EC by measuring the temperature dependent membrane resistance. He proposes a thermal conductivity between 5.3 and 6.3 $\mathrm{W\,m^{-1}\,K^{-1}}$ for titanium felt PTL with 56 % porosity and between 1.6 and 3.6 $\mathrm{W\,m^{-1}\,K^{-1}}$ for 76 % porosity. The PTL can be assumed to be humidified during the in-situ measurements. The here measured thermal conductivity falls within the conductivities measured by Schuler *et al.* for high porosities, however the porosity of the samples was calculated to (52 ± 5) %, which lies closer to Schuler *et al.*'s low porosity samples. The difference in conductivity might be explained by the fact that the samples used in this study were platinum coated, while the samples used by Schuler *et al.* were uncoated. Bock *et al.* [7] showed for dry sintered titan PTL that the surface treatment can have an impact on the thermal conductivity and measured a decrease up to 25 % in dry thermal conductivity for PTL of platinum coated titanium compared to uncoated titanium. Wet thermal conductivities were not measured for platinum coated samples by Bock *et al.* and are not known to exist elsewhere in literature. Also, in-situ thermal conductivity measurements as conducted by Schuler *et al.* always underlie significant uncertainties, as discussed in section 3.1.
Thus, the thermal conductivity of titanium felt PTL was measured to increase significantly with increasing pressure and to increase more than five times when being humidified, while no significant compression or swelling could be determined. Comparing the measurements to literature is only possible to a limited extent, as both dry and wet conductivities are highly influenced by the composition and structure of the material. Further research is required on the impact of the sample-sample contact resistance on the determined thermal conductivity to further verify the results of the measurements.

5.2. Temperature distribution in stack

In the following, firstly, the results of the validation are discussed to assess variations from the predictions in literature. Secondly, the results of the scenarios simulated with the validated model are discussed and compared.

5.2.1. Validation

Based on the results presented in section 4.2.1, the following section discusses differences between the results of this study and the prediction of the reference models to assess the validity of this study's model. The results of the mesh refinement study and using low/high conductivity values were as expected and are therefore not further discussed here.

The maximal temperatures simulated by Bock *et al.* [7] were overall higher than predicted by the model of this study when using the same overpotentials. This can be explained by a combination of several factors. Firstly, Bock *et al.* assumed temperature-controlled BPs. This is a valid assumption for single-cell tests where the end-plates are temperature-controlled, however, BPs in EC stacks are often only cooled by the fluid in the FFs. Therefore, a controlled FF temperature

was assumed in this model. This led to an overall lower temperature as the pathway between heat sources and sinks is shorter. Secondly, the influence of mass flowing through the different layers of the EC in x-direction due to the electrolysis reaction and water drag was considered in this model but not by Bock *et al.* This leads to additional cooling of the inner layers of the EC and thus an increased effective thermal conductivity. It explains why the maximal temperature and thus the cathodic temperature gradients were less affected by the PTL's conductivity in the results of this study than predicted by Bock *et al.*, who considered only heat conduction. At the interface between PTL and FF, the temperature would be expected to be the same for all three PTLs materials as the same amount of heat must be led away through the FF. At the anode side interface, however, the temperature was simulated to be slightly higher for Sinter 1 material and at the cathode side for Sinter 3. This can be explained by more heat flowing to the cathodic FF when the thermal conductivity of the PTL decreases due to the then relatively higher impact of heat transport through mass flows. Bock *et al.* predicts a higher temperature for the Sinter 3 materials at both the anodic and cathodic interface, as they take into account the temperature gradient between channels of the FF and ribs of the BP in z-direction, which increases with decreasing PTL conductivity. This effect is neglected in this study, which explains the differences in temperature distribution at this position. This effect equalled about out with the decrease in membrane temperature compared to Bock *et al.* and led to similar thermal gradients over the anodic PTL.
Using the overpotentials as described by Krenz *et al.* led to lower temperature gradients, which matches expectations, as the V-i characteristics show a lower voltage and thus lower overpotentials at a current density of $3\,\mathrm{A\,cm^{-2}}$.
Thus, the temperature gradients simulated by Bock *et al.* and this study are very similar. All deviations can be explained by different assumptions due to simulating a stack and not a single cell, including the mass flow in x-direction through the EC and neglecting temperature gradients between channels and ribs of the BPs. The simulation is therefore assumed to be valid on a cell level.

The temperatures and heat fluxes predicted by Krenz *et al.* [5] fit overall very well with the mean values of the predictions of this study, both for parallel and counter-flow. The simulation can therefore be assumed to also be valid on a stack level. It comparison also shows that Krenz *et al.* underestimated the maximal temperatures in the cells by 2 to 4 K or 20 to 40 % by not considering the temperature gradients within the cells.

The impact of the simplified assumption of negligible contact resistances between the single layers in the ECs could not be determined here as measuring the actual contact resistances inside the MEA is difficult and exceeded the scope of this work. Also in literature these contact resistances are, to best of the author's knowledge, always neglected [7, 8, 9]. It was therefore assumed that this simplification did not have a significant impact on the results of the simulation.
Furthermore, it was assumed that all parts of the cell are always fully humidified. Considering partial humidification levels would require further measurements on the thermal conductivity of

EC materials at different humidification levels, which exceeded the scope of this work. However, a full humidification in all layers of the cell can be considered close to reality, as both FFs were regarded to always be flooded with water as proposed by Krenz *et al.* [5].
Assuming an equal temperature for solid and fluids within each mesh-cell overestimates the heat exchange rate between the solid and liquid phase. However, for the FFs the heat transport resistance was considered through the BLs. All mass flows in x-direction through the ECs were comparably small and are often neglected in literature [7, 9]. It was therefore assumed that the difference in temperature through the overestimation of heat transfer was small and did not affect the overall results of the simulations.

The simulation has thus been validated on both cell- and stack level for a stack with the V-i-characteristics described in section 3.2.1 and depicted in figure 4.8. It was shown that the maximal temperatures in the MEAs are underestimated by about 2 to 4 K when using lumped values inside the ECs in the stack. This equals an increase of about 20 to 40 % in total temperature gradients over the stack compared to Krenz *et al.*

5.2.2. Simulation

In the following, the effects of the different varied parameters on the temperature distribution within the stack are discussed and compared to literature where available.

Measured conductivities

Firstly, the deviations between the simulated temperatures using measured thermal conductivities at the upper and lower boundary of uncertainty are discussed. Afterwards, the general shapes of the simulated temperature distributions are evaluated and compared to literature.

Varying the thermal conductivities within the range of measurement uncertainties of this study did not notably affect the temperature distribution within the cell. However, it did impact the maximal cell temperatures within the stack, leading to an increase in thermal gradients by up to 1.2 K within a single cell in the stack when minimal conductivities were used instead of maximal conductivities. This corresponds to an uncertainty of 4 % for the mean value of the calculated thermal gradients. The deviation in maximal temperature also leads to some uncertainty in voltage efficiency, which increased by up to 0.11 % when using lower thermal conductivities, giving an uncertainty of 0.07 % for mean voltage efficiencies. These uncertainties do not apply to the comparison with the other simulated scenarios with equal thermal conductivity values but only to comparison with reality and are therefore only considered in this scenario.

The temperature within the ECs in the centre of the stack was predicted to be maximal between the ACL and membrane both in parallel and counter-flow operation. This matches with expectations as anodic overpotentials are significantly larger than cathodic overpotentials [7] and agrees with literature [7, 8]. The temperature-gradient within a single EC in the stack was with

(16.5 ± 0.6) K in parallel flow significantly higher than the maximal gradients predicted by Krenz *et al.* [5] with around 9 K. The same goes for counter-flow, where Krenz *et al.* predicted thermal gradients of about 10 K and this simulation yields (17.6 ± 0.5) K. This was to be expected, as the maximal temperature in the membrane is significantly higher than the mean temperature over all layers of the ECs. However, the maximal thermal gradients were also notably higher than during the validation, where gradients around 13 K were predicted using the thermal conductivities from Krenz *et al.* This deviation can be attributed to the significantly higher thermal conductivity values assumed by Krenz *et al.* They used thermal conductivities measured by Bock *et al.* [7] for the membrane and PTL to calculate lumped conductivities. The CLs were not considered. The higher conductivities used by Krenz *et al.* can be explained by two factors: Firstly, the thermal conductivity given by Krenz *et al.* with reference to Bock *et al.* for the membrane is, probably by accident, ten times higher than given in the referenced paper of Bock *et al.* itself. The value given in the paper of Bock *et al.* also fits well with the thermal conductivity measured and used here. Secondly, Bock *et al.* measured significantly higher thermal conductivities in a sinter PTL than measured here for the felt PTL, as discussed in section 5.1.2. In order to determine the impact of the conductivity of the PTL on the temperature distribution, a scenario was examined using thermal conductivities of sintered PTL as measured by Bock *et al.* and is discussed later in this section.

Counter-flow conditions show slight performance benefits over parallel flow in the simulation. The voltage efficiency was with an increase of 0.2 % slightly higher under counter-flow conditions. Also the current density was more uniformly distributed over the cell in counter-flow as the current density distribution roughly follows the temperature distribution within the MEA. This can be explained by the fact that higher temperatures lead to locally reduced losses and thus higher current densities under a constant cell-voltage. This again leads to a higher heat generation rate and thus again a higher temperature so that both variables are interconnected. Therefore, also the maximal temperatures in the stack increased up to 1.2 K in counter-flow. This can be disadvantageous, as the maximal allowable temperature of the membrane is already reached at lower current densities. The temperature distribution was therefore also examined under higher current densities of $3\,\mathrm{A\,cm^{-2}}$ in another scenario and discussed later in this section. Li *et al.* [59] experimentally compared parallel and counter-flow conditions within a single EC and detected no notable difference in performance. However, the increase in efficiency might be more pronounced within the stack than in a single cell, as the exchange of heat between anodic and cathodic FF through the BP leads to more uniform conditions in the anodic and cathodic half-cell. This can be seen in the outer ECs of the stack, which lack the respective other electrode on one side of the EC. However, the predicted increase in efficiency is very small and can thus also be below the uncertainties of measurement in reality.
The lower temperatures in the ECs at the beginning and the end of the stack can be ascribed to the cooling effect of the non-insulated end-plates. This cooling effect was especially defined in the first EC, where the hot anode side adjoins the end-plate. In the last EC, the cooling effect was slightly lower because of the generally colder temperatures of the cathode side and thus

a cooler end-plate and less heat-transfer to the ambient. In order to reduce inhomogeneities within the stack, and to operate the cells at the end of the stacks at higher temperatures and thus higher efficiencies, it might be beneficial to insulate the end-plates to minimize heat-losses to the ambient. As the cooling effect of the end-plates only affects the outer ECs, the insulation can also be expected to only impact the temperature in the outer cells.

Sinter PTL

When the measured titanium felt PTLs were replaced by sintered titanium PTLs of the same thickness with a higher through-plane conductivity, the temperature gradients within the cells in the stack decreased by 3.5 K in counter-flow and 3.9 K in parallel flow. The maximal temperatures predicted using the sintered PTL were only 0.1 K higher in counter-flow and 0.6 K in parallel flow than predicted during the validation, where higher conductivities for CLs and membrane were used. This shows, that the PTLs are the layers with the highest impact on the temperature distribution within the ECs. This can be attributed to the high thickness of the PTL compared to the other EC layers. Using the higher conductive sinter PTL reduced the thermal gradient in the ECs by over 20 % in counter-flow and close to 25 % in parallel flow. This allows higher current densities in the stack before the maximal temperature is reached in the membrane and thus permits a higher hydrogen production rate. The lower voltage-efficiency can be counter-acted by higher inlet-temperatures when the current density should be kept constant. This points out the importance of considering thermal properties of the PTL layers within the design process to minimize thermal gradients within the ECs to maximize the current densities. However, the decrease in maximal temperature by using the sintered PTL would probably be slightly smaller in reality as the lower porosity leads to an increase in mass transfer overpotentials, which again leads to a higher heat production.
The decrease in temperature towards the right end of the stack was simulated to be slightly higher when using sinter PTL compared to the base scenario. This effect can also be explained by less heat flowing towards the cathodic and more heat flowing towards the anodic FF when the thermal conductivity of the PTL is increased, as discussed in section 5.2.1.
The in-plane conductivity, however, was assumed to be ten times the through-plane conductivity in the felt PTL due to its fibrous structure, whereas the thermal conductivity in the sinter PTL was assumed to be the same in-plane and through-plane leading to a 4 times higher in-plane conductivity in the felt PTL compared to the sintered PTL. This explains the change in the shape of the temperature field within the cell. However, it also shows that the in-plane conductivity has a subordinate relevance on the maximal cell temperature in industrial-sized stacks.

High current density

Increasing the current density from 2 to 3 $\mathrm{A\,cm^{-2}}$ led to a significant increase in maximal temperatures over the ECs by almost 10 K, both in parallel and counter-flow. Part of this increase was caused by higher temperatures in the FFs, which can be counteracted by increasing

the mass flow rates. However, also the thermal gradients between the MEA and the FFs increased by about one half to 14 K in the middle of the cells in counter flow, which can only significantly be reduced by constructive measures.
In counter-flow the maximal temperatures were about 1 K higher than in parallel flow, about the same amount as under a current density of $2\,\mathrm{A\,cm^{-2}}$. The advantage of counter-flow in terms of voltage efficiency slightly increased from 0.19 % at $2\,\mathrm{A\,cm^{-2}}$ to 0.25 % at $3\,\mathrm{A\,cm^{-2}}$. It thus seems beneficial to operate the stack in counter-flow without running into danger of generating additional hot-spots within the cells at high current densities. As discussed above, this advantage was not confirmed experimentally in a single EC [59], but might be more significant on a stack-level.
Running the stack at high current densities led to a significant decrease in voltage efficiency by about 3.6 % both in parallel and counter-flow, which is in contrast to the other simulation cases, where an increase in cell temperature caused a higher voltage efficiency. This can be explained by higher overpotentials due to the increased reaction rate. Increasing the current density thus seems disadvantageous, as more energy is required to produce the same amount of hydrogen. However, with a higher current density more hydrogen can be produced in the same time and thus more effectively. Trade-offs between efficiency and effectivity must be balanced individually for each use-case. This study can support the process by providing knowledge about the impact of an increased current density on efficiency and temperatures inside the stack.
Both in parallel and counter-flow, the cooling effect of the right end-plate on the MEAs inside the last ECs decreased notably with higher current densities. This effect can be explained by the overall higher heat fluxes towards the cathodic FF through the increased mass flows through the cell in x-direction and thus a smaller impact of the almost constant convective heat-losses towards the ambient.

Yasutake *et al.* [9] simulated the 2D temperature distribution within a single PEMEC of $1\,\mathrm{cm^2}$ cell area at high current densities along the channels of the FFs and in stacking direction. They also noticed a significant increase in temperature, especially on the anode side, with increasing current density. At $6.36\,\mathrm{A\,cm^{-2}}$, they predicted a temperature gradient of 10 K, at $7.75\,\mathrm{A\,cm^{-2}}$ a temperature gradient of 15 K. However, they kept the cell-voltage constant at 2.7 V and varied the thickness of the membrane to reach the desired current density. This and the different dimensions of the cell do not allow for a reliable quantitative comparison of the results.
Moradi Nafchi *et al.* [8] varied the current density only from 0.1 to $1.1\,\mathrm{A\,cm^{-2}}$ in their 1D simulation in stacking direction. They predicted an increase of about 0.2 K at the ACL surface but seem not to include PTLs into their simulation. This makes the results difficult to compare to the results of this study, as the PTLs have the largest contribution to the thermal gradients over the EC (cf. simulation scenario “Sinter PTL”).
No other studies are known that examine the effect of varying current density on the temperature distribution within an PEMEC.

Without water drag

The effect of water being dragged through the membrane was disabled in the simulation, and the results were compared to the case with water drag in order to determine the impact on the temperature distribution within the ECs in the stack. The maximal temperature inside the MEA decreased significantly by 2 to 3 K when the water drag was considered and more water was flowing through the MEA. This can be explained by the additional cooling effect through heating up the water until it reaches the warmest point in the cell. In the cooler layers on the cathode side, the water is cooled down, leading to a heating effect in this part of the cell and an overall higher effective thermal conductivity within the EC in x-direction.
With water drag, the temperature was therefore more uniformly distributed within the MEA, which could be expected to be beneficial for the efficiency of the cell. However, the current density was about $0.04\,\mathrm{A\,cm^{-2}}$ higher without water drag, which can be explained by the higher temperatures and thus lower overpotentials in the cell. This also explains the steeper temperature increase throughout the anodic FF without water drag. The temperature in the cathodic FF was about the same in both scenarios as the water drag led to a higher heat flux towards the cathode side, which seems to equal out the additional heat generation without water drag.
Whether this effect occurs with the same significance in an actual stack has to be validated experimentally. It was assumed that solid and fluid have the same temperature in each mesh-cell. This is a simplified approximation, as temperature gradients occur in reality between the phases due to heat transfer resistances. The consequence is a slightly lower cooling effect of the water drag in reality. However, because of presumably high heat exchange rates within the porous media, the error can be assumed to be low.

No other studies are known that examine the effect of water drag on the temperature distribution in larger PEMECs. The results could therefore not be compared to literature.

Warmer cathode

In order to further determine if a more uniform temperature within the MEA can be produced through operations management and utilized in form of higher efficiencies, the inlet-temperature of the FFs was increased by 3 K on the cathode side and decreased by 3 K on the anode side. However, no notable decrease in thermal gradient over the MEA could be identified in this scenario, which can be attributed to a small temperature difference between the anodic and cathodic FF inside the cell. The rapid decrease in temperature difference between the two FFs can be attributed to the high thermal conductivity of the thin BPs between the anodic and cathodic FFs of neighbouring cells.
Altering the inlet-temperatures of anode and cathode separately thus seems not to have a significant benefit on the efficiency of the electrolysis reaction. It is therefore not considered a favourable operating strategy.
No other literature is known that examines the effect of dissimilar FF temperatures on the performance of PEMECs.

6. Conclusion and Outlook

Thermal conductivities and compressibilities of PEMEC Tion5-W PFSA membrane, PEMEC CL and platinized titanium felt PTL were measured under different pressures and humidification levels in the first part of this study. In a second part, the temperature distribution within an industrial-sized PEM electrolyser was simulated along the channels of the FFs and in stacking direction, considering thermal gradients within the single cells using the measured thermal conductivities.

Through-plane thermal conductivities have been measured ex-situ using the heat flux method. The measurement procedure was verified by measuring thermal conductivities of PEEK, FC CL and Nafion® membrane. The measured thermal conductivities were in good agreement with literature. The compressibility of the materials was also examined, however, could only be measured with high uncertainty due to the measurement procedure.
Tion5-W PFSA membrane showed similar to Nafion® an increase in thermal conductivity by about 50 % when being soaked in water with no significant impact of compaction pressure. However, the thermal conductivity was overall slightly higher than that measured for Nafion®. The mean thermal conductivity over iridium ruthenium oxide anodic and platinum black cathodic EC CL was measured to be in the same order of magnitude as that of the membrane, but is significantly more compressible. The values were within literature values for FC CL, with a significant increase in thermal conductivity under compaction pressure for dry material and about 50 % higher thermal conductivities when being humidified at a pressure of 4.6 bar. However, thermal conductivities decreased under pressure in humidified material, which was not the case for FC CL. Whether this decrease in thermal conductivity is an inherent property of EC CL or must be attributed to the indirect measurements within a MEA, would have to be assessed in further measurements on separate CL samples. However, the impact on the temperature distribution within ECs is limited, as shown in the simulation.
For platinized titanium felt PTL with a porosity of (52 ± 5) vol.% dry thermal conductivities were measured to be about double the value of membrane or CL conductivities, but below the literature values for titanium-based PTLs. The thermal conductivities increased about five times when being humidified and over 50 % under pressure without notable compressibility. The increased conductivity under pressure can be explained by an increase in fibre-fibre contact within the felt and eventually a perturbation during measurements through the contact resistance between the stacked samples. If the contact resistance between the PTL samples notably impacted the results of the measurements, must be examined in further measurements, which were out of the scope

of this thesis. However, also in literature the contact resistance was neglected during similar measurements [7].

A 2D model has then been developed to simulate the temperature distribution within an industrial-sized PEM electrolyser with 1 m^2 cell area, considering thermal gradients within the single cells in the stack along the channels of the FFs and in stacking direction. The model has been validated on a cell- and stack-level using verified models from literature.
The model has then been used to simulate the conditions within the stack both for parallel and counter-flow conditions using the measured thermal conductivities. Under a mass flow of 0.15 $kg\,s^{-1}$ water of 60 °C at the inlet of both the anodic and cathodic FF of each cell and 2 $A\,cm^{-2}$ current density, temperature gradients of (16.5 ± 0.6) K in parallel flow and (17.6 ± 0.5) K in counter-flow conditions were predicted within the cells. The counter-flow arrangement showed an increase in voltage efficiency by 0.2 %. The maximal temperatures occurred between the ACL and membrane in the middle of the ECs in counter-flow and in parallel flow in the same layer in stacking direction but at the outlets of the FFs. This leads to general slightly higher temperatures in the anodic half-cell. The outer cells in the stack were predicted to be, depending on the flow arrangement, 2 to 4 K colder than in the middle of the stack when the end-plates were not thermally insulated against ambient. This again led to lower efficiencies in these cells. Compared to literature, where lumped properties were used within the ECs in stacking direction, the thermal gradients over the stack were about 20 to 40 % higher in this study.
Replacing the measured trough-plane thermal conductivity values of titanium felt PTL by the two times higher literature values for sintered PTL led to 3.5 K lower thermal gradients in counter-flow and a 3.9 K reduction in parallel flow. The impact of membrane and CL thermal conductivities was low compared to this. It is thus important to consider the PTL through-plane thermal conductivity during the design process to minimize thermal gradients and maximize possible current densities within the stack. The in-plane thermal conductivity of the PTL was of lower relevance due to the long FFs in industrial-sized electrolysers.
Increasing the current density to 3 $A\,cm^{-2}$ increased the thermal gradients by about 10 K both in parallel and counter-flow at constant flow rates and reduced the voltage efficiency by about 3.6 %. The advantage of counter-flow arrangement in terms of voltage efficiency increased slightly with the current density. The maximal temperature was still lower in parallel flow, but with a deviation of less than 1 K.
Furthermore, the effect of water being dragged through the membrane by the hydrogen ions was investigated with regard to its impact on the temperature distribution within the cells in parallel flow. At the side of the FF inlets, the maximal temperature in the MEA increased by 2 to 3 K when the water drag was disabled and thermal gradient within the MEA grew. The higher temperatures led to a slight increase in efficiency and thus current density under constant voltage, which resulted in an 0.5 K increased outlet temperature in the anodic FF. The temperature in the cathodic FF did not significantly change due to the increased heat transport to this side when considering water drag.
In order to examine possible efficiency benefits through lower thermal gradients over the MEA,

the inlet-temperature of the fluid was increased at the cathode side and decreased on the anode side. Due to the high thermal conductivity of the BPs, however, the fluid temperatures between two adjacent anodic and cathodic FFs annealed quickly inside the ECs. Thus, no impact on performance or maximal temperatures in the cells could be identified.

During the design process of future electrolysers, especially at high current densities, the temperature distribution within the single ECs must be considered also on a stack level in order to prevent overheating of the membrane or the necessity of increased safety margins due to unknown temperature gradients. The trough-plane thermal conductivity and thickness of the PTLs have been identified as important factors to limit thermal gradients, and should thus be considered during materials selection in future electrolysers in order to limit thermal gradients within the ECs.
In future research, the thermal conductivity of further, different PTL materials should be investigated in order to identify high-conductive PTL materials which are suited to reduce thermal gradients in next-generation PEMs electrolysers. As part of this, also the thermal conductivity of titanium felt PTL should be measured again using custom-made samples of different thicknesses in order to rule out an eventual contact resistance between the samples that might impact the measured thermal conductivity. Furthermore, the model developed here could be refined by considering separate temperatures for fluids and solids using advanced heat transfer models inside the porous layers and thus further increasing the accuracy of the calculated cooling effect of mass flows through the MEA.

Bibliography

[1] S. Schiebahn, T. Grube, M. Robinius, V. Tietze, B. Kumar, and D. Stolten, "Power to gas: Technological overview, systems analysis and economic assessment for a case study in germany", *International Journal of Hydrogen Energy*, vol. 40, no. 12, pp. 4285–4294, 2015.

[2] K. Kavadias, D. Apostolou, and J. Kaldellis, "Modelling and optimisation of a hydrogen-based energy storage system in an autonomous electrical network", *Applied Energy*, 2017.

[3] S. Shiva Kumar and H. Lim, "An overview of water electrolysis technologies for green hydrogen production", *Energy Reports*, vol. 8, pp. 13 793–13 813, 2022.

[4] K. Zhang *et al.*, "Status and perspectives of key materials for pem electrolyzer", *Nano Research Energy*, vol. 1, e9120032, 2022.

[5] T. Krenz *et al.*, "Temperature and performance inhomogeneities in pem electrolysis stacks with industrial scale cells", *Journal of The Electrochemical Society*, vol. 170, no. 4, p. 044 508, 2023.

[6] O. S. Burheim, "(invited) review: Pemfc materials' thermal conductivity and influence on internal temperature profiles", *ECS Meeting Abstracts*, vol. MA2017-02, no. 33, p. 1458, 2017.

[7] R. Bock *et al.*, "Measuring the thermal conductivity of membrane and porous transport layer in proton and anion exchange membrane water electrolyzers for temperature distribution modeling", *International Journal of Hydrogen Energy*, vol. 45, no. 2, pp. 1236–1254, 2020.

[8] F. Moradi Nafchi, E. Afshari, and E. Baniasadi, "Thermal and electrochemical analyses of a polymer electrolyte membrane electrolyzer", *International Journal of Hydrogen Energy*, vol. 47, no. 95, pp. 40 172–40 183, 2022.

[9] M. Yasutake *et al.*, "Temperature distribution analysis of pem electrolyzer in high current density operation by numerical simulation", *ECS Transactions*, vol. 109, no. 9, pp. 437–450, 2022.

[10] R. García-Valverde, N. Espinosa, and A. Urbina, "Simple pem water electrolyser model and experimental validation", *International Journal of Hydrogen Energy*, vol. 37, no. 2, pp. 1927–1938, 2012.

[11] G. Correa, P. Marocco, P. Muñoz, T. Falagüerra, D. Ferrero, and M. Santarelli, "Pressurized pem water electrolysis: Dynamic modelling focusing on the cathode side", *International Journal of Hydrogen Energy*, vol. 47, no. 7, pp. 4315–4327, 2022.

[12] H. Kim, M. Park, and K. S. Lee, "One-dimensional dynamic modeling of a high-pressure water electrolysis system for hydrogen production", *International Journal of Hydrogen Energy*, vol. 38, no. 6, pp. 2596–2609, 2013.

[13] G. Nellis and S. A. Klein, *Heat transfer*. Cambridge: Cambridge Univ. Press, 2009.

[14] Q. Feng *et al.*, "A review of proton exchange membrane water electrolysis on degradation mechanisms and mitigation strategies", *Journal of Power Sources*, vol. 366, pp. 33–55, 2017.

[15] T. E. Springer, T. A. Zawodzinski, and S. Gottesfeld, "Polymer electrolyte fuel cell model", *Journal of The Electrochemical Society*, vol. 138, no. 8, pp. 2334–2342, 1991.

[16] D. Stolten, R. C. Samsun, and N. Garland, Eds., *Fuel cells: Data, facts and figures*. Weinheim: Wiley-VCH Verlag GmbH & Co. KGaA, 2016.

[17] M. Möckl, M. Bernt, J. Schröter, and A. Jossen, "Proton exchange membrane water electrolysis at high current densities: Investigation of thermal limitations", *International Journal of Hydrogen Energy*, vol. 45, no. 3, pp. 1417–1428, 2020.

[18] D. S. Falcão and A. Pinto, "A review on pem electrolyzer modelling: Guidelines for beginners", *Journal of Cleaner Production*, vol. 261, p. 121 184, 2020.

[19] N. A. David, P. M. Wild, J. Hu, and N. Djilali, "In-fibre bragg grating sensors for distributed temperature measurement in a polymer electrolyte membrane fuel cell", *Journal of Power Sources*, vol. 192, no. 2, pp. 376–380, 2009.

[20] N. David, K. von Schilling, P. M. Wild, and N. Djilali, "In situ measurement of relative humidity in a pem fuel cell using fibre bragg grating sensors", *International Journal of Hydrogen Energy*, vol. 39, no. 31, pp. 17 638–17 644, 2014.

[21] M. E. Lebbal and S. Lecœuche, "Identification and monitoring of a pem electrolyser based on dynamical modelling", *International Journal of Hydrogen Energy*, vol. 34, no. 14, pp. 5992–5999, 2009.

[22] ISO/IEC, *Guide 98-3:2008: Uncertainty of measurement - part 3: Guide to the expression of uncertainty in measurement*, 2008.

[23] O. Burheim, P. Vie, J. G. Pharoah, and S. Kjelstrup, "Ex situ measurements of through-plane thermal conductivities in a polymer electrolyte fuel cell", *Journal of Power Sources*, vol. 195, no. 1, pp. 249–256, 2010.

[24] M. Khandelwal and M. M. Mench, "Direct measurement of through-plane thermal conductivity and contact resistance in fuel cell materials", *Journal of Power Sources*, vol. 161, no. 2, pp. 1106–1115, 2006.

[25] R. Asmatulu, A. Khan, V. K. Adigoppula, and G. Hwang, "Enhanced transport properties of graphene-based, thin nafion® membrane for polymer electrolyte membrane fuel cells", *International Journal of Energy Research*, vol. 42, no. 2, pp. 508–519, 2018.

[26] M. Ahadi, M. Andisheh-Tadbir, M. Tam, and M. Bahrami, "An improved transient plane source method for measuring thermal conductivity of thin films: Deconvoluting thermal contact resistance", *International Journal of Heat and Mass Transfer*, vol. 96, pp. 371–380, 2016.

[27] M. Ahadi, M. Tam, M. S. Saha, J. Stumper, and M. Bahrami, "Thermal conductivity of catalyst layer of polymer electrolyte membrane fuel cells: Part 1 – experimental study", *Journal of Power Sources*, vol. 354, pp. 207–214, 2017.

[28] R. Bock *et al.*, "The influence of graphitization on the thermal conductivity of catalyst layers and temperature gradients in proton exchange membrane fuel cells", *International Journal of Hydrogen Energy*, vol. 45, no. 2, pp. 1335–1342, 2020.

[29] O. S. Burheim, H. Su, H. H. Hauge, S. Pasupathi, and B. G. Pollet, "Study of thermal conductivity of pem fuel cell catalyst layers", *International Journal of Hydrogen Energy*, vol. 39, no. 17, pp. 9397–9408, 2014.

[30] O. S. Burheim *et al.*, "Thermal conductivity in the three layered regions of micro porous layer coated porous transport layers for the pem fuel cell", *International Journal of Hydrogen Energy*, vol. 40, no. 46, pp. 16 775–16 785, 2015.

[31] O. S. Burheim and J. G. Pharoah, "A review of the curious case of heat transport in polymer electrolyte fuel cells and the need for more characterisation", *Current Opinion in Electrochemistry*, vol. 5, no. 1, pp. 36–42, 2017.

[32] R. Bock, B. Hamre, M. A. Onsrud, H. Karoliussen, F. Seland, and O. S. Burheim, "The influence of argon, air and hydrogen gas on thermal conductivity of gas diffusion layers and temperature gradients in pemfcs", *ECS Transactions*, vol. 92, no. 8, pp. 223–245, 2019.

[33] O. S. Burheim, G. Ellila, J. D. Fairweather, A. Labouriau, S. Kjelstrup, and J. G. Pharoah, "Ageing and thermal conductivity of porous transport layers used for pem fuel cells", *Journal of Power Sources*, vol. 221, pp. 356–365, 2013.

[34] R. Bock *et al.*, "Thermal conductivity and compaction of gdl-mpl interfacial composite material", *Journal of The Electrochemical Society*, vol. 165, no. 7, F514–F525, 2018.

[35] X.-Z. Yuan *et al.*, "The porous transport layer in proton exchange membrane water electrolysis: Perspectives on a complex component", *Sustainable Energy & Fuels*, vol. 6, no. 8, pp. 1824–1853, 2022.

[36] J. Zhao, H. Liu, and X. Li, "Structure, property, and performance of catalyst layers in proton exchange membrane fuel cells", *Electrochemical Energy Reviews*, vol. 6, no. 1, p. 13, 2023.

[37] T. Chen, S. Liu, J. Zhang, and M. Tang, "Study on the characteristics of gdl with different ptfe content and its effect on the performance of pemfc", *International Journal of Heat and Mass Transfer*, vol. 128, pp. 1168–1174, 2019.

[38] T. Schuler, T. J. Schmidt, and F. N. Büchi, "Polymer electrolyte water electrolysis: Correlating performance and porous transport layer structure: Part ii. electrochemical performance analysis", *Journal of The Electrochemical Society*, vol. 166, no. 10, F555–F565, 2019.

[39] O. S. Burheim, J. G. Pharoah, H. Lampert, P. J. S. Vie, and S. Kjelstrup, "Through-plane thermal conductivity of pemfc porous transport layers", *Journal of Fuel Cell Science and Technology*, vol. 8, no. 2, 2011.

[40] R. Bock *et al.*, "Experimental study of thermal conductivity and compression measurements of the gdl-mpl interfacial composite region", *ECS Transactions*, vol. 75, no. 14, pp. 189–199, 2016.

[41] A. K. van der Vegt and L. Govaert, *Polymeren: Van keten tot kunststof*, 5e dr. Delft: DUP Blue Print, 2003.

[42] E. Alizadeh, M. M. Barzegari, M. Momenifar, M. Ghadimi, and S. Saadat, "Investigation of contact pressure distribution over the active area of pem fuel cell stack", *International Journal of Hydrogen Energy*, vol. 41, no. 4, pp. 3062–3071, 2016.

[43] E. Passalacqua, F. Lufrano, G. Squadrito, A. Patti, and L. Giorgi, "Nafion content in the catalyst layer of polymer electrolyte fuel cells: Effects on structure and performance", *Electrochimica Acta*, vol. 46, no. 6, pp. 799–805, 2001.

[44] G.-Y. Chen *et al.*, "Gradient design of pt/c ratio and nafion content in cathode catalyst layer of pemfcs", *International Journal of Hydrogen Energy*, vol. 42, no. 50, pp. 29 960–29 965, 2017.

[45] E. Borgardt *et al.*, "Impact of clamping pressure and stress relaxation on the performance of different polymer electrolyte membrane water electrolysis cell designs", *International Journal of Hydrogen Energy*, vol. 44, no. 42, pp. 23 556–23 567, 2019.

[46] D. Roizard, "Antoine equation", in *Encyclopedia of Membranes*, ser. Springer eBook Collection, E. Drioli and L. Giorno, Eds., Berlin, Heidelberg: Springer, 2019, pp. 1–3.

[47] P. Trinke, *Experimental and model-based investigations on gas crossover in polymer electrolyte membrane water electrolyzers*, Gottfried Wilhelm Leibniz Universitat Hannover, Ed., 2021.

[48] H. Ito, T. Maeda, A. Nakano, and H. Takenaka, "Properties of nafion membranes under pem water electrolysis conditions", *International Journal of Hydrogen Energy*, vol. 36, no. 17, pp. 10 527–10 540, 2011.

[49] P. Trinke, B. Bensmann, and R. Hanke-Rauschenbach, "Current density effect on hydrogen permeation in pem water electrolyzers", *International Journal of Hydrogen Energy*, vol. 42, no. 21, pp. 14 355–14 366, 2017.

[50] J. H. Lienhard, *A heat transfer textbook*, Fourth edition. New York: Dover Publications, 2017.

[51] M. Bhaiya, A. Putz, and M. Secanell, "Analysis of non-isothermal effects on polymer electrolyte fuel cell electrode assemblies", *Electrochimica Acta*, vol. 147, pp. 294–309, 2014.

[52] P. Moin, *Fundamentals of engineering numerical analysis*, 2. ed. Cambridge: Cambridge Univ. Press, 2010.

[53] J. Peron *et al.*, "Properties of nafion® nr-211 membranes for pemfcs", *Journal of Membrane Science*, vol. 356, no. 1-2, pp. 44–51, 2010.

[54] K. K. Pushpa, D. Nandan, and R. M. Iyer, "Thermodynamics of water sorption by perfluorosulphonate (nafion-117) and polystyrene–divinylbenzene sulphonate (dowex 50w) ion-exchange resins at 298 ± 1 k", *Journal of the Chemical Society, Faraday Transactions 1: Physical Chemistry in Condensed Phases*, vol. 84, no. 6, p. 2047, 1988.

[55] T. A. Zawodzinski, M. Neeman, L. O. Sillerud, and S. Gottesfeld, "Determination of water diffusion coefficients in perfluorosulfonate ionomeric membranes", *The Journal of Physical Chemistry*, vol. 95, no. 15, pp. 6040–6044, 1991.

[56] W. Martienssen and H. Warlimont, *Springer handbook of condensed matter and materials data: With 914 tables* (Springer handbook). Berlin and Heidelberg: Springer, 2005.

[57] J. C. Dixon, Ed., *The shock absorber handbook* (Wiley-professional engineering publishing series), 2. ed. Chichester: John Wiley, 2007.

[58] A. D. Shum, D. Y. Parkinson, X. Xiao, A. Z. Weber, O. S. Burheim, and I. V. Zenyuk, "Investigating phase–change–induced flow in gas diffusion layers in fuel cells with x–ray computed tomography", *Electrochimica Acta*, vol. 256, pp. 279–290, 2017.

[59] H. Li, H. Nakajima, A. Inada, and K. Ito, "Effect of flow-field pattern and flow configuration on the performance of a polymer-electrolyte-membrane water electrolyzer at high temperature", *International Journal of Hydrogen Energy*, vol. 43, no. 18, pp. 8600–8610, 2018.

A. Appendix

A.1. Measured thermal conductivity values

Table A.1.: Measured thermal conductivities of FC materials in $\mathrm{W\,m^{-1}\,K^{-1}}$ at different compaction pressures. Measurement order was from left to right in table

Material	4.6 bar	9.3 bar	13.9 bar	4.6 bar
Nafion® 211 dry	0.183 ± 0.011	0.184 ± 0.008	0.184 ± 0.007	-
Nafion® 211 wet	0.268 ± 0.025	0.263 ± 0.021	0.261 ± 0.016	0.264 ± 0.024
MEA dry	0.136 ± 0.011	0.154 ± 0.009	0.166 ± 0.008	-
MEA wet	0.333 ± 0.009	0.327 ± 0.009	0.326 ± 0.009	0.336 ± 0.018
Catalyst layer dry	0.104 ± 0.015	0.128 ± 0.015	0.146 ± 0.016	-
Catalyst layer wet	0.610 ± 0.048	0.642 ± 0.065	0.674 ± 0.067	0.726 ± 0.201

Table A.2.: Measured thermal conductivities of EC materials in $\mathrm{W\,m^{-1}\,K^{-1}}$ at different compaction pressures. Measurement order was from left to right in table

Material	4.6 bar	9.3 bar	16.0 bar	4.6 bar
Tion5-W	0.191 ± 0.006	0.193 ± 0.005	0.193 ± 0.004	-
Tion5-W wet	0.332 ± 0.026	0.322 ± 0.010	0.313 ± 0.011	0.304 ± 0.007
MEA dry	0.168 ± 0.004	0.180 ± 0.005	0.189 ± 0.003	-
MEA wet	0.314 ± 0.031	0.292 ± 0.021	0.283 ± 0.016	0.270 ± 0.020
Catalyst layer dry	0.128 ± 0.006	0.154 ± 0.012	0.177 ± 0.008	-
Catalyst layer wet	0.245 ± 0.090	0.201 ± 0.038	0.193 ± 0.029	0.178 ± 0.031
Titan fibre felt	0.316 ± 0.041	0.423 ± 0.033	0.512 ± 0.029	-
Titan fibre felt	2.495 ± 0.167	2.577 ± 0.164	2.671 ± 0.213	2.697 ± 0.279

Table A.3.: Measured thermal conductivities of EC materials in $\mathrm{W\,m^{-1}\,K^{-1}}$ at different compaction pressures. Each pressure was measured with freshly wetted sample.

Material	4.6 bar	9.3 bar	16.0 bar
Tion5-W wet	0.378 ± 0.061	0.322 ± 0.027	0.314 ± 0.012
MEA wet	0.356 ± 0.075	0.303 ± 0.024	0.300 ± 0.030
Catalyst layer wet	0.274 ± 0.206	0.236 ± 0.091	0.242 ± 0.103
Titan fibre felt	3.26 ± 0.77	3.47 ± 1.09	12.3 ± 52.0

A.2. Simulated temperature gradients

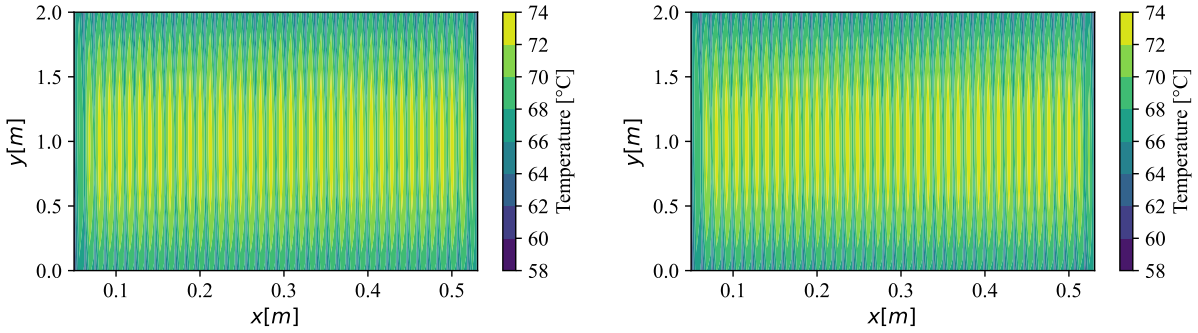

(a) $N_{\text{mesh-cells,y}} = 21$ **(b)** $N_{\text{mesh-cells,y}} = 42$

Figure A.1.: Results mesh refinement study on a stack level

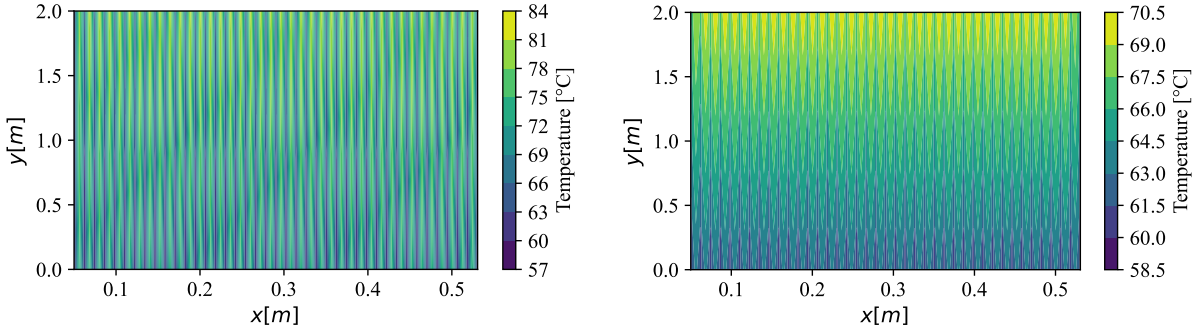

(a) Low conductivity: $2\,\mathrm{W\,m^{-1}\,K^{-1}}$ **(b)** High conductivity: $15\,\mathrm{W\,m^{-1}\,K^{-1}}$

Figure A.2.: Results of validation for high and low thermal conductivities under parallel flow on stack level

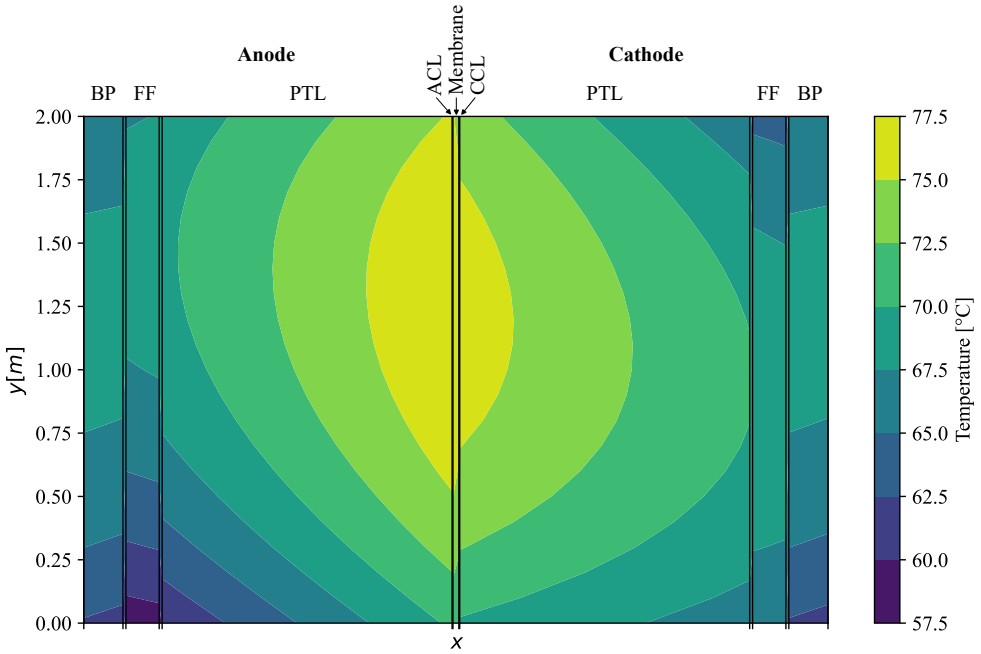

Figure A.3.: Simulated temperature distribution in middle cell (no. 20) under counter-flow with an warmer inlet-temperature in the cathodic FF

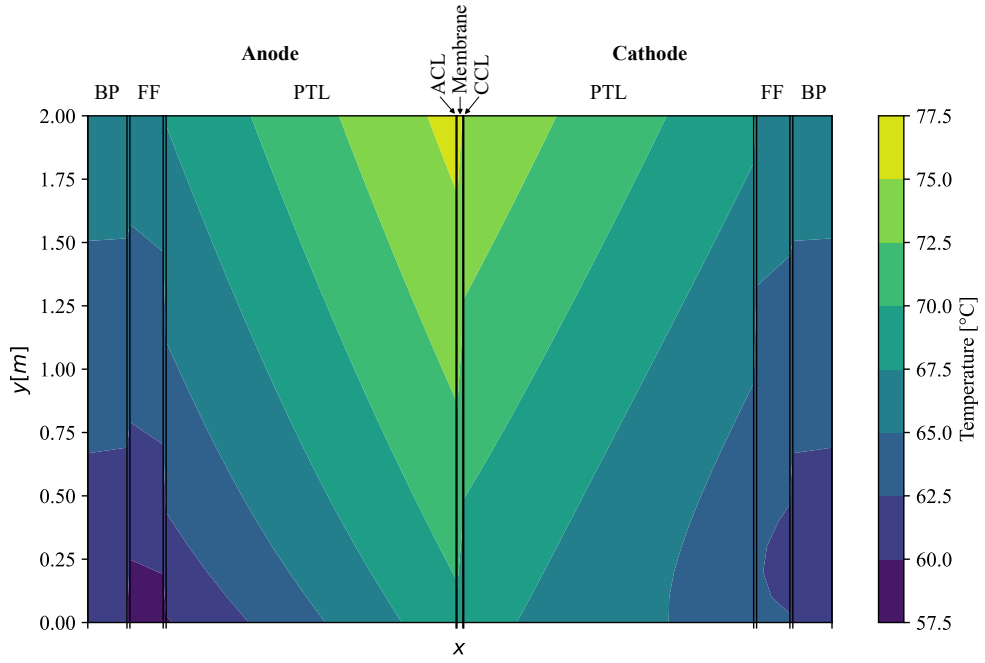

Figure A.4.: Simulated temperature distribution in middle cell (no. 20) under parallel flow with an warmer inlet-temperature in the cathodic FF

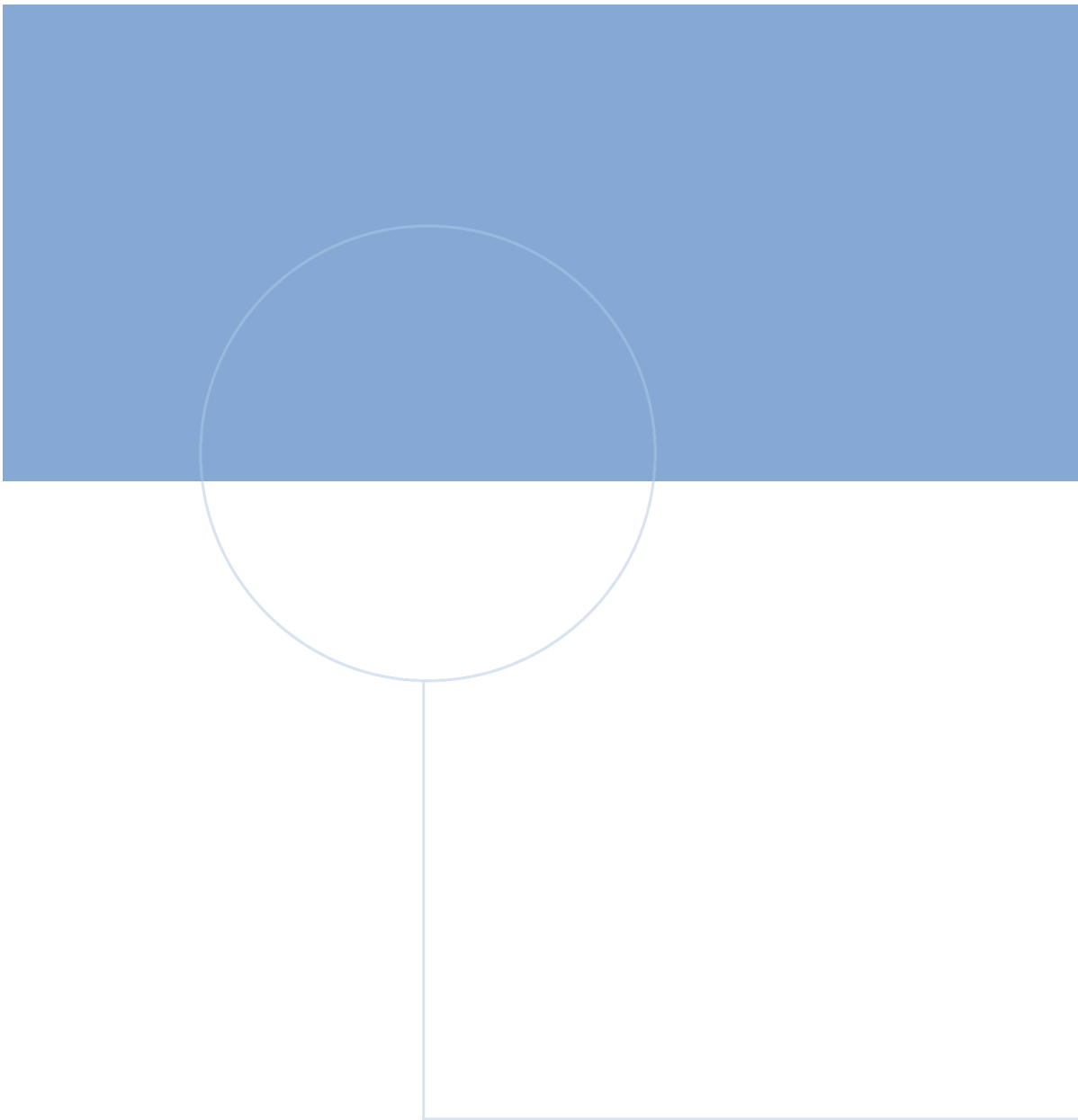

NTNU

Norwegian University of
Science and Technology